Fabrication and Characterization of 2-Port Surface Acoustic Wave (SAW) Resonators for Strain Sensing

Liam Kelly

Thesis submitted to the University of Ottawa in partial fulfillment of the requirements for the degree of

Master of Science in Physics

Department of Physics
Faculty of Science
University of Ottawa

Abstract

This thesis focuses on the theory, fabrication, and characterization of 2-port surface acoustic wave (SAW) resonators, as well as the application of their Fabry-Pérot resonance modes for strain sensing. The thesis includes three articles. In the first article, a fabrication method for high frequency SAW devices using traditional UV photolithography equipment is developed. It is well known that SAW sensors become more sensitive at higher frequencies but realizing high frequency devices requires small features which challenge existing photolithography methods. The proposed process is a modified version of a previously reported tri-layer lift-off photolithography process intended for Si or SiO_2 substrates which allows for compatibility with materials that are piezoelectric and pyroelectric, often used as the substrate in SAW devices. The process uses a lithographic tri-layer consisting of layers of lift-off resist (LOR) on the bottom, back anti-reflection coating (BARC) in the middle, and photoresist (PR) on top, improving resolution by a factor of two over traditional lift-off photolithography techniques. We demonstrate the fabrication of a SAW device with an interdigital transducer (IDT) pitch of 4 μm (minimum feature size of 1 μm) on 128° Y-X cut lithium niobate, whose operating frequency is measured as 994.5 MHz. The 2-Port SAW devices that are used in subsequent chapters are fabricated using this process.

The second article proposes a method of analyzing acoustic Fabry-Pérot spectra, by analogy with optical cavities, to determine key SAW parameters. In our experiment, 2-port SAW resonators, consisting of two interdigital transducers (IDTs) laterally separated by a free surface cavity length, are used to generate SAWs on 128° Y-X lithium niobate that are trapped between the two IDTs which also act as Bragg reflectors. Fabry-Pérot cavity peaks can be observed through the electrical S_{11} (reflection) spectrum measured on one IDT, hence a 2-Port resonator is equivalent to an acoustic Fabry-Pérot cavity/resonator. Measurements of the free spectral range and linewidths are then fitted to linear models to obtain the free surface velocity and attenuation of SAW waves, as well as the reflection of interdigital transducers (IDTs), all of which are crucial design parameters. Our method of analyzing Fabry-Pérot spectra provides a convenient method for determining key characteristics of SAW waves and cavities.

In the third article, a surface acoustic wave (SAW) strain sensor based on measuring acoustic Fabry-Pérot resonance peaks from a 2-port SAW resonator is demonstrated. A theoretical analysis is proposed to estimate the frequency sensitivity to strain of IDT and cavity resonances and to predict strain distributions in both the cavity and IDT regions of a 2-port SAW resonator bonded to a tapered cantilever beam. The frequency stability of cavity resonance peaks for fabricated 2-port SAW resonators of different cavity length are measured and analyzed to determine the cavity length which exhibits maximum frequency stability. A cross-correlation analysis technique is then introduced to improve the detection of the frequency shift of SAW resonances and enable multimode frequency shift detection. The measured frequency sensitivity to strain of the cavity resonances of a resonator 10 mm in length (operating frequency = 97.7 MHz) was found to be -103.2 ± 0.2 Hz/με while demonstrating excellent linearity (R^2 = 0.9999). By considering a minimum signal to noise ratio (SNR) of 3 dB, the device exhibits a minimum strain resolution of only 234 nε.

Acknowledgements

To begin, I'd like to thank my supervising professors, Xiaoyi Bao and Pierre Berini, for their constant support and guidance over the course of my time at uOttawa. Our weekly discussions were not only tremendously helpful for progressing our projects, but the hour we'd spend together was always enjoyable. Thank you to Prof. Bao for taking a chance on me as a student, I am always grateful for the opportunities that you've afforded me. Your imagination and ability to reach into the true physics meaning of the problems we faced was a tremendous tool. Thank you very much for supporting me financially throughout my studies. Thanks to Prof. Berini for agreeing to come along on this project with Prof. Bao and I, I can't imagine how our project would turn out without you. Your clarity of thought and ability to turn complex problems into simpler was invaluable. As much as both of you have impressed me by your ability as professors, I've been even more impressed by how great you are as people. You are both incredibly kind, understanding, patient, and good humored, and being your student has been both an honour and a pleasure.

I would also sincerely thank everyone else at uOttawa who's helped me along the way. None of the fabrication work would be possible without the help of Sabaa Rashid, Howard Northfield, and Anthony Olivieri. Thank you all for always helping me out and spending time to teach me things. Thanks to Maryam Amiri Naeini, Luis Mayoral Astorga, and Zohreh Hirbodvash, for all your help in 337 and for the kindness you all showed me. Thanks to Prof. Liang Chen, Chams Baker, Chen Chen, and all the members of Prof. Bao's group for our seminar presentations for all the help and insights you have given me.

Finally, I'd like to thank my family and all my wonderful friends. And thanks to Sara for your constant love and support.

Table of contents

Table of figures

List of Acronyms

AFM	atomic force microscope
Al	aluminum
BARC	back anti-reflection coating
Cr	chromium
DI	de-ionized
FBG	fiber Bragg grating
FEM	finite element method
FSR	free spectral range
HIM	helium ion microscope
IDT	interdigital transducer
IPA	isopropyl alcohol
$LiNbO_3$	lithium niobate
LOR	lift-off resist
PR	photoresist
PSR	post-spin relax
RIE	reactive ion etch
SAW	surface acoustic wave
SEM	scanning electron microscope
SNR	signal to noise ratio
VNA	vector network analyzer

Chapter 1 – Introduction

In 1885 Lord Rayleigh predicted a type of elastic wave that travels along a solid surface and is confined to a depth comparable to their wavelength [1], known as surface acoustic waves (SAWs). It wasn't until 1965, when the invention of the interdigital transducer (IDT) would enable the efficient generation and detection of SAWs on piezoelectric substrates [2], that a boom in the use of SAW technology in microelectronics would be initiated. SAW devices would soon gain immense popularity as pulse compression filters for radar signal processing and as electronic bandpass filters for consumer devices such as televisions and cellphones [3]. As SAW devices continued to find success in the consumer and military industries, an increasing number of new SAW applications were explored. SAW devices were used as microfluidic pumps and tweezers [4], and as chemical vapour, temperature, and strain sensors [5]. And in the past decade, SAW devices have been exploited for their ability to couple to quantum systems, *e.g.*, superconducting qubits [6], [7], [8] and quantum dots [9]. With such a wide range of application in research and commercial industries, over 1 billion SAW devices are manufactured every year [10].

Meanwhile in the field of optics, Charles Fabry and Alfred Pérot proposed a novel form of interference device back in 1897. The device made use of the interference of electromagnetic waves due to their successive reflection between two parallel silvered glass plates, named the Fabry-Pérot interferometer after its founders. The spectrum of the Fabry-Pérot interferometer is characterized by sharp peaks which periodically repeat with a separation equal to the free spectral range, given as $c/2nL$ where c is the speed of light in vacuum and n and L are the refractive index and length of the medium between the reflectors, respectively. This interferometer found a wide variety of applications in metrology and spectroscopy [11]. Furthermore, since the basis of the Fabry-Pérot interferometer is wave interference, the same principles that apply to the electromagnetic waves in the Fabry-Pérot apply to mechanical waves as well, as has been demonstrated with surface acoustic waves [12].

In this thesis, the Fabry-Pérot resonance peaks from a 2-port SAW resonator are used to demonstrate a high-resolution strain sensor. To fabricate 2-port SAW resonators, a lift-off photolithography method for high frequency SAW device fabrication is presented. Fabricated 2-port SAW resonators, which act as Fabry-Pérot cavities due to the Bragg reflectance of IDTs, are characterized by analysing the free spectral range and linewidth of cavity resonances in the acoustic Fabry-Pérot spectrum. The thesis concludes with a study of the performance of high-resolution strain sensors based on Fabry-Pérot resonances from 2-port SAW resonators, where the frequency stability of cavity peaks as a function of cavity length is investigated and the sensitivity and resolution of the strain sensor are determined.

1.1 Surface acoustic waves

In 1885, Lord Rayleigh discovered a type of elastic wave that propagates along a solid surface and who's amplitude is confined to a depth beneath the surface that is comparable to their wavelength [1]. Named the Rayleigh wave after its pioneer, they will be referred to as SAWs henceforth[1]. When excited in a piezoelectric substrate, the mechanical wave associated with SAWs are accompanied by a potential wave due to the piezoelectric effect. And while wave solutions for SAW propagation are known to be complex, it happens that the electrical potential generated at the substrate surface by SAWs can be effectively modelled as a travelling potential wave [3]:

$$\varphi(x,t) = \varphi_0 \exp\left(i(2\pi f t - kx)\right)$$

where φ_0 is the initial potential amplitude of the wave, f is its frequency, and k is the wavenumber, $k = 2\pi f/v - i\alpha_{loss}/2$, where v is the SAW velocity and α_{loss} is the intensity attenuation coefficient in (1/m). SAW propagation can also be modelled more extensively using finite element analysis (FEA). Electrostatics, solid mechanics, and piezoelectric constitutive equations are solved at each finite element to determine SAW propagation throughout the computational domain (the equations used for SAW

[1] Note, Rayleigh waves are technically a subtype of SAW. However, in the literature the two terms are often used interchangeably.

propagation calculations are detailed in Chapter 2.3 Subsection 3.4). Figure 1 shows the associated displacement and potential distributions of a SAW travelling along the free surface of 128° Y-X lithium niobate as calculated using COMSOL Multiphysics.

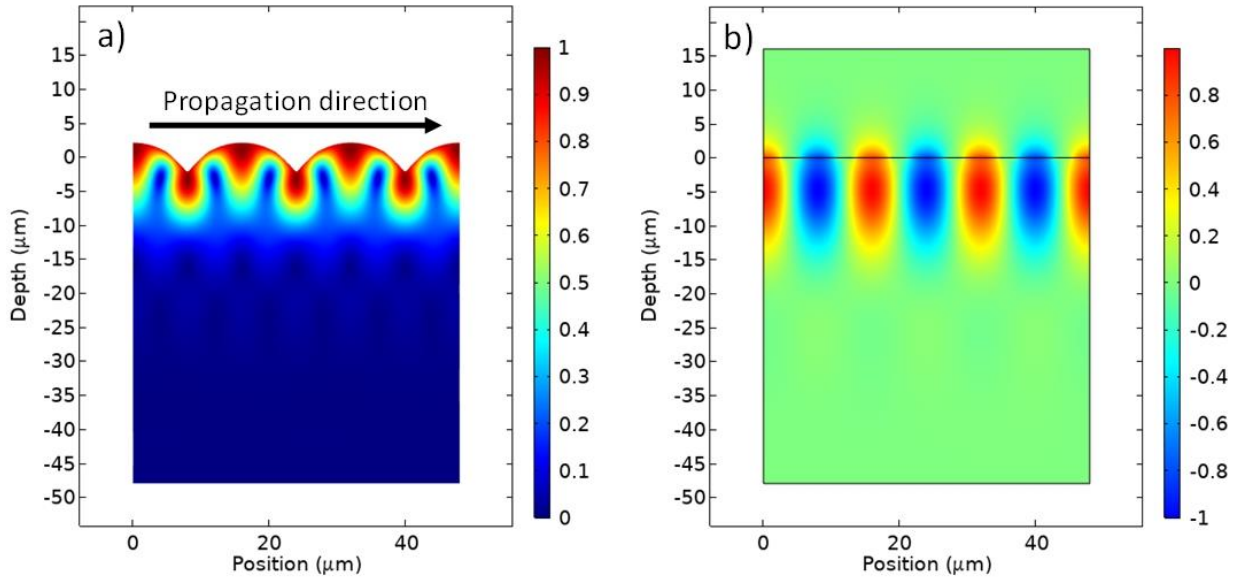

Figure 1: SAW mode as calculated using COMSOL Multiphysics eigenfrequency simulation. a) Deformed surface map of the normalized displacement amplitude of a SAW mode; b) surface map of the normalized electric potential of a SAW mode.

SAWs are distinct due to their strong surface confinement, having a displacement profile which decays rapidly with depth into the substrate. The relative amplitudes of u, the displacement parallel to the SAW propagation, and v, the displacement parallel to the surface normal, associated with a SAW are plotted as a function of depth into the substrate in Figure 2. The total displacement magnitude, $\sqrt{u^2 + v^2}$, can be seen to decay exponentially with depth into the substrate.

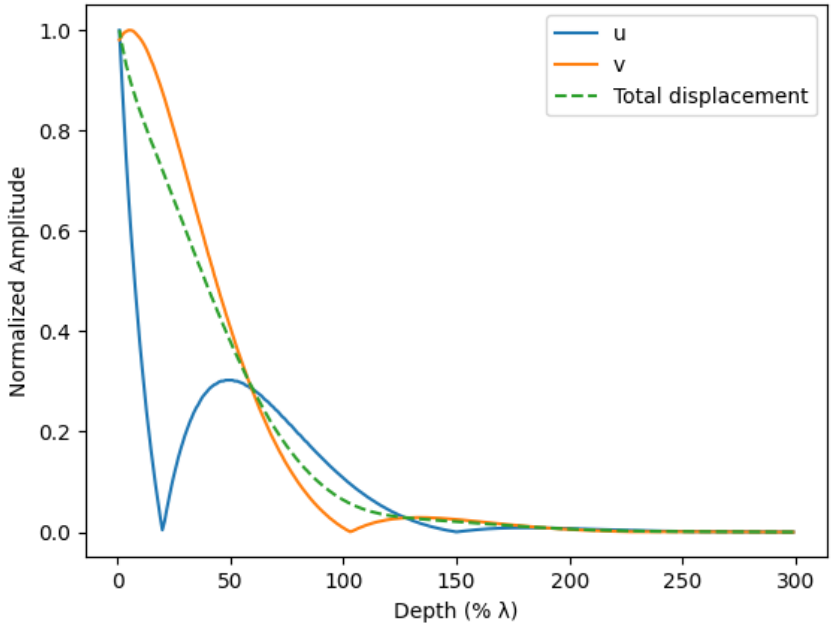

Figure 2: Normalized amplitudes of the absolute material displacements associated with surface acoustic waves (SAWs) as a function of depth beneath the substrate. u is the displacement parallel to the SAW propagation, v is the displacement parallel to the surface normal and the total displacement magnitude is $\sqrt{u^2 + v^2}$.

1.2 Interdigital transducers

In 1965, the interdigital transducer (IDT) was introduced by White and Voltmer [2]. Since then, SAW devices almost always include one or two IDTs on a piezoelectric substrate used to excite or detect SAWs. Fabricated from thin metal films, IDTs consist of two electrodes with interdigitated fingers, as seen in Figure 3. The period between fingers from the same electrode is known as the IDT pitch (λ_{IDT}) and defines the length of a unit cell which periodically repeats itself over the length of the IDT. By applying an AC signal across the IDT electrodes, an electric potential distribution is generated in the piezoelectric substrate which overlaps with and excites SAW modes. When the frequency of the applied signal matches the frequency of the SAW mode of wavelength λ_{IDT} ($f_{IDT} = v_{IDT}/\lambda_{IDT}$), SAW excitation is maximised as the phase accumulated over the length of the IDT period is equal to 2π, and thus IDTs generated from successive finger pairs are in phase. This frequency is known as the fundamental operating frequency of the SAW device (f_{IDT}). SAW devices exhibit resonant behaviour about f_{IDT} which can be referred to as IDT resonance.

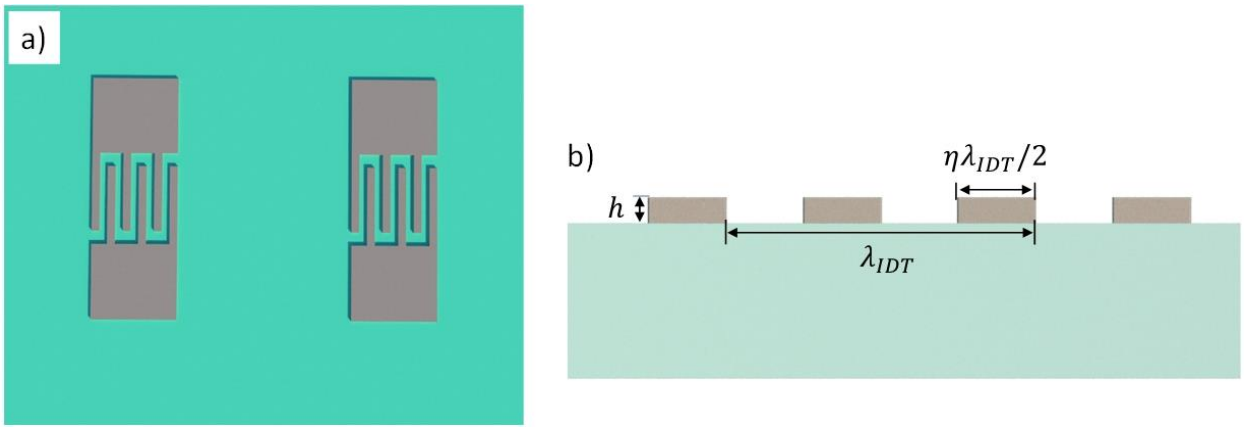

Figure 3: a) Overhead view of two interdigital transducers (IDTs) with a free surface length separating them, forming a 2-port SAW delay line. b) Cross-sectional view of electrode fingers on top of a piezoelectric substrate. h is the electrode height, λ_{IDT} is the pitch of the IDT, and η is the metallization ratio.

As mentioned previously, IDTs can also be used to detect SAWs. When a travelling SAW passes through an IDT, the associated potential wave generates a potential difference between the IDT electrodes, which can be detected using an oscilloscope, for example. IDTs also demonstrate a similar resonance about f_{IDT} for SAW detection, the potential difference generated between electrodes being maximal when the SAW wavelength matches the pitch of the IDT.

The geometric parameters of an IDT will determine its response. As mentioned previously, the IDT pitch, λ_{IDT}, determines the peak frequency of the IDT resonance. The number of IDT finger pairs, n, impacts both the amplitude and Q-factor of the IDT resonance. Since each finger pair can be considered as an acoustic source, increasing the number of finger pairs leads to a larger total SAW output when SAWs from each pair are in phase, however more destructive interference occurs when SAWs are detuned, leading to sharper resonances. The metallization ratio, η, describes the fraction of the substrate surface that is covered with metal in the IDT region, the width of the IDT fingers can then be represented as $\eta\lambda_{IDT}/2$ (η ranges from 0 to 1). As η increases, IDT fingers become increasingly spatially distributed along the SAW propagation direction, allowing for a larger number of frequencies about f_{IDT} to better satisfy the phase condition required for IDT resonance and leading to lower Q-factors. The height of the IDT fingers, h,

affects the velocity mismatch between metallized and free surface regions, and thus impacts the magnitude of the reflection and scattering of SAWs at IDT fingers.

It should also be noted that IDTs act not only as transducers but also as acoustic Bragg reflectors. SAWs are partially reflected by each IDT finger, and since IDT fingers are spaced out at intervals of $\lambda_{IDT}/2$, the phase difference between SAWs reflected at successive fingers will be 2π when the SAW wavelength is equal to λ_{IDT}. Thus, not only is the IDT (transduction) resonance centered about f_{IDT} but so is the IDT's reflectance band. This effect limits the number of fingers an IDT can have, as beyond a certain number of fingers the transmission through the IDT is zero.

1.2.2 Characterization

An IDT delay line, as shown in Figure 3a, can be regarded as a two-port network as shown in Figure 4.

Figure 4: Graphic representation of a 2-port network where V_{iI} and V_{iO} are the input and output voltages of port i, respectively.

A two-port network can be described mathematically as [13]:

$$\begin{pmatrix} V_{1O} \\ V_{2O} \end{pmatrix} = \begin{pmatrix} S_{11} & S_{12} \\ S_{21} & S_{22} \end{pmatrix} \begin{pmatrix} V_{1I} \\ V_{2I} \end{pmatrix}$$

where V_{iI} is the input voltage to port i, V_{jO} is the output voltage of port j, and S_{ij} are the scattering parameters. The scattering parameters can be divided into two groups: the reflection parameters ($S_{ij}, i = j$) and the transmission parameters ($S_{ij}, i \neq j$). The scattering parameters can be written explicitly as

$$S_{11} = \left.\frac{V_{1O}}{V_{1I}}\right|_{V_{2I}=0} \quad S_{22} = \left.\frac{V_{2O}}{V_{2I}}\right|_{V_{1I}=0} \quad S_{21} = \left.\frac{V_{2O}}{V_{1I}}\right|_{V_{2I}=0} \quad S_{12} = \left.\frac{V_{1O}}{V_{2I}}\right|_{V_{1I}=0}$$

All the scattering parameters are frequency dependent and can be measured using standard network analysis tools and techniques.

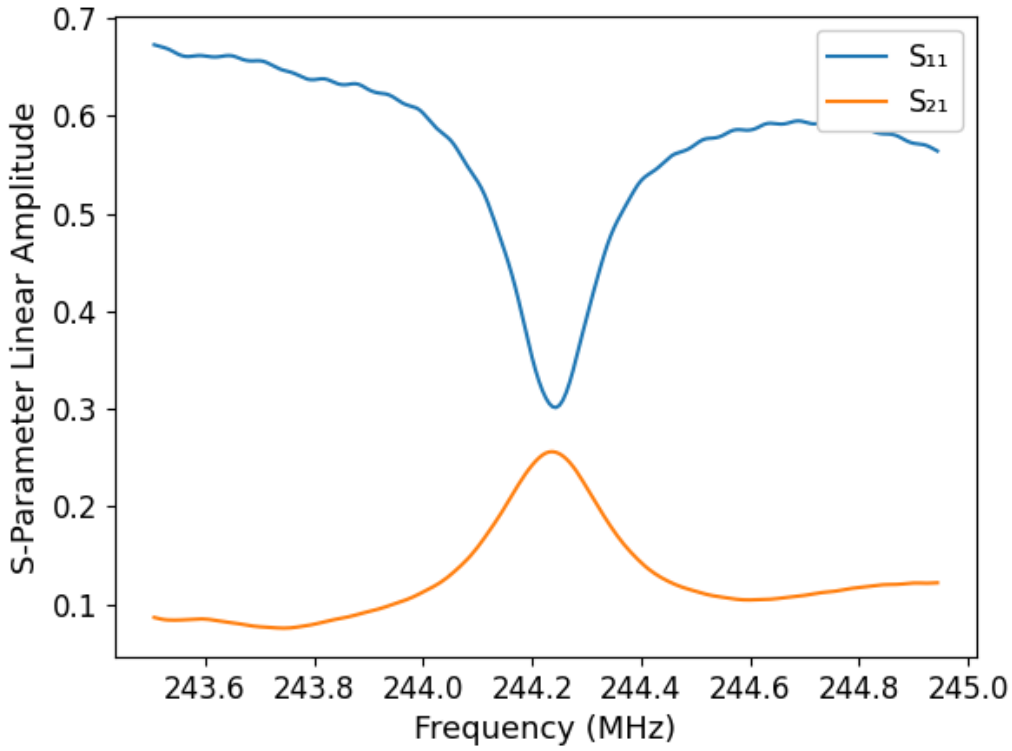

Figure 5: Measured S_{11} (reflection at port 1) and S_{21} (transmission from port 1 to port 2) spectra for a 2-port SAW device with a 1 mm separation between IDTs. The frequency of minimum reflection corresponds to the frequency of maximum transmission, indicating that the resonances in both spectra correspond to SAW generation.

When IDTs are measured using a vector network analyzer (VNA), IDT resonance can be observed as a dip in the frequency response of the electrical S_{11} (reflection) parameter, as seen in Figure 5. This is because electrical power escapes due to the electrical coupling into SAW modes (and some other acoustic modes to a lesser degree), thus there is less power reflected back to the electrical source by port 1. It can be confirmed that energy is in fact being lost to SAWs by using a 2-port configuration and observing the transmission from one IDT to the next, as possible in an S_{21} measurement, also displayed in Figure 5. It can be seen that the dip in the S_{11} spectrum aligns with the peak in the S_{21}, thus acoustic energy dissipated by one IDT is being received at the other. And since IDTs exist on the substrate surface, the acoustic energy must be confined to the surface for efficient transmission between IDTs, thus we can conclude that the resonances in the measured S spectra are in fact due to electrical coupling to SAW modes. It may be noted

that the reduction in S_{11} at SAW resonance is larger than the increase in S_{21}. This is primarily because standard IDTs are bidirectional devices, meaning they generate SAWs in both the +ve and -ve directions perpendicular to the IDT fingers on the substrate surface. Thus, there is at best a 50% transmission of SAW power from the transmitting IDT to the receiving IDT. Other asymmetries between S_{11} and S_{21} are similarly due to the irradiation of electrical power into modes which cannot be retrieved at the receiving IDT, *e.g.*, bulk acoustic wave modes and off-axis SAW modes.

1.3 Fabrication methods and challenges for high-frequency SAW devices

It is well known that SAW sensors become more sensitive at higher operating frequencies [14]. Since the operating frequency of a SAW device is approximately given by $f_{IDT} = v_{SAW}/\lambda_{IDT}$, λ_{IDT} should be minimized for high frequency operation. However, the operating frequencies of SAW devices are limited by the smallest resolvable feature size of the employed fabrication technique, which must be less than the minimum feature size in the SAW device (which for a standard IDT is $\lambda_{IDT}/4$). Thus, a high-resolution fabrication technique should be used for high frequency SAW device fabrication.

Photolithography, a fabrication method used for patterning films on a substrate, is frequently used for the fabrication of SAW devices. Photolithography can generally be applied in two different techniques: wet etching and lift-off. Wet etching is a method where a film is deposited directly onto a substrate and a layer of photo sensitive material - photoresist (PR) - is applied on top. When exposed to UV light, PR becomes soluble in its developer. By exposing select regions of the PR with UV light using a photomask, the exposed regions of PR can be dissolved (with developer) and the remaining PR can then function as an etching mask. By submerging the substrate into a wet chemical etchant, unwanted material can be removed leaving behind the desired patterns. While this method is effective, the wet chemistry used for etching can damage the substrate or underlying materials [15]. Wet etching of metal films tends to reveal their grain structure, resulting in rough metal edges in the final devices. Alternatively, lift-off photolithography involves applying photoresist to the substrate directly, then exposing and developing the photoresist,

followed by depositing a film on top. Unwanted film is then "lifted off" by stripping the photoresist underneath it with a chemical solvent. Clean lift-off can be ensured by the addition of a layer beneath the photoresist - lift-off resist (LOR). LOR is etched isotropically by the developer, thus after developing through the PR layer the LOR will be developed underneath the PR, creating a re-entrant sidewall profile. A re-entrant sidewall profile ensures a detached film deposition and allows for the stripping solvent to contact the LOR and PR directly, leading to good lift-off. However, development of the LOR layer can be difficult to control due to it being coupled to the PR development. If the LOR layer is underdeveloped there will be a lack of re-entrant sidewall profile and if the LOR is overdeveloped, it will not be able to support the PR above it leading to lithographic collapse. When fabricating small features, undercut development becomes increasingly difficult and often limits the achievable resolution. Although the resolution associated with lift-off is consequently lower than wet etching, lift-off is still often the better choice as it does not impact or damage the substrate surface and produces sharp edges in the final devices. For these reasons, lift-off photolithography has been frequently employed for the fabrication of SAW devices [16].

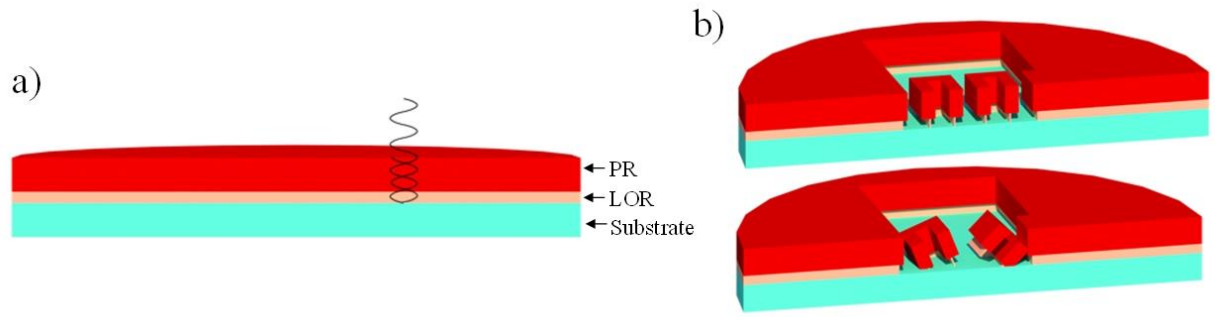

Figure 6: Sources of failure in traditional bi-layer photolithography. a) Standing wave exposure produced from reflection of exposure light at the substrate. b) Lithographic collapse due to overdeveloping of LOR undercut.

The resolution of the chosen fabrication technique is strongly dependent on the wavelength of the exposure light. UV contact photolithography, the most common and accessible technique, often uses an exposure wavelength of 365 nm (I-line). SAW devices fabricated through UV photolithography have features typically limited to about 2-3 microns [17], [18] which limits the fundamental SAW operating frequency to below 500 MHz on lithium niobate. Alternatively, higher frequency SAW devices can be achieved by reducing the exposure wavelength, as demonstrated with x-ray lithography [19], ion projection

lithography [20], and electron beam lithography [21]. While high frequency (up to 1.89 GHz) SAW devices have been realized with these methods, they require expensive equipment or are serial processes which do not scale easily. Thus, a lift-off UV contact photolithography process for SAW devices which can reliably produce micron sized features, enabling near GHz fundamental operating frequencies on lithium niobate, would be highly useful.

1.4 Measurement of velocity, attenuation, and reflection in SAW devices

In designing SAW devices such as 2-port SAW resonators, parameters such as the free surface SAW velocity, SAW attenuation, and IDT reflection are critical. SAW velocity is often experimentally determined by measuring the fundamental operating frequency of the device then multiplying by λ_{IDT} ($v_{IDT} = f_0 \cdot \lambda_{IDT}$) [22], [23]. However, the obtained velocity is for SAWs overlapping with the IDT, which differs from the free surface SAW velocity because of piezoelectric stiffening and mass loading introduced by the IDT [3]. Alternatively, a SAW pulse can be transmitted between two IDTs and its delay time can be used to calculate the free surface SAW velocity [22], [24]. However, IDTs are spatially distributed along the SAW propagation axis, so the propagation distance is not well defined. Also, the impact on SAW velocity of the IDT regions introduces further error. Means of accurately measuring free surface SAW velocity have been proposed as specialized IDT configurations [25] or by implementing a direct electrical coupling path between 2-port SAW delay lines with different delay line lengths [26], but such specialized designs have no further use. It is also possible to obtain accurate measurements of the free surface SAW velocity by using an optical probe, where the velocity can be measured accurately from the angle of acousto-optically diffracted light [27] or from an optical ‘’sing-around’ method [28].

Additionally, SAW attenuation has been measured primarily using optical probes, most notably by measuring the power of acousto-optically diffracted light [27], [29], or detecting surface displacements using a Michelson interferometer [30] at different SAW propagation distances. However, the requirement

of an optical setup in addition to the electrical setup needed for SAW excitation makes these methods impractical or inaccessible in many lab environments.

Accurate measurement of the reflection coefficient frequency response of metallized strips on the substrate surface has been demonstrated through time gated S-parameter measurements [31]. The measurement of SAW velocity, attenuation, and reflection has been demonstrated using a 2-port SAW resonator, where SAW parameters were varied until agreement was reached between calculated and measured transfer functions [32]. While this method allows for synchronous measurement of various SAW parameters, it requires an unintuitive and complex calculation procedure.

1.5 SAW strain sensors

SAW devices as strain sensors has received considerable interest due to their low power consumption, wafer-scale fabrication, sensitivity, robustness, passive implementation, and ability to be remotely interrogated, making them ideal sensors for rugged conditions as required in the aerospace, automotive, and civil engineering fields. Compared to alternatives such as piezoresistive [33], [34] or optical fiber strain sensors [35], [36], SAW sensors have superior dynamic range, low system complexity, and are inexpensive.

Surface acoustic wave devices used as strain sensors are based on three main design configurations. The first and simplest form of a SAW strain sensor is the resonant interdigital transducer (IDT), where the resonant frequency is used as the measurand. When strained, the SAW velocity and pitch of the IDT are affected, leading to shifts in the IDT's resonant frequency. Resonant IDT strain sensors have been demonstrated as 1-port [37], [38], [39] and 2-port devices [40], [41]. Another common design is the SAW oscillator, which uses two IDTs in a "sing-around" configuration to generate high quality factor resonant modes [42], [43], [44]. SAWs produced by a transmitting IDT are converted to an electrical signal at a receiving IDT, then amplified and routed back to the transmitting IDT, causing the system to oscillate when the total phase per system round trip is an integer multiple of 2π. When the substrate is strained, both the

distance between the IDTs and the SAW velocity in the substrate are affected, producing a shift in the oscillation frequencies. Finally, SAW strain sensors have been demonstrated using the reflective delay line, where the change in phase of a SAW signal produced by an IDT, travelling to and from a reflection array under strain, is measured [45], [46].

1.6 Thesis objectives

The objective of this thesis is to develop methods for the fabrication, and characterization of 2-port surface acoustic wave (SAW) resonators, as well investigate the use of their Fabry-Pérot resonance modes for strain sensing. UV photolithography is commonly used as the fabrication method for SAW devices, however, the resolution limit of existing UV photolithography techniques prevents the realization of high-frequency devices. A photolithography technique that can achieve high-resolution (1 μm) while also being compatible with piezoelectric/pyroelectric materials used for SAW devices would be highly useful for researchers. Additionally, the characterization of SAW cavities has been demonstrated using various techniques in the literature, but an intuitive technique to simultaneously obtain key SAW parameters such as velocity and attenuation is absent. This thesis works to develop a novel and intuitive method of characterizing SAW cavities based on optical Fabry-Pérot cavity theory to allow for simultaneous measurement of cavity parameters. Finally, SAW strain sensors have been previously demonstrated, primarily using the designs of the SAW oscillator and 1-port SAW resonator. This thesis strives to demonstrate a high-resolution SAW strain sensor by creating a device based on Fabry-Pérot resonances in a 2-port SAW resonator.

1.7 Thesis outline

This thesis includes three research articles. Chapter 2 presents a fabrication method for high frequency SAW devices based on a tri-layer lift-off photolithography technique and demonstrates the fabrication and operation of SAW devices with a 1 GHz operating frequency. The fabricated devices are

electrically characterised and compared with numerical results to good agreement. The article in this chapter is in its “as submitted” format. Chapter 3 describes a method for measuring the velocity, attenuation, and reflection within a SAW cavity through the acoustic Fabry-Pérot spectra. Optical theory is adapted for acoustic waves to derive expressions for the free spectral range and linewidth of cavity resonances. Resonances are measured for various cavity lengths to obtain various SAW parameters. The article in this chapter is in its “as submitted” format. Chapter 4 demonstrates a high-resolution strain sensor based on Fabry-Pérot resonances from a 2-port SAW resonator. A theoretical analysis is presented to estimate the sensitivity of the device and to predict strain distributions in the employed straining setup. Then, the frequency stability of resonance peaks was measured and compared for resonators of different lengths. A cross-correlation analysis technique is then introduced to improve the detection of the frequency shift of SAW resonances and enable multimode frequency shift detection. Finally, the sensitivity of a 10 mm long resonator is measured, and its strain resolution is obtained. The article in this chapter is in its “as submitted” format. Chapter 5 serves to conclude the thesis and provides suggestions for future work.

Chapter 2 – Fabrication of high frequency SAW devices using tri-layer lift-off photolithography

2.1. Summary

In this chapter a tri-layer lift-off photolithography technique is presented to enable the fabrication of surface acoustic wave (SAW) devices with near GHz fundamental operating frequencies. The sensitivity of SAW sensors is known to improve with frequency, however high frequency SAW devices require high-quality micron-scale features for high frequency operation, a requirement that challenges traditional UV photolithography techniques. The presented process is a modified version of a previously reported tri-layer photolithography process intended for Si and SiO_2 substrates which allows for compatibility with materials that are piezoelectric and pyroelectric, often used as the substrate in SAW devices. The process uses a lithographic tri-layer consisting of layers of lift-off resist (LOR) on the bottom, back anti-reflection coating (BARC) in the middle, and photoresist (PR) on top. The addition of the BARC layer prevents back reflection of exposure light, improves the structural integrity of the lithographic stack, and decouples the PR and LOR development, improving resolution by a factor of two over traditional lift-off photolithography techniques. We demonstrate the fabrication of a SAW device with an interdigital transducer (IDT) pitch of 4 μm (minimum feature size of 1 μm) on 128° Y-X cut lithium niobate. The device produces a dip in the measured S_{11} spectrum at 994.5 MHz, corresponding to the fundamental operating frequency of the device. The fundamental operating frequency of the SAW device is also determined theoretically via numerical modelling and found to be 995.5 MHz. The process thus enables the reliable fabrication of high frequency SAW devices that can be used as highly sensitive strain sensors.

2.2. Work contribution

In this work, a tri-layer lift-off photolithography process is introduced to push the resolution limit of UV photolithography techniques for SAW device fabrication. Bi-layer lift-off photolithography, which is the traditional UV lift-off photolithography method for SAW device fabrication, has a resolution limit of 2 μm. The resolution is limited not only by diffraction patterns resulting from the interference of exposure light from adjacent apertures in the photomask, but also by standing wave exposures due to reflection of the exposure light at the substrate and by difficulties in undercutting the LOR beneath the PR layer without over-developing and causing lithographic collapse. Our tri-layer photolithography adds a layer of back anti-reflective coating (BARC) to eliminate back reflections of the exposure light and decouple PR and LOR development, resulting in much better control of undercut development. Due to these advantages, the tri-layer lift-off photolithography method has a minimum resolution of 1 μm, improving resolution and SAW device operating frequency by a factor of 2 over traditional techniques. Thus, our process will help researchers to realize higher frequency SAW devices using standard UV photolithography equipment.

2.3. Article

The following article was published in Microelectronic Engineering, 253 (Jan 2022).

Fabrication of High Frequency SAW Devices using Tri-Layer Lift-Off Photolithography

Liam Kelly,[1,2] Howard Northfield,[2] Sabaa Rashid,[2] Xiaoyi Bao,[1,2] Pierre Berini[*,1,2,3]

[1]Department of Physics, University of Ottawa, Ottawa ON, K1N 6N5, Canada
[2]Centre for Research in Photonics, University of Ottawa, Ottawa ON, K1N 6N5, Canada
[3]School of Electrical Engineering and Computer Science, University of Ottawa, Ottawa ON, K1N 6N5, Canada

Keywords: Photolithography, Surface acoustic waves, High-resolution, High frequency

Abstract

A tri-layer lift-off photolithography technique is presented to enable the fabrication of surface acoustic wave (SAW) devices with near GHz fundamental operating frequencies. SAW devices require high-quality micron-scale features for high frequency operation, a requirement that challenges traditional UV photolithography techniques. The presented process is a modified version of a previously reported tri-layer photolithography process intended for Si and SiO_2 substrates which allows for compatibility with materials that are piezoelectric and pyroelectric, often used as the substrate in SAW devices. The process uses a lithographic tri-layer consisting of layers of lift-off resist (LOR) on the bottom, back anti-reflection coating (BARC) in the middle, and photoresist (PR) on top. The addition of the BARC layer prevents back reflection of exposure light, improves the structural integrity of the lithographic stack, and decouples the PR and LOR development, improving resolution by a factor of two over traditional lift-off photolithography techniques. We demonstrate the fabrication of a SAW device with an interdigital transducer (IDT) pitch of 4 μm (minimum feature size of 1 μm) on 128° Y-X cut lithium niobate. The device produces a dip in the measured S_{11} spectrum at 994.5 MHz, corresponding to the fundamental operating frequency of the device. The fundamental operating frequency of the SAW device is also determined theoretically via numerical modelling and found to be 995.5 MHz. The process thus enables the reliable fabrication of high frequency SAW devices that exhibit excellent agreement with numerical results.

1. Introduction

Surface acoustic wave (SAW) devices typically consist of one or two interdigital transducers (IDTs) which are fabricated on the surface of a piezoelectric substrate. When an AC signal is applied across the electrodes of the IDT, an electric potential distribution is generated in the substrate which overlaps with and excites SAW modes. The excitation of SAWs is maximal when the SAW wavelength (λ_{SAW}) corresponding to the frequency of the applied electrical signal is roughly equal to the pitch of the IDT (λ_{IDT}):

$$\lambda_{SAW} = \frac{v_{SAW}}{f} = \lambda_{IDT}$$

Thus, at a signal frequency of $f = v_{SAW}/\lambda_{IDT}$, the SAW device demonstrates resonant behaviour. This frequency is known as the fundamental operating frequency of the SAW device. The SAW device's resonant behaviour can be observed through the frequency response of the electrical S_{11} (reflection) and S_{21} (transmission) scattering parameters. Owing to this resonant behaviour, SAW devices originally gained immense popularity as electrical bandpass filters for communication devices [1], and have now found interest as temperature, strain, and chemical vapour sensors [2]. Since these sensors become more compact and sensitive at higher frequencies, there is a demand for GHz range SAW devices and fabrication processes which can realize short IDT pitches and micron-scale features.

Photolithography, a fabrication method used for patterning films on a substrate, is frequently used for the fabrication of SAW devices. Photolithography can generally be applied in two different techniques: wet etching and lift-off. Wet etching is a method where a film is deposited directly onto a substrate and a layer of photo sensitive material - photoresist (PR) - is applied on top. When exposed to UV light, PR becomes soluble in its developer. By exposing select regions of the PR with UV light using a photomask, the exposed regions of PR can be dissolved (with developer) and the remaining PR can then function as an etching mask. By submerging the substrate into a wet chemical etchant, unwanted material can be removed leaving behind the desired patterns. While this method is effective, the wet chemistry used for etching can damage the substrate or underlying materials [3]. Wet etching of metal films tends to reveal their grain structure, resulting in rough metal edges in the final devices. Alternatively, lift-off photolithography involves applying photoresist to the substrate directly, then exposing and developing the photoresist, followed by depositing a film on top. Unwanted film is then "lifted off" by stripping the photoresist underneath it with a chemical solvent. Clean lift-off can be ensured by the addition of a layer beneath the photoresist - lift-off resist (LOR). LOR is etched isotropically by the developer, thus after developing through the PR layer the LOR will be developed underneath the PR, creating a re-entrant sidewall profile. A re-entrant sidewall profile ensures a detached film deposition and allows for the stripping solvent to contact the LOR and PR directly, leading to good lift-off. However, development of the LOR layer can be difficult to control due to it being coupled to the PR development. If the LOR layer is underdeveloped there will be a lack of re-entrant sidewall profile and if the LOR is overdeveloped, it will not be able to support the PR above it leading to lithographic collapse. When fabricating small features, undercut development becomes increasingly difficult and often limits the achievable resolution. Although the resolution associated with lift-off is consequently lower than wet etching, lift-off is still often the better choice as it does not impact or damage the substrate surface and produces sharp edges in the final devices. For these reasons, lift-off photolithography has been frequently employed for the fabrication of SAW devices [4].

The resolution of the chosen fabrication technique is strongly dependent on the wavelength of the exposure light. UV contact photolithography, the most common and accessible technique, often uses an exposure wavelength of 365 nm (I-line). SAW devices fabricated through UV photolithography have features typically limited to about 2-3 microns [5], [6] which limits the fundamental SAW operating frequency to below 500 MHz on lithium niobate. Alternatively, higher frequency SAW devices can be achieved by reducing the exposure wavelength, as demonstrated with x-ray lithography [7], ion projection lithography [8], and electron beam lithography [9]. While high frequency (up to 1.89 GHz) SAW devices have been realized with these

* Corresponding author at: Center for Research in Photonics, University of Ottawa, Ottawa, Ontario K1N 6N5, Canada.

methods, they require expensive equipment or are serial processes which do not scale easily. Thus, a lift-off UV contact photolithography process for SAW devices which can reliably produce micron sized features, enabling near GHz fundamental operating frequencies on lithium niobate, would be highly useful.

We propose a modified version of a previously reported tri-layer lift-off contact photolithography process intended for SiO_2 or Si substrates [10]. Our modified version was created for compatibility with substrate materials that are piezoelectric and pyroelectric, as often used for SAW devices (*e.g.*, lithium niobate and lithium tantalate), imposing strict limits on thermal processing steps. The tri-layer process uses a BARC layer which prevents back reflection of exposure light, improves the structural integrity of the lithographic stack, and decouples the PR and LOR development steps enabling reliable fabrication of 1 µm feature sizes and high frequency SAW devices. Additionally, as a lift-off process, the substrate surface (and pre-existing structures on the surface) remains unaffected. The process does not involve the use of acids and complicated chemistries, and clean edges are produced in the final devices. We demonstrate the process in the reliable fabrication of IDTs with a 4 µm pitch (1 µm linewidths) on 128° Y-X cut lithium niobate using standard UV photolithography equipment. We also present a modified thick metal tri-layer lift-off photolithography process which can be used to realize thick electrical contact pads without damaging pre-existing IDT patterns. We demonstrate application of the process by fabricating and testing a SAW device and comparing the measurements with theory.

2. Fabrication

Our photolithography process uses a tri-layer lithographic stack to enable higher resolution than the traditional lithographic bi-layer. The tri-layer, as detailed in [10], consists of the traditional layers of lift-off resist (LOR) on the bottom and photoresist (PR) on the top with an additional layer of back anti-reflection coating (BARC) in the middle. The addition of the BARC layer serves three main functions: (i) It prevents back reflection of the exposure light at the substrate from re-entering the PR layer, preventing spurious exposure of the PR. (ii) The BARC layer adds additional structural stability, further reducing the risk of lithographic collapse. (iii) It decouples the development of the PR and LOR as BARC is not soluble in developer. Since the LOR layer can be developed independently, there is much greater control of the re-entrant sidewall profile development, with less risk of lithographic collapse (over-development) or a shallow re-entrant sidewall profile (under-development). These three functions provided by the BARC layer help improve the resolution limit of the process over traditional single- or bi-layer lift-off photolithography techniques.

Substrates which are used for SAW devices are piezoelectric and often pyroelectric (*e.g.*, lithium niobate and lithium tantalate), making them incompatible with the thermal ramping and cooling steps in typical photolithography processes. This incompatibility arises from the substrate generating an internal electric field between its surfaces when subjected to a high temperature through the pyroelectric effect, and then producing mechanical deformations in response to the electric field through the piezoelectric effect. When these mechanical deformations exceed the elastic limit, the wafer will crack or shatter. This was confirmed to be the case when a lithium niobate wafer was placed directly onto a 190 °C hotplate (following the unmodified tri-layer process) and broke almost instantly. To circumvent this issue, the previously reported tri-layer photolithography technique was modified so that a ramp of 2 °C/min was used for all heating and cooling steps. All baking, exposure, development, and etching stages consequently required re-optimization.

Lithium niobate, which was used as the substrate in developing this process, is very brittle. When spin coating the wafer, the vacuum from the spin coater caused the wafer to deform to the point of breakage. To mitigate this issue, the lithium niobate wafer was affixed to the top of a silicon (Si) wafer prior to the first spinning step to reduce the strain imparted on the lithium niobate wafer. The wafers were affixed by painting a thin layer of SPR 955 around the perimeter of the Si wafer surface, then placing the lithium niobate wafer on top. By ramping the wafer stack to a temperature of 155 °C, strong adhesion was achieved, and despite differences in thermal expansion coefficient between lithium niobate and silicon, the wafer stack remained stable during thermal cycling. The decrease in temperature at the lithium niobate surface due to the Si "support" wafer when heating was accounted for by increasing all hotplate baking temperatures listed in Table 1 and Table 2 by 2 °C.

The steps of the modified tri-layer lift-off photolithography process are visualized in the flow diagram in

Figure 1. Two versions of the process are presented: a process to lift-off thin films (< 200 nm) which provides the best resolution and is intended for fine features such as IDT fingers, and a process to lift-off thick films (200-1000 nm) which can be used for larger features such as metal contact pads. The process was designed for and performed on 500 µm thick single-side polished 128° Y-X cut lithium niobate wafers, although it is expected to be transferrable to any piezoelectric/pyroelectric material that can withstand a thermal ramp of 2 °C/min. Microposit LOR-1A [11] was used for the LOR layer, Microposit XHRiC-16 [12] which is optimised to absorb I-line exposure was used for the BARC layer, and Megaposit I-line optimised SPR955-0.7 positive photoresist [13] was used as the top PR layer. The exposure wavelength used was 365 nm (I-line).

2.1 Process to Lift-Off Thin Films (< 200 nm)

Table 1 summarizes the process steps of the tri-layer photolithography process to lift-off thin films, which can be used to fabricate fine features as small as 1 µm in films as thick as 200 nm. The wafers were hand cleaned using isopropyl alcohol (IPA) and optical wipes, followed by submersion in acetone, IPA, and de-ionised (DI) H_2O baths to remove any contaminants on the wafer surface. The LOR layer was then spin-applied to the wafer, then placed on a hotplate where it was baked[2] at a temperature of 160 °C for 6 min. Then the BARC layer was applied, followed by a 60 s vacuum-off post-spin relax (PSR) before baking[2] at 150 °C for 1 min. Finally, the top PR layer was spin-applied on top of the BARC layer, followed by a 60 s PSR, then baked[2] at 90 °C for 3 min. It may be noted that the baking temperatures and times were lower and longer than those previously reported [10]. By using a lower baking temperature, a longer baking time is required to evaporate an equivalent amount of solvent in the lithographic materials. However, the concentration of solvents approaches a steady state at longer baking times, greatly reducing the need for timing accuracy when baking. This plays a crucial role when using ramped bakes, which can make controlling baking time much more difficult.

I-line exposure of the PR layer was carried out through a photomask using an OAI 200IR contact mask aligner fitted with I-line band-pass filters. When using 3 I-line filters, the I-line intensity was measured as ~ 7 mW/cm^2. To get the best feature resolution, the exposure dose was optimized over many trials to 80 mJ and hard contact was used between the mask and the substrate. Hard contact minimizes the distance between the mask and PR layer, also minimizing the diffraction of exposure light through the photomask. Diffraction patterns in the PR are thus also minimized, helping to prevent unwanted exposure and maintain resolution. However, during fabrication, we still observed diffraction patterns in some locations on the wafer as the wafer and resist thicknesses are not uniform over the 4" wafer, leading to variation in PR-to-mask uniformity. Resolution is improved by ensuring that the layers in the tri-layer are uniform post-spin and do not contain particulates. After exposure, a post-exposure bake at 120 °C for 3 min was performed.[1]

[1]All baking stages used heating and cooling ramps of 2 °C/min to reach and cool from baking temperatures.

Table 1: Process steps for the modified tri-Layer lift-off contact photolithography process.

Step	Description	Details
1	LOR-1A Application	Slow* spin (~225 nm) followed by 6 min bake† @ 160 ˚C.
2	BARC Application	Fast* spin (~225 nm) followed by 60 s vacuum off post spin relax. 1 min bake† @ 150 °C.
3	SPR 955 Application	Fast* spin (~600 nm) followed by 60 s vacuum off post spin relax. 3 min bake† @ 90 °C.
4	UV Exposure	80 mJ exposure dose with hard contact between mask and substrate. 3 I-line (365 nm) pass UV filters were used yielding a ~7 mW/cm^2 intensity.
5	Post Exposure Bake	Bake† for 3 min @ 120 °C.
6	PR Development	4 min in CD-26 with 80 kHz ultrasound bath at 30% max power for 10 s intervals at 1, 1.5, 2.5, 3.5 min followed by DI H_2O bath.
7	Post Development Bake	Bake† for 3 min at 150 °C to desensitize photoresist to incidental UV exposure.
8	RIE of BARC	SAMCO 10-NR RIE: 25 W, 7 min, 4 Pa, 10 sccm O_2.
9	Undercut Development	3 s Dip in MF-24A bath followed by DI H_2O bath.
10	Metal Deposition	Angstrom E-beam Deposition Chamber: 100 nm of Al (Can be replaced with choice of metal up to a thickness of ~200 nm)
11	Lift-off	1-2 hr submersion in covered Remover PG bath @ 75 °C followed second 1-2 hr Remover PG bath @ 75 °C and then by 5 min IPA and 5 min DI H_2O baths.
12	Optional Additional Thick Metal Layer	Additional thick metal films can be patterned using our modified thick metal tri-layer photolithography process. Its details can be seen in the supplementary materials.

*LOR, BARC, and PR application spins:
Fast: (15 s @ 200 r/s) + (10 s @ 3000 rpm) + (15 s @ 200 r/s) + (30 s @ 6000 rpm) + (6 s @ -1000 r/s)
Slow: (5 s @ 200 r/s) + (5 s @ 1000 rpm) + (4 s @ 500 r/s) + (45 s @ 3000 rpm) + (5 s @ -600 r/s)
†All hot plate temperatures were reached from 35 °C by thermal ramping of 2 °C/min, followed by cooling back to ~35 °C. Once cooled, the lithium niobate wafer was placed on cooling rack for ~ 5 min to dissipate accumulated charge.

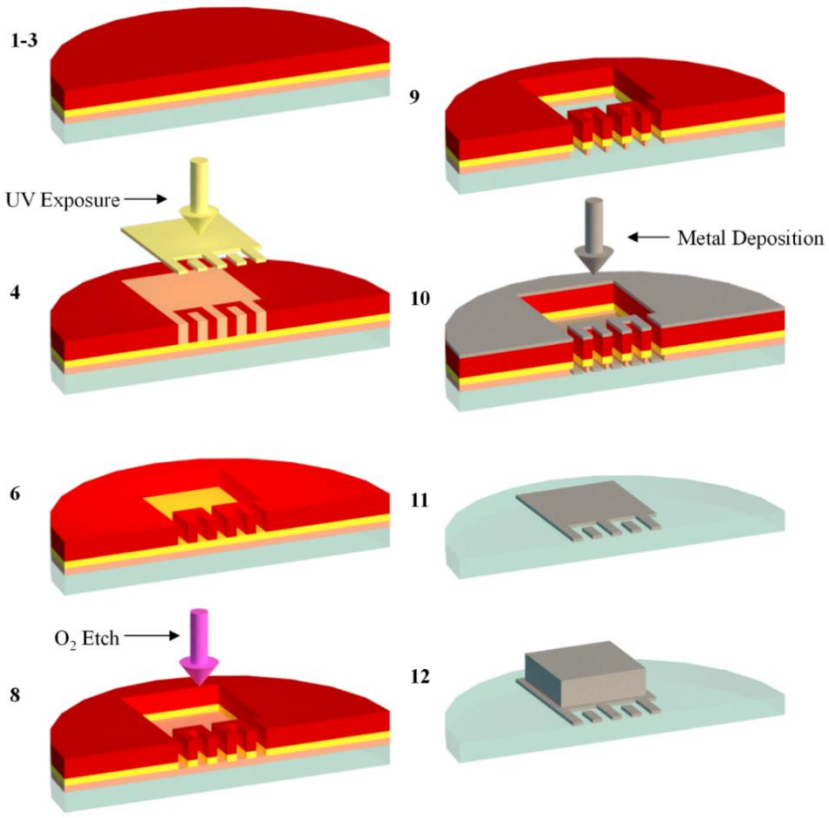

Figure 1: Process flow diagram for the modified tri-layer lift-off contact photolithography process. Numbers to the top-left of each image index the corresponding fabrication steps in Table 1. Step 1-3: tri-layer application, step 4: UV exposure, step 6: PR development, step 8: RIE of BARC, step 9: undercut development, step 10: metal deposition, step 11: lift-off, step 12: additional thick metal layer.

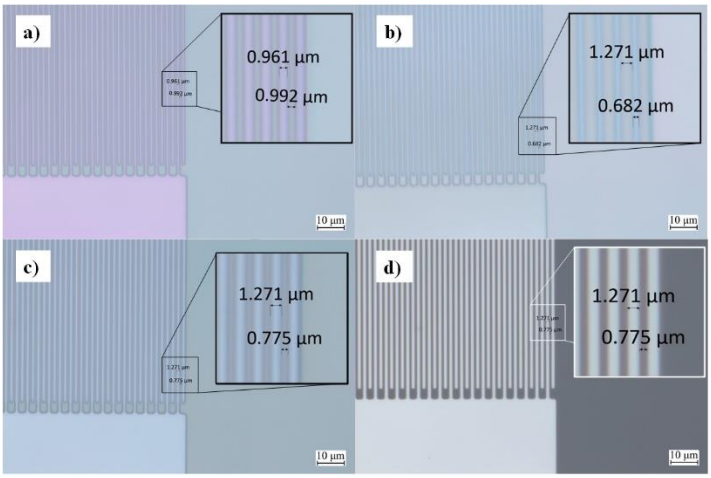

Figure 2: Optical microscope images at different processing stages when fabricating a 4 µm pitch interdigital transducer (IDT) on 128° Y-X cut lithium niobate. a) Post photoresist (PR) development. b) Post reactive ion etch (RIE) of back anti-reflection coating (BARC). c) Post undercut development. d) Post lift-off.

Next, the PR was developed to dissolve the exposed regions. The wafer was submerged in a CD-26 (TMAH-based) developer bath for 4 min. The bath was subjected to 80 kHz ultrasonication at 30% max power for 10 s intervals at 1, 1.5, 2.5 and 3.5 min. The wafer was then removed from the CD-26 bath and immediately submerged in a DI H_2O bath. After N_2 drying the wafer, a post development bake[2] at 150 °C for 3 min was performed to render the photoresist insensitive to incidental UV exposure. An optical image of the tri-layer post development can be seen in Figure 2 a).

An O_2 reactive ion etch (RIE) was then used to etch through the BARC which had been revealed post PR development. This was done using a SAMCO 10NR anisotropic RIE system. The etching power and time are crucial parameters as the BARC must be completely etched to allow for the development of the underlying LOR layer, but over etching causes erosion of the top PR layer which can lead to feature enlargement and lithographic failure. The optimal etching time was found to be 7 min when using O_2 at 25 W, 4 Pa, and 10 sccm. An optical image of the tri-layer post RIE etching can be seen in Figure 2 b), where slight feature enlargement can be observed.

The LOR layer was then developed using MF 24A developer. The LOR development must be done accurately to ensure that the substrate surface is cleared of LOR and that an undercut of ~ 100 nm under the BARC layer is created to produce a re-entrant sidewall profile. If the development time is too long, the undercut becomes too deep and the LOR layer will not be able to support the BARC layer above it, resulting in collapse of the lithographic stack. It was found that submerging the wafer in the developer for 3 s followed by immediate submersion in a DI H_2O bath produced the desired undercut. An optical image post undercut development can be seen in Figure 2 c).

Metal films can then be deposited onto the substrate. Using an anisotropic deposition method is suggested to mitigate risk of sidewall coating. In our experiment, the deposition was done using an Angstrom Nexdep e-beam deposition chamber. A thin 20 nm layer of Cr was first deposited to create good adhesion to the lithium niobate substrate, followed by a deposition of 100 nm of Al. The roughness of the metal stack was measured as Rq = 3.22 nm. It is important to note that sidewall contact will be achieved if the thickness of the metal films exceeds the thickness of the LOR layer. Thus, the thickness of metal films using this process should not exceed 175 nm. Upon removing the wafer from the chamber, it was placed in Remover PG at 75 °C for several hours to strip the remaining resist and unwanted metal from the substrate. A second Remover PG bath at 75 °C was used to remove any remaining lithographic material, followed by IPA and DI H_2O baths. The metalized structures on the substrate surface can be seen in Figure 2 d). Note that the dimensional accuracy is maintained beyond the RIE etching stage.

2.2 Process to Lift-Off Thick Films (200-1000 nm)

Table 2 summarizes the process steps of the modified tri-layer photolithography process to lift-off thick films, which can be used to fabricate features in films as thick as 1000 nm. This process is not intended for fine features (>50 µm), but rather to realize thick metal contact pads to SAW devices without risk of damaging pre-existing structures on the substrate surface. The process steps (Table 2) are carried out in the same fashion as the process for thin films (Table 1). The key difference in the thick process is that the LOR used is Microposit LOR 10B [11], a thicker LOR which will give more clearance between the deposited film and the resolution defining BARC layer. Due to changes in the LOR material, the times for all baking, exposure, development, and etching stages were reoptimized.

Table 2: Process steps for the modified Thick Metal Tri-Layer Lift-off Photolithography process.

Step	Description	Details
1	LOR-10B Application	Slow* spin (~225 nm) followed by 8 min bake† @ 165 ºC.
2	BARC Application	Fast* spin (~225 nm) followed by 60 s vacuum off post spin relax. 1 min bake† @ 155 ºC.
3	SPR 955 Application	Fast* spin (~600 nm) followed by 60 s vacuum off post spin relax. 5 min bake† @ 100 ºC.
4	UV Exposure	*80 mJ* exposure dose with hard contact between mask and substrate. 3 I-line (365 nm) pass UV filters were used yielding a ~7 mW illumination power.
5	Post Exposure Bake	Bake† for 5 min @ 125 ºC.
6	PR Development	4 min in CD-26 with with 80 kHz ultrasound bath at 30% max power for 10 s intervals at 1,1.5,2.5,3.5 min followed by Di H_2O bath.
7	Post Development Bake	Bake† for 5 min at 155 ºC to desensitize photoresist to incidental UV exposure.
8	RIE of BARC	SAMCO 10-NR RIE: 25 W, 7 min, 4 Pa, 10 sccm O_2.
9	Undercut Development	3 s Dip in MF-24A bath followed by DI H_2O bath.
10	Metal Deposition	Angstrom E-beam Deposition Chamber: 100 nm of Al (Can be replaced with choice of metal up to a thickness of ~200 nm)
11	Lift-off	Overnight submersion in covered Remover PG bath @ 55 ºC followed by 5 min IPA bath and then 5 min DI H_2O bath.

*LOR, BARC, and PR application spins:
Fast: (15 s @ 200 r/s) + (10 s @ 3000 rpm) + (15 s @ 200 r/s) + (30 s @ 6000 rpm) + (6 s @ -1000 r/s)
Slow: (5 s @ 200 r/s) + (5 s @ 1000 rpm) + (4 s @ 500 r/s) + (45 s @ 3000
rpm) + (5 s @ -600 r/s)

†All hot plate temperatures were reached from ~35 ºC by thermal ramping of 2 ºC/min, followed by cooling back to 35 ºC. Once cooled, LN wafer was placed on cooling rack for ~ 5 min to dissipate accumulated charge.

Using the thin film modified tri-layer lift-off photolithography process, SAW devices were fabricated with a 4 µm IDT pitch, 70 finger pairs, and a 240 µm aperture width. A 20 nm Cr adhesion layer followed by 100 nm of Al were used as the metal films for the IDT structures. The thick film modified tri-layer photolithography process was used to pattern 700 nm thick Al contact pads. Optical microscope images of a completed SAW device can be seen in Figure 3.

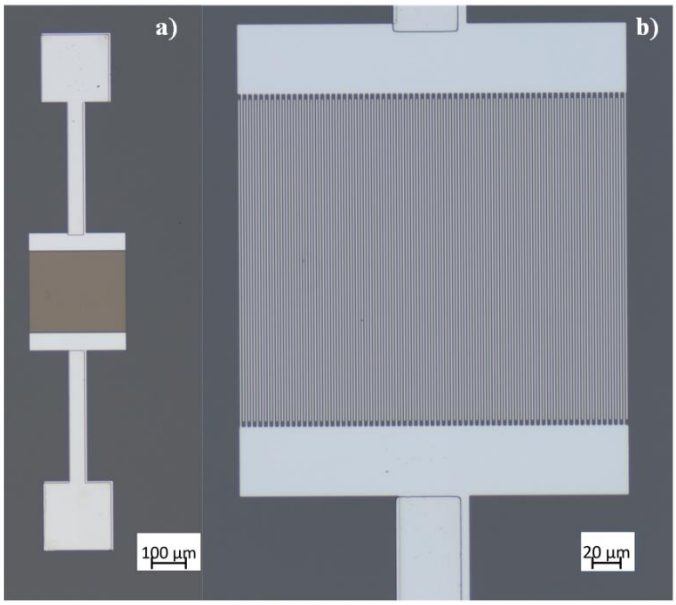

Figure 3: Optical microscope images of a realized surface acoustic wave (SAW) device with 4 µm pitch interdigital transducer (IDT) and thick metal contact pads; a) 5x magnification and b) 20x magnification.

3. Results and Discussion

3.1 High Resolution Imaging

High resolution imaging techniques were used to assess the quality of the tri-layer structure and fabricated devices. Post undercut development, a wafer was cleaved through the center of a SAW device and a cross-section was imaged using a Zeiss Gemini 500 scanning electron microscope (SEM) to reveal the structure of the tri-layer (Figure 4). The three layers of the tri-layer can be clearly observed: LOR on the bottom, BARC in the middle, and PR on the top. A trench can be seen in the top PR layer. This is attributed to diffraction occurring through the photomask and producing diffraction patterns, leading to some incidental exposure between apertures in the photomask. It is also evident that the BARC layer is the resolution defining material in the lithographic stack. Finally, a slight re-entrant sidewall profile produced from the LOR can be seen under the BARC layer, ensuring a detached film deposition and clean lift-off.

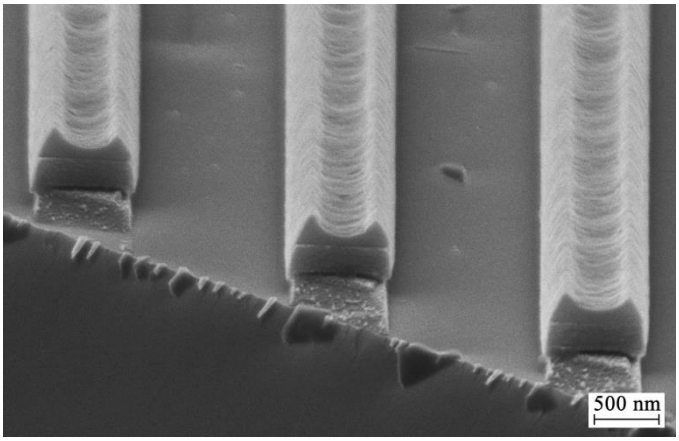

Figure 4: Scanning electron microscope (SEM) image of tri layer post undercut development. Sample was sputtered with ~ 5 nm Au to allow for the discharge of imaging electrons.

An Atomic force microscope (AFM) and a Helium Ion Microscope (HIM) were then used to characterize the quality of the fabricated structures. The AFM (Bruker Dimension Icon) was used to obtain roughness measurements of the metal films (Rq = 3.22 nm) and the substrate surface (Rq = 0.601 nm) as well as thickness measurements of the metal film (99.9 nm). Images obtained with the AFM can be seen in Figure 5. Note that the films have no "wing" structures near their edges which occur in the absence of a sidewall re-entrant profile. The substrate surface has a low roughness which is approximately equal to the substrate surface roughness before processing (Rq < 1 nm), and thus we can conclude that the substrate surface is cleared of any lithographic material or metal from deposition.

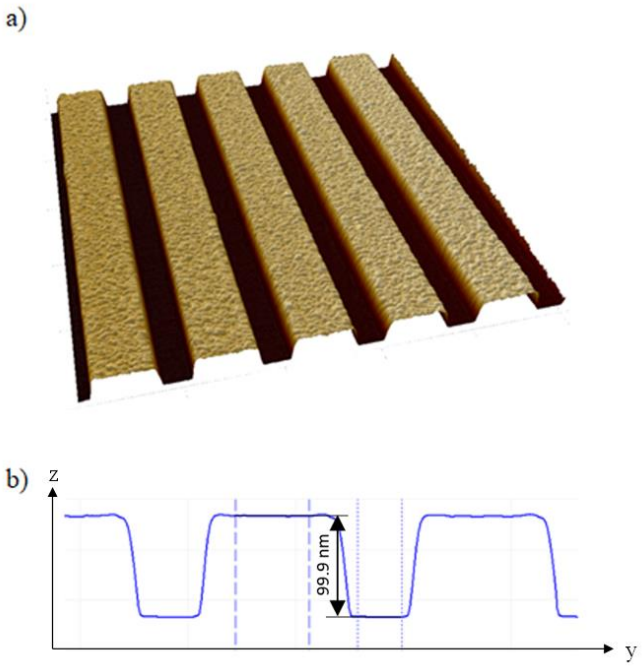

Figure 5: Atomic force microscope (AFM) image of electrodes in the center of a 4 µm pitch interdigital transducer (IDT). a) 3D image showing the fingers' structure scanned over a 10 x 10 µm area. b) Thickness measurement averaged over the length of the IDT fingers. A measurement of the film thickness is made by taking the height difference between averaged regions on the top of the metal film (long dashed line) and on the substrate surface (short dashed line) and is found to be 99.9 nm.

HIM microscopy was then used to accurately image the final devices at high resolution and with dimensional accuracy. These images are then used to determine the metallization ratio and pitch of realized devices. The HIM does not require sputtering of Au as an electron flood gun was used to neutralize the imaging He ions. High and low mag images can be seen in Figure 6 where the metallization ratio has been measured as 0.65. The pitch was also measured over many periods as 4.000 µm. While the measured pitch is equal to the design pitch of 4 µm, the measured metallization ratio deviates from the design value of 0.5. This effect is largely due to lateral widening of the lithographic openings during the RIE etching stage, leading to enlarged features. The increase in metallization will slightly affect the operating frequency and Q-factor of the SAW device's resonance peaks; however, higher metallization ratios are associated with more efficient harmonic excitation [14].

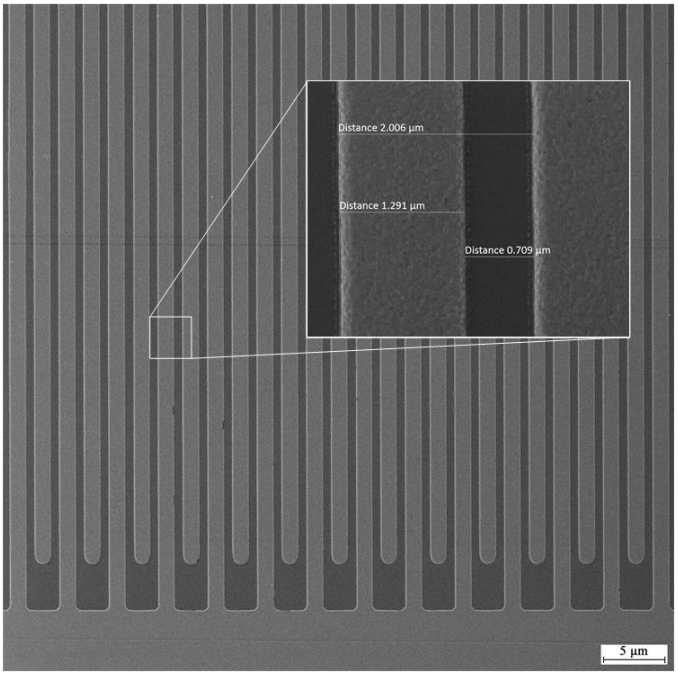

Figure 6: Helium ion microscope (HIM) image of realized surface acoustic wave (SAW) device with 4 µm pitch interdigital transducer (IDT). Inset shows a high magnification HIM image with measurements of the Al electrode finger width (1.291 µm), finger spacing (0.709 µm) and half of the IDT pitch (2.006 µm).

3.2 Assessment of Metallization Ratio

To evaluate the success of the modified tri-layer lift-off photolithography process, an analysis of the measured metallization ratio was performed. The metallization ratio was measured using a high-magnification optical microscope (Zeiss Axio Imager M2.M). Across the 30 fabricated devices, the average metallization ratio was 0.588, with values ranging from 0.531 to 0.662. The standard deviation was calculated as 0.031 (5.3%). The measured metallization ratio as a function of the radial position on wafer can be seen in Figure 7, where no clear trend is observed indicating a high uniformity across the wafer. By defining a range for yield of +/- 20% about the design metallization ratio of 0.5, 63.3% of fabricated devices are deemed to be on-spec. Additionally, yield can be defined by the percentage of wafers which do not contain defects such as broken or shorted fingers, as determined via microscope inspections. 25/30 (83%) of the fabricated devices yield successfully in this manner.

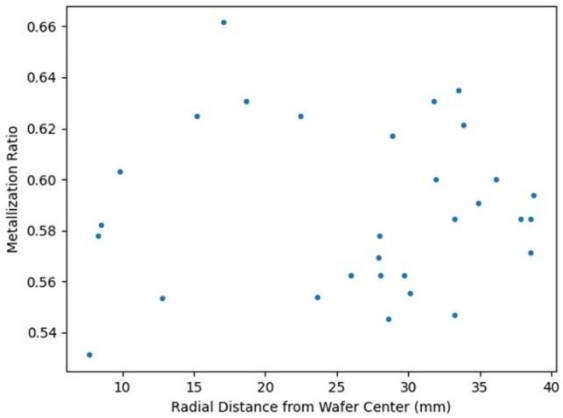

Figure 7: Measured metallization ratio for each SAW device as a function of radial distance from the center of the lithium niobate wafer.

3.3 Electrical Characterization of Devices

The fabricated SAW devices were first electrically characterized by measuring their capacitance using an HP 4284A LCR meter. The capacitance was constant over the frequency range of 10 - 500 kHz at a value of 9.27 pF.

To characterize the electro-acoustic response of fabricated SAW devices, their S_{11} scattering parameters were measured over frequency using an HP 8510 vector network analyzer (VNA). A ground-signal probe (Picoprobe, ECP18) was mounted onto an optical positioner and connected to the VNA via an SMA cable. The signal and ground tips of the probe were firmly contacted to a SAW device's contact pads. At electrical frequencies which strongly excite the SAW mode, power is dissipated through radiation of SAWs, reducing the electrical power which is reflected back to the VNA and producing a dip in the S_{11} response. As seen in Figure 8 a), there is a dip in the S_{11} spectrum at 994.5 MHz which is the frequency which best excites the SAW mode in the tested device; *i.e.*, at the fundamental operating frequency of the device.

3.4 Theoretical Modelling

To verify that the SAW device operates in accordance with theoretical expectations, a COMSOL Multiphysics simulation was performed to calculate the SAW device's fundamental operating frequency. The simulation considers a 3D unit cell of an IDT which models one finger from each electrode. Periodic boundary conditions are used, which effectively models an infinite IDT. The geometry of the device was defined such that the SAW propagation direction (perpendicular to IDT fingers) is along the computational x-axis and the substrate surface normal is parallel to the computational z-axis. The geometric parameters of the simulated device are selected to replicate the measured parameters of the fabricated device: metallization ratio of 0.65, metal film thickness of 99.9 nm, and pitch of 4 µm. The substrate height (along z-axis) was set to be 12 µm, and the substrate depth (along y-axis) was set to be 2 µm.

i) Materials

Material properties were imported from the built-in COMSOL library. The substrate used lithium niobate's material properties rotated so that the SAW propagation direction is parallel to the crystalline x-axis and the surface normal is parallel to the 38° rotated crystalline z-axis (rotated clockwise about the crystal x-axis). The corresponding Euler angle is ($\alpha = 0°, \beta = -38°, \gamma = 0°$). The electrodes used Al material properties, ignoring the impact of the Cr adhesion layer. The regions above and below the substrate were set to the properties of air.

ii) Physics

The first physics interface used was the Solid Mechanics interface, employed only on the substrate and electrode domains. This interface solves the solid mechanical equation of motion:

$$\nabla_i \cdot T_{ij} = \rho \frac{\partial^2 u_j}{\partial t^2}$$

where T_{ij} is the surface force acting on each finite element of the mesh (*i.e.*, the stress), ρ is the material density and u_j is the displacement of each finite element from its equilibrium position. Note, the Being an eigenfrequency simulation, the above equation is solved in the frequency domain (let $u_j = u_{j_0} e^{-i\omega t}$):

$$\nabla_i \cdot T_{ij} = -\rho\omega^2 u_j$$

A fixed boundary condition ($u_j = 0$) was imposed on the bottom boundary of the substrate, periodic boundary conditions were imposed on the sides of the substrate, and a free boundary condition ($T_{ij} \cdot n_j = 0$) was imposed on the substrate and electrode surfaces which interface with air.

The second physics interface used was the Electrostatics interface, which was employed on all domains in the computation. The length of the (fabricated 4 µm pitch) IDT is 280 µm, much shorter than the electromagnetic wavelength of ~ 300 mm at a frequency of 1 GHz, so the electric field varies very little over the area of the structure. Thus, the electrostatic approximation in which Maxwell's equations take on their simpler time-independent form can be used:

$$\nabla_i \cdot D_i = \rho_{free}$$

where D_i is the electric displacement field and ρ_{free} is the free charge density. Ground ($V = 0$) was imposed on the top and bottom boundaries of the computational domain, which were stretched to a distance 1 m above and below the substrate using an infinite element domain. The domain for one of the electrodes was also set to ground, whereas a set potential ($V \equiv constant$) was applied to the domain of the other electrode. Periodic boundary conditions were applied to the sides of the computational domain.

Finally, a piezoelectric multiphysics interface was used to couple the solid mechanic and electrostatic interfaces in the substrate's domain. This interface uses the piezoelectric constituent equations:

$$T_{ij} = {c^E}_{ijkl} \cdot S_{kl} - {e^T}_{ijk} \cdot E_k$$

$$D_i = e_{ikl} \cdot S_{kl} + \varepsilon_{ij} \cdot E_j$$

where S_{kl} is the strain, ${c^E}_{ijkl}$ is the elastic stiffness, E_k is the electric field, e_{ikl} is the piezoelectric coupling (${e^T}_{ijk}$ being its transpose), and ε_{ij} is the permittivity.

iii) Meshing

Elements in the simulation were meshed using a free tetrahedral mesh, where the size of mesh elements were constrained to below 0.5 µm ($\lambda_{IDT}/8$). A complete mesh for the simulation can be seen in Figure 8 b).

iv) Results

By using the electrostatic interface, the static capacitance from adjacent finger pairs can be calculated using a stationary solver. The capacitance calculated for the unit cell must be multiplied by the number of finger pairs (70) and scaled to represent the length of fabricated IDT fingers. The calculated capacitance was 8.15 pF, which agrees reasonably with the measured capacitance of 9.27 pF. The difference between the calculated and measured values can be partially attributed to the neglected capacitance from non-finger structures in the IDT, such as contact pads and banks which connect the fingers in an electrode.

The eigenfrequency calculation was used with all physics interfaces to determine the frequency of the calculated SAW modes. SAW modes can be identified by their unique displacement and potential distributions and their strong surface confinement. The SAW mode for a device with a 4 µm pitch was found at 995.5 MHz, having only a 0.10 % difference from the measured SAW operating frequency of 994.5 MHz. A deformed surface map of the displacement amplitude for the calculated SAW mode can be seen in Figure 8 c) and a surface map of the electric potential for the calculated SAW mode can be seen in Figure 8 d).

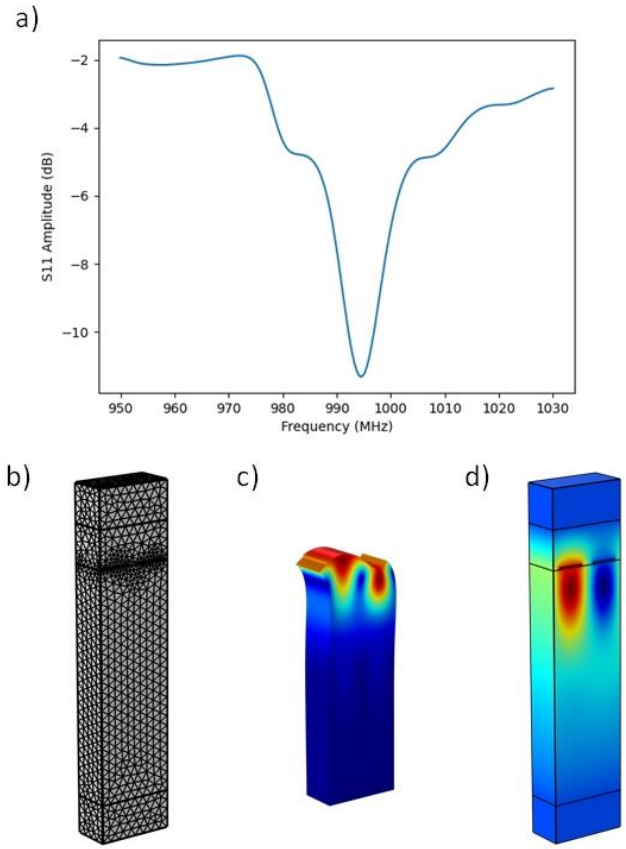

Figure 8: a) Measured S_{11} spectrum of fabrication surface acoustic wave (SAW) device of 4 µm interdigital transducer (IDT) pitch. The S_{11} dip is located at 994.5 MHz. b) Full 3D mesh used in the simulation. c) Deformed surface map of the displacement amplitude for the calculated SAW mode. d) Surface map of the electric potential for the calculated SAW mode.

3.5 Discussion

The modified tri-layer lift-off photolithography process demonstrates an ability to fabricate SAW devices with minimum dimension sizes of 1 µm at high yield, with the main source of device failure being diffraction patterns produced by the mask during exposure. The process is fundamentally diffraction limited, but dimensions of 600 nm at a yield of ~ 30% have been demonstrated on Si using the unmodified tri-layer photolithography process [10]. The main challenge in producing high yield is obtaining good PR-to-mask uniformity over a 4" wafer, which requires an extremely uniform tri-layer thickness. If a smaller wafer is used, the tri-layer's uniformity could be improved leading to smaller realizable dimensions at a higher yield.

4. Conclusion

A tri-layer lift-off photolithography process for the fabrication of high frequency SAW devices on piezoelectric and pyroelectric substrates was described. A previously reported tri-layer photolithography process intended for use on SiO_2 or Si substrates was modified for compatibility with piezoelectric/pyroelectric materials enabling the fabrication of SAW devices. The tri-layer consists of layers of LOR, BARC and PR, where the addition of the BARC layer prevents back reflection of exposure light, improves the structural integrity of the lithographic stack, and decouples the PR and LOR development, improving resolution over traditional lift-off photolithography techniques. The process was employed to fabricate SAW devices with a 4 µm IDT pitch and feature sizes as small as 1 µm on 128° Y-X cut lithium niobate

with high yield. The response of a device was measured, and the frequency of the excited SAW mode was determined as 994.5 MHz. Numerical modelling was carried out to determine the theoretical operating frequency of the SAW device, which is 995.5 MHz. The measured and computed frequencies are in excellent agreement, with only a 0.10 % difference. These results, in addition to physical measurements obtained on fabricated devices, validate the tri-layer photolithography process as capable of reliably fabricating high-quality GHz SAW devices using only standard UV contact photolithography equipment. The process allows for the further development of high frequency SAW applications.

Credit Author Statement

LK developed the modified tri-layer lift-off photolithography process, performed all measurements (excluding SEM and HIM images), and carried out the simulation. HN assisted with process development. SR performed SEM and HIM imaging and aided in process development. XB and PB directed the project. All authors contributed to the interpretation of the results and writing of the manuscript.

Acknowledgements

The authors acknowledge Anthony Olivieri for his guidance in operating numerous tools required for this work, and to Ewa Lisicka-Skrzek for her assistance in designing and preparing the layout used for the photomask.

Declaration of Competing Interest

The authors declare that they have no known competing financial interests or personal relationships that could have appeared to influence the work reported in this paper.

References

[1] D. P. Morgan, Surface acoustic wave filters: with applications to electronic communications and signal processing, Amsterdam: Academic Press, 2007.

[2] D. S. Ballantine, Acoustic wave sensors theory, design, and physico-chemical applications, San Diego: Academic Press, 1997.

[3] M. Hatzakis, B.J. Canavello, J.M. Shaw, "Single-step optical lift-off process," *IBM journal of research and development 24*, pp. 452-460, (1980).

[4] H. Smith, F. Bachner, N. Efremow, "A high-yield photolithographic technique for surface wave devices," *J. Electrochem. Soc. 118*, pp. 821-825, (1971).

[5] H. I. Smith, "Fabrication techniques for surface-acoustic-wave and thin-film optical devices," *Proceedings of the IEEE 62*, pp. 1361-1387, (1974).

[6] J. Mei, N. Zhang, J. Friend, "Fabrication of surface acoustic wave devices on lithium niobate," *J. Vis. Exp. 160*, (2020).

[7] N. Yoshioka, A. Sakai, H. Morimoto, K. Hosono, Y. Watakabe, S. Wadaka, "Fabrication of surface acoustic wave devices By using x-ray lithography," *Journal of Vacuum Science and Technology B 7*, pp. 1688-1691, (1989).

[8] W.H. Brünger, L.-M. Buchmann, M. Kreutzer, M. Torkler, G. Zwicker, B. Fleischmann, "Fabrication of 3.5 GHz surface acoustic wave filters by ion projection lithography," *Microelectronic Engineering 17*, pp. 245-248, (1992).

[9] M. Itoh, H. Gokan, S. Esho, K. Asakawa, "Fabrication process for surface acoustic wave filters having 0.5 μm finger period electrodes," *Journal of Vacuum Science and Technology 20*, pp. 21-25, (1982).

[10] H. Northfield, O. Krupin, R. N. Tait, P. Berini, "Tri-layer contact photolithography process for high-resolution lift-off," *Microelectronic Engineering 241*, p. 111545, (2021).

[11] MicroChem Corp, LOR Lift-off Resists. Technical Brochure, Online, https://amolf.nl/wp-content/uploads/2016/09/datasheets_LOR_datasheet.pdf

[12] Brewer Science, XHRiC I-line Anti Reflective Coating, Technical Brochure [Online], https://wiki.nanotech.ucsb.edu/wiki/images/3/33/XHRiC-Anti-Reflective-Coating.pdf

[13] Rohm and Haas, MEGAPOSIT SPR955-CM Series Photoresist for Microlithography Applications, Technical Brouchure [Online], https://www.mri.psu.edu/sites/default/files/file_attach/Shipley_SPR955_Datasheet.pdf

[14] F.D. Lai, J.M. Hua, "Increasing the maximum operating frequency of SAW filters fabricated using an I-line source," *Microelectronic Engineering 86*, pp. 1300-1302, (2009).

Chapter 3 – Measuring velocity, attenuation, and reflection in surface acoustic wave cavities through acoustic Fabry-Pérot spectra

3.1. Summary

In this chapter we present a method for the measurement of key parameters of the fabricated 2-port SAW resonators. Our method involves the analysis of acoustic Fabry-Pérot resonances and is based on theory from the optics literature. In our experiment, 2-port SAW resonators, consisting of two IDTs laterally separated by a free surface cavity length, are used to generate SAWs on 128° Y-X lithium niobate that are trapped between the two IDTs which also act as Bragg reflectors. Resonant cavity peaks can be observed through the electrical S_{11} (reflection) spectrum measured on one IDT. The free spectral range (FSR) and linewidths of cavity peaks are then measured for 2-port SAW resonators of different cavity lengths. Linear models are then applied to the measured FSR and linewidths to obtain the free surface SAW velocity and SAW propagation attenuation coefficient for SAWs on 128° Y-X lithium niobate, as well as the reflection phase and amplitude of the IDTs. This method of analyzing Fabry-Pérot spectra provides an intuitive method for determining key characteristics of SAW waves in a 2-port SAW resonator.

3.2. Work contribution

In this work, a novel and intuitive method for characterizing SAW cavities is demonstrated through analogy with theory from the optical Fabry-Pérot interferometer. Using our Fabry-Pérot analysis method, the SAW velocity measurement accuracy is 0.2 %. This accuracy is slightly worse than demonstrated using a 3-IDT time delay measurement (~ 0.1 %) [24], yet better than using an optical probing method (~ 0.6 %) [27]. For attenuation, our method demonstrated an accuracy of about 10 %. Accuracy values were absent

in SAW attenuation measurements from the literature. Our method thus provides an intuitive approach for accurately obtaining SAW velocity and attenuation, among other parameters, which can be measured simultaneously and without the use of optical probes.

3.3. Article

The following article is presented as published on IEEE Xplore (available as an early access article. Intended for publication in a future edition of IEEE Transactions on Ultrasonics, Ferroelectrics, and Frequency Control).

Measuring Velocity, Attenuation, and Reflection in Surface Acoustic Wave Cavities Through Acoustic Fabry-Pérot Spectra

Liam Kelly, Pierre Berini, *Fellow, IEEE,* and Xiaoyi Bao, *Senior Member, IEEE*

***Abstract*— Surface acoustic wave (SAW) cavities have been widely applied as electronic bandpass filters, sensors, microfluidic tweezers, and, in recent years, as devices for coupling with quantum systems. Here we propose a novel method of analyzing acoustic Fabry-Pérot spectra, by analogy with optical cavities, to determine the free surface velocity and attenuation of SAW waves, as well as the reflection of interdigital transducers (IDTs), all of which are crucial design parameters. In our experiment, 2-port SAW resonators, consisting of two IDTs laterally separated by a free surface cavity length, are used to generate SAWs on 128° Y-X lithium niobate that are trapped between the two IDTs which also act as Bragg reflectors. Resonant cavity peaks can be observed through the electrical S_{11} (reflection) spectrum measured on one IDT. The free spectral range and linewidths of cavity peaks are then measured to obtain the free surface SAW velocity, SAW propagation attenuation coefficient, and IDT reflection phase and amplitude. Our method of analyzing Fabry-Pérot spectra provides a method for determining key characteristics of SAW waves and cavities.**

***Index Terms*— Surface acoustic waves, interdigital transducer, velocity, attenuation, reflection**

I. Introduction

Since their conception in the 1960's, surface acoustic wave (SAW) devices have gained immense popularity, today billions of SAW devices are manufactured every year [1]. SAW devices almost always include one or two interdigital transducers (IDTs) on a piezoelectric substrate used to excite or detect SAWs. Fabricated from thin metal films, IDTs consist of two electrodes with interdigitated fingers. The period between fingers from the same electrode is known as the IDT pitch (λ_{IDT}) and defines the length of a unit cell which periodically repeats itself over the length of the IDT. By applying an AC signal across the IDT electrodes, an electric potential distribution is generated in the piezoelectric substrate which excites SAW modes. When the frequency of the applied signal matches the frequency of the SAW mode of wavelength λ_{IDT} ($f_0 = v_{IDT}/\lambda_{IDT}$), SAW excitation is maximised. This frequency is known as the fundamental operating frequency of the SAW device. SAW devices exhibit resonant behaviour about f_0 which can be referred to as IDT resonance. When IDTs are measured using a vector network analyzer (VNA), IDT resonance can be observed as a dip in the frequency response of the electrical S_{11} (reflection) parameter, as electrical power is used to drive SAWs near the resonance frequency of the IDT.

SAW cavities, in which SAWs are trapped between two reflecting elements, have been widely applied as electronic bandpass filters [2], microfluidic tweezers [3], and chemical vapour sensors [4]. More recently, SAW cavities have been used for their ability to couple to quantum systems such as super conducting qubits [5], [6], [7] and quantum dots [8]. In designing SAW cavities, parameters such as the free surface SAW velocity, SAW attenuation, and IDT reflection are critical. SAW velocity is often experimentally determined by measuring the fundamental operating frequency of the device then multiplying by λ_{IDT} ($v_{IDT} = f_0 \cdot \lambda_{IDT}$) [9], [10]. However, the obtained velocity is for SAWs overlapping with the IDT, which differs from the free surface SAW velocity because of piezoelectric stiffening and mass loading introduced by the IDT [11]. Alternatively, a SAW pulse can be transmitted between two IDTs and its delay time can be used to calculate the free surface SAW velocity [9], [12]. However, IDTs are spatially distributed along the SAW propagation axis, so the propagation distance is not well defined. Also, the impact on SAW velocity of the IDT regions introduces further error. Means of accurately measuring free surface SAW velocity have been proposed as specialized IDT configurations [13] or by implementing a direct electrical coupling path between 2-port SAW delay lines with different delay line lengths [14], but such specialized designs have no further use. It is also possible to obtain accurate measurements of the free surface SAW velocity by using an optical probe, where the velocity can be measured accurately from the angle of acousto-optically diffracted light [15] or from an optical "sing-around" method [16].

Additionally, SAW attenuation has been measured primarily using optical probes, most notably by measuring the power of acousto-optically diffracted light [15], [17], [18] or detecting surface displacements using a Michelson interferometer [19] at different SAW propagation distances. However, the requirement of an optical setup in addition to the electrical setup needed for SAW excitation makes these methods impractical or inaccessible in many lab environments.

Accurate measurement of the reflection coefficient frequency response of metallized strips on the substrate surface has been demonstrated through time gated S-parameter measurements [20]. The measurement of SAW velocity, attenuation, and reflection has been demonstrated using a 2-port SAW resonator, where SAW parameters were varied until agreement was reached between calculated and measured

LK fabricated the SAW devices and carried out the electrical S_{11} measurements. XB and PB directed the project. All authors contributed to the interpretation of the results and writing of the manuscript. (*Corresponding author: L. Kelly)*

The authors are with the Department of Physics, University of Ottawa, Ottawa, ON K1N 6N5, Canada.

transfer functions [21]. While this method allows for synchronous measurement of various SAW parameters, it requires an unintuitive and complex calculation procedure.

Here we present a novel method based on analysing acoustic Fabry-Pérot spectra, following the theory of optical Fabry-Pérot resonators, to simultaneously measure the free surface SAW velocity, SAW attenuation, and reflection characteristics of IDTs. Multiple SAW cavities of different cavity lengths are used to measure the free spectral range (FSR) and linewidth of cavity peaks as a function of cavity length. Linear regression models can then be employed to obtain key parameters. The proposed method does not require the fabrication of specialized IDT designs or use of optical probes, providing a convenient and intuitive method for measuring key cavity parameters.

II. Theory

When a SAW cavity consists of 2 reflectors separated by a propagation region, the SAW cavity can be regarded as an acoustic analog to an optical Fabry-Pérot interferometer [22]. Resonance is achieved in a SAW cavity when the phase associated with one round trip in the cavity (φ_{RT}) is equal to an integer multiple of 2π, Here, SAWs from successive reflections in the cavity are in phase, producing a maximum SAW intensity in the cavity.

$$\varphi_{RT} = q \cdot 2\pi$$

A derivation of the resonance condition for an acoustic cavity is provided in the appendix. The round-trip phase can be expressed as the sum of the phase accumulated by the SAW as it travels along the free surface between identical reflectors and the phase change associated with both reflectors:

$$\frac{4\pi f l_c}{v_{free}} + 2 \cdot \varphi_{ref} = q \cdot 2\pi$$

Here φ_{ref} is the reflection phase of either reflector (assumed to be identical). It is assumed that all waves are travelling along a direction perpendicular to the cavity reflectors. It is convenient to model φ_{ref} by an effective length, l_0, added to the free surface cavity length:

$$\frac{4\pi f (l_c + 2l_0)}{v_{free}} = q \cdot 2\pi$$

Thus, discrete frequencies resonate in the cavity spaced by frequency intervals known as the free spectral range (Δf):

$$\Delta f = \frac{v_{free}}{2(l_c + 2l_0)}$$

When observed over a sufficiently small frequency range, l_0 will vary minutely and can be assumed constant. Thus, when Δf is measured for 2-port SAW resonators with identical IDTs separated by varying cavity lengths, the inverse of Δf can be plotted against l_{cavity}. By performing a linear regression, v_{free} can be obtained from the slope, while l_0 can be obtained from the y-intercept. l_0 can also then be re-converted to φ_{ref} by using $\varphi_{ref} = 4\pi f_{cen} l_0 / v_{free}$ where f_{cen} is the center frequency used in the analysis.

Furthermore, additional information about cavity losses can be extracted from the linewidth of the cavity peaks. Principal loss mechanisms in an unguided SAW cavity can be divided into two groups: (*i*) Escape losses due to imperfect reflection at the reflectors, and (*ii*) attenuation, scattering, and beam divergence that occurs as SAWs propagate in the cavity. The linewidth (*i.e.*, the full width half maximum) of cavity peaks, Δv_c, can be related to the loss mechanisms as (see appendix for derivation):

$$\Delta v_c = \frac{-\ln\left(R_{ref}^2\right) v_{free}}{4\pi(l_c + 2l_0)} + \frac{v_{free} \cdot \alpha_{loss}}{2\pi}$$

where R_{ref} is the reflectance of each mirror, assumed identical and constant over a sufficiently small frequency range. Note that the intensity attenuation coefficient, α_{loss}, includes contributions from elastic propagation losses, surface scattering losses, and losses due to beam spreading, in units of (1/m). v_{free} and l_0 have been previously acquired through the free spectral range analysis. Thus, by plotting Δv_c *vs.* $\left(l_{cavity} + 2l_0\right)^{-1}$, a linear model can be used to obtain R_{ref} from the slope and α_{loss} from the y-intercept.

III. Experiment and Results

In our experiment, 2-port SAW resonators [23] consisting of two IDTs separated laterally by a free surface cavity length (l_{cavity}) were used to excite and confine SAWs. In this configuration, transmission (S_{21}) and reflection (S_{11}) measurements are possible. In a standard IDT design, IDT fingers are placed on the piezoelectric surface at intervals of $\lambda_{IDT}/2$. Since IDT fingers cause acoustic reflection due to mass loading and piezoelectric stiffening, IDTs will operate not only as transducers but as SAW Bragg reflectors with a reflectance band centered around f_0.

It should be noted that reflections from the IDTs are not localized and that the reflected SAW contains the superposition of many SAWs which have been partially reflected by successive IDT fingers. Depending on the thickness of IDT fingers, SAWs may be reflected multiple times before exiting the IDT. Furthermore, since one IDT is electrically loaded, SAWs passing through the IDT produce a current which may lead to regeneration of SAWs. Nonetheless, the reflection coefficient of both IDTs is taken as $R_{ref}^{0.5} \angle \varphi_{ref}$ where the phase is modelled by an equivalent effective length. Thus, owing to their Bragg behaviour, 2-port SAW resonators trap SAW power between two IDTs to form an acoustic cavity which can be modelled by the aforementioned theory for acoustic cavities.

2-port SAW resonators were fabricated using a tri-layer lift-off photolithography technique [24] on 500 μm thick 128° Y-X cut lithium niobate wafers (Ra < 0.5 nm), as seen in Fig. ***1***. Our designs contained 2 different IDT types, designed to excite SAWs in the Rayleigh mode, which are defined primarily by their values of λ_{IDT} of 16 and 8 μm. The geometric parameters for each IDT type can be seen in Table I. On a fabricated wafer, devices with cavity lengths of 1, 2, 5, 10 and 20 mm were fabricated for each IDT type, and for each cavity length three duplicates were made. Two wafers were fabricated and thus 30 devices per IDT type were produced.

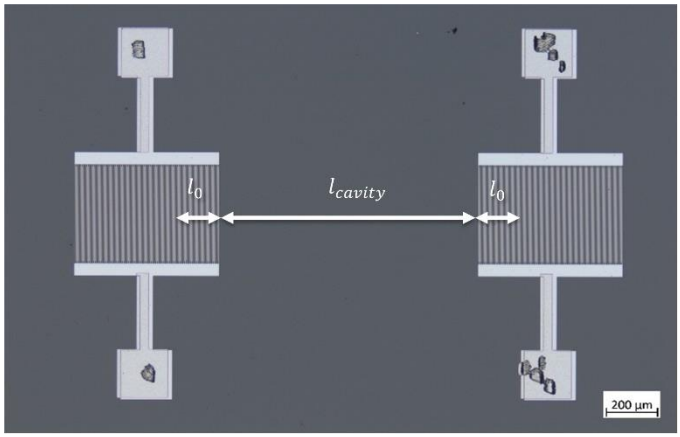

Fig. 1. Optical microscope image (5× lens) of 2 interdigital transducers (IDTs) in a 2-port SAW resonator. Both IDTs have a pitch of 8 µm and are separated by a 1 mm cavity length (l_{cavity}). The correction to the free surface cavity length due to the reflection phase of IDTs (l_0) is shown (not to scale).

TABLE I
DESIGN PARAMETERS OF IDTS USED IN THE 2-PORT SAW RESONATORS.

IDT Pitch (λ_{IDT})	f_0 (MHz)	No. of IDT fingers	IDT aperture (µm)	Metallization ratio (%)	Electrode thickness (nm)
16 µm	248.8	70	750	50	20 (Cr) + 100 (Al)
8 µm	497.5	70	400	50	20 (Cr) + 100 (Al)

When probing one of the IDTs in the cavity, the measured (complex) S_{11} can be viewed as the superposition of two contributions: one due to the IDT and the other due to the acoustic behaviour of the SAW cavity. By measuring the S_{11} responses of an isolated identical IDT (S_{11}^{iso}), and of a 2-port SAW resonator (S_{11}^{res}) constructed from a pair of identical IDTs, the contribution of the cavity can be isolated:

$$S_{11}{}^{cav} = S_{11}{}^{res} - S_{11}{}^{iso}$$

Thus $S_{11}{}^{cav}$ directly represents the contribution from the acoustic behaviour of the cavity and follows the acoustic cavity theory as developed in Section II. It is common practice to model IDTs electrically as an input admittance Y_{11} because the real part of the admittance, $\mathrm{Re}\{Y_{11}\}$, can be directly associated with SAW generation (*i.e.*, the acoustic conductance). In the case of a SAW cavity, this association no longer holds directly as SAW generation is superimposed with the acoustic cavity reflection.

The impact of the SAW cavity on the S_{11} spectrum can be seen in Fig. ***2***, where the response of an isolated IDT is compared to the response of a 2-port SAW resonator. Note, an IDT in a 2-port SAW resonator can be isolated by applying an attenuating material (*e.g.*, epoxy resin, silicone adhesive) on the substrate surface on either side of the IDT, preventing coherent back reflection of SAWs to the IDT.

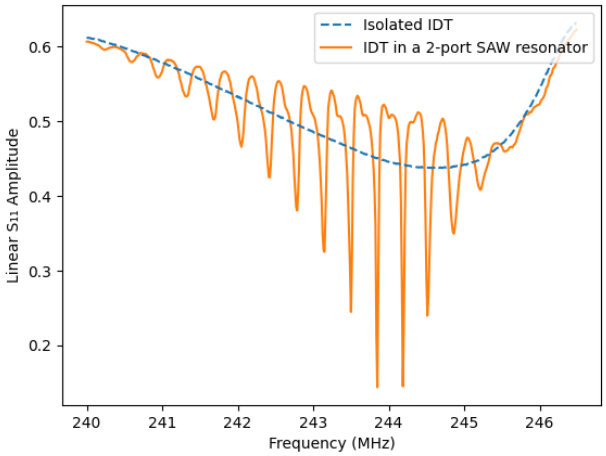

Fig. 2. $|S_{11}|$ spectra of an isolated interdigital transducer (IDT) with $\lambda_{IDT} = 16\ \mu m$ (with suppression of outgoing SAWs using attenuating epoxy), and of an IDT with $\lambda_{IDT} = 16\ \mu m$ in a 2-port SAW resonator with a 5 mm cavity length.

S_{11} (reflection) measurements were obtained on the SAW resonators using an HP 8510 Vector Network Analyzer (VNA). A ground-signal probe (Picoprobe, ECP18) was connected to the VNA via an SMA cable, then the signal and ground tips of the probe were firmly contacted to the IDT's contact pads. The frequency range used for analysis was chosen to capture the resonator's cavity response (243.2-245.2 MHz, 484-486 MHz). S_{11} measurements for IDTs of $\lambda_{IDT} = 8\ \mu m$ and different cavity lengths can be seen in Fig. ***3***.

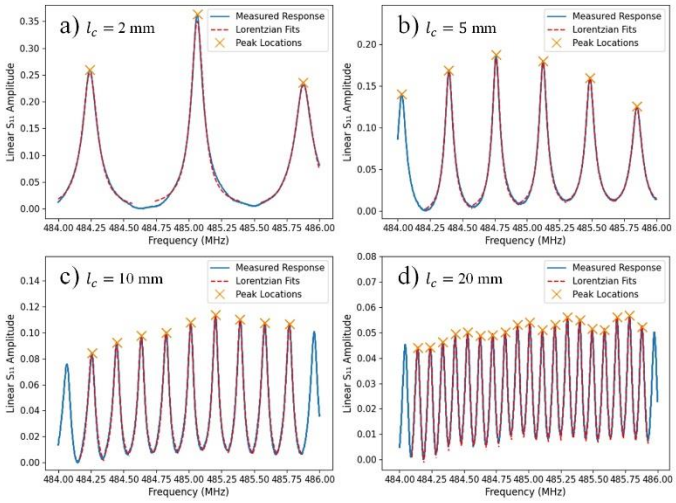

Fig. 3. Cavity peaks with Lorentzian fits and peak locations in the S_{11} spectra of 2-port SAW resonators with IDTs of $\lambda_{IDT} = 8\ \mu m$ and various cavity lengths: (a) $l_{cavity} = 2\ mm$, b) $l_{cavity} = 5\ mm$, c) $l_{cavity} = 10\ mm$, d) $l_{cavity} = 20\ mm$.

For each cavity length, a peak finding algorithm was used to locate the frequency position of peaks in the S_{11} spectra and the frequency difference between successive peaks was determined. The inverse of the measured free spectral range *vs.* the cavity length and its linear regression are plotted for both IDT types in Fig. ***4***. The calculated standard error on the slope and y-intercept, as well as the square of the correlation coefficient (R^2) between the linear fit and measured data

account for the spread in the measured FSR at each cavity length.

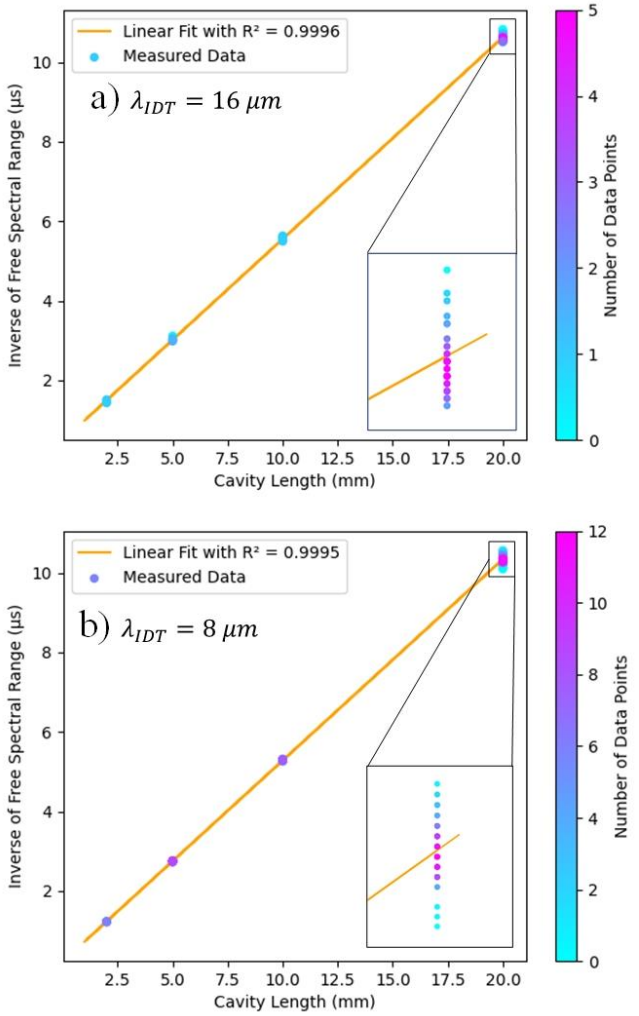

Fig. 4. Inverse of the free spectral range vs. the cavity length. a) Cavities with IDTs of $\lambda_{IDT} = 16\ \mu m$, and b) $\lambda_{IDT} = 8\ \mu m$. Linear regression is performed on both data sets, each fit having an R^2 value > 0.999. Inset magnifies the data for 20 mm cavity lengths, where the spread in data along the y-axis can be observed.

From the linear regression, both IDT types show excellent linearity with an R^2 value > 0.999, validating the assumption that variations of the correction to the free surface cavity length can be assumed constant over the chosen frequency ranges. However, it may be interpreted that the spread in data along the y-axis and the relatively large uncertainties in the correction to the free surface cavity length and reflection phase are due to their frequency dependence. The measured free surface velocities (v_{free}) are $3941 \pm 13\ m/s$ for devices with IDTs of $\lambda_{IDT} = 16$ µm, and $3950 \pm 8\ m/s$ for devices with IDTs of $\lambda_{IDT} = 8$ µm, which are in good agreement with previously reported SAW velocities on 128° Y-X cut lithium niobate of $3955\ m/s$ [9] and $3977\ m/s$ [12]. The measured values of the correction to the free surface cavity length (l_0) and the reflection phase of the IDTs (φ_{IDT}) can be seen in Table II.

The linewidths of the spectral peaks were then determined by fitting a Lorentzian function to each peak in the S_{11} spectra as shown in Fig. ***3***. The Lorentzian function is given as:

$$\mathcal{L}(x) = \frac{A}{1 + (2(x - x_0)/w)^2}$$

where A is the amplitude, w is the linewidth (*i.e.*, the full width at half maximum), and x_0 is the position of the maximum. Theoretically, the cavity peaks should have a Lorentzian line shape (as shown in the appendix), otherwise either a measurement error occurred or a defect in the measured SAW device was present, and thus the peak should be omitted from the analysis. The measurement reliability can be ensured by requiring that the square of the correlation coefficient (R^2) between the raw data and the fitted Lorentzian be above 0.995. Furthermore, IDT fingers are weakly reflecting structures, so the reflection amplitude of IDTs can have considerable frequency dependence. Thus, the measured frequency range can be divided into smaller subsets over which linear analysis is performed to obtain the frequency dependence of the IDT reflection amplitude and SAW attenuation. In our linewidth analysis, frequency subsets with ranges of 336 kHz were used for devices with IDTs having $\lambda_{IDT} = 16$ µm, and 364 kHz for devices with IDTs having $\lambda_{IDT} = 8$ µm.

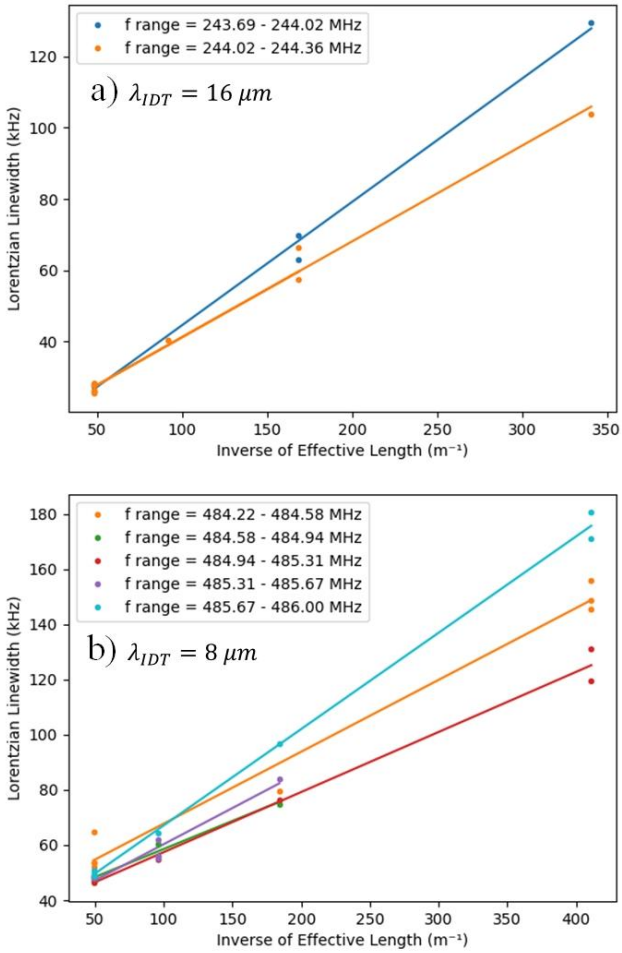

Fig. 5. Lorentzian linewidth of cavity peaks vs. the inverse of the effective free surface cavity length between IDT devices

$(l_{cavity} + 2l_0)^{-1}$ for different frequency subsets. a) IDTs with $\lambda_{IDT} = 16\ \mu m$ and b) IDTs with $\lambda_{IDT} = 8\ \mu m$.

A linear analysis was performed on each frequency subset (Fig. ***5***), all subsets demonstrating good linearity, each producing an R^2 value > 0.95. The measured values of the intensity attenuation coefficient in dB/m (α_{loss}) and the total reflectance of the IDTs acting as a Bragg reflector (R_{ref}) for each frequency subset can be seen in Table III. Values for the SAW attenuation are constant among different frequency subsets for either IDT type, all values being equal within uncertainty, while the reflection amplitudes are not. Although attenuation measurements for SAWs on 128° Y-X lithium niobate could not be found in the literature, the measured attenuation of the 8 μm devices (average α_{loss} of 17.6 dB/m), which operate at a frequency of ~ 485 MHz, can be compared to the measurement of attenuation for an X-propagating shear acoustic wave in lithium niobate in [18] of ~ 18 dB/m @ 500 MHz to excellent agreement. Alternatively, the measured attenuation can be compared with the values measured on Y-Z lithium niobate in [15] of ~ 30.4 dB/m @ 200 MHz and 151.9 dB/m @ 500 MHz. While the measured attenuations are much lower in our experiment, this is expected as the 128° Y-X cut is known to have much lower losses than the Y-Z cut for lithium niobate.

TABLE II
CALCULATED PARAMETERS OF THE SAWS AND CAVITY THROUGH MEASUREMENTS OF THE FREE SPECTRAL RANGE (FSR).

IDT Pitch (λ_{IDT})	**v_{free} (m/s)**	**l_0 (mm)**	**φ_{IDT} (rad)**
16 μm	3941 ± 13	0.47 ± 0.03	367 +/- 23
8 μm	3950 ± 8	0.22 ± 0.02	333 +/- 28

TABLE III
CALCULATED PARAMETERS OF THE SAWS AND CAVITY THROUGH MEASUREMENTS OF THE LINEWIDTHS OF CAVITY PEAKS.

λ_{IDT}	**f Range (MHz)**	**R^2**	**α_{loss} (dB/m)**	**R_{ref}**
16 μm	243.69 – 244.02	0.995	12.0 ± 3.3	0.576 ± 0.013
	244.02 - 244.36	0.989	13.6 ± 1.2	0.651 ± 0.010
8 μm	484.22 - 484.58	0.982	18.2 ± 1.7	0.660 ± 0.015
	484.58 - 484.94	0.984	17.8 ± 0.6	0.725 ± 0.015
	484.95 - 485.30	0.990	17.5 ± 1.1	0.707 ± 0.011
	485.31 - 485.67	0.954	17.3 ± 1.5	0.659 ± 0.030
	485.67 - 486.03	0.998	17.1 ± 1.0	0.574 ± 0.007

IV. DISCUSSION

It should be noted that the results from the spectral linewidths of cavity peaks are inherently less accurate than those from the free spectral range. In the spectral linewidth measurements, it is extremely important that the IDTs be identical, as shorts, broken fingers, pitch variations, and metallization variations have a significant impact on the shape of the underlying IDT resonance. Since the S_{11} spectrum contains contributions from both the IDT and cavity resonances, the shape of the cavity peaks, and consequently their linewidth, are affected by the shape of the IDT peak. Conversely, in the FSR measurement, the position of cavity peaks is determined by the accumulated round-trip phase, which is much less sensitive to IDT defects/variations.

Additionally, in the theory of cavity resonance we assumed that all waves are travelling perpendicular to the cavity reflectors. However, since SAW cavities are unguided, SAWs will diverge from the propagation axis as they propagate between the IDTs. This introduces error in the effective cavity length as the round-trip distance is larger at off-axis angles. Assuming divergence is small, the free spectral range of the cavity peaks will remain unaffected as SAW intensity will be concentrated about the propagation axis. However, it is expected that the linewidth of cavity peaks will be broadened as SAWs at off-resonant frequencies can better satisfy the resonance phase condition at angles which diverge from the propagation axis. As cavity lengths increase, phonon decay time increases, and a larger proportion of SAW intensity travels off-axis. Thus, it is expected that beam divergence will negatively impact the linearity of the linewidth analysis.

It was observed that the reflectance of the IDTs varied between different frequency ranges while the attenuation did not. IDTs consist of many IDT fingers which are weakly reflecting elements, so the reflection amplitude is expected to vary rapidly with frequency. Log scale SAW attenuation has a frequency dependence of $f^{1.6}$ on Y-Z cut lithium niobate [25], so variations in frequency of ~100 ppm are not expected to produce significant changes in the attenuation.

It is also worth noting that our method of spectral analysis can be effective in any SAW device containing a cavity formed by at least 1 IDT. The 2nd IDT in the 2-port SAW resonator can be replaced with an array of reflecting strips or any other method of producing coherent SAW reflection.

V. CONCLUSION

In conclusion, a novel method for determining key parameters in SAW cavities based on analysing the spectral response of acoustic Fabry-Pérot resonators was proposed and demonstrated. 2-port SAW resonators with IDT pitches of 16 and 8 μm, and varying cavity lengths, were fabricated on 128° Y-X lithium niobate and used to generate SAWs which reflect between two IDTs acting as Bragg reflectors and forming an acoustic cavity. The frequency spacing of cavity peaks in the

S_{11} spectra is used to calculate the free surface SAW velocity, the correction to the free surface cavity length, and the reflection phase of the IDTs. The linewidth of the spectral peaks is then used to calculate the intensity attenuation coefficient and the reflection amplitude of the IDTs. The method proposed is easy to implement, providing an accessible method for determining key cavity characteristics.

VI. Appendix – Derivation of Phase Condition for Cavity Resonance and Linewidths of Cavity Peaks

The following derivation of the linewidth of acoustic cavity peaks is adapted by analogy with the optical theory of Fabry-Pérot cavities [24].

Consider a travelling displacement wave, $u_0(x,t)$, which propagates in the x-direction:

$$u_0(x,t) = U_0 \exp\left(i(2\pi f t - kx)\right)$$

where U_0 is the initial displacement amplitude of the wave, f is its frequency, and k is the wavenumber, $k = 2\pi f/v - i\alpha_{loss}/2$, where v is the velocity and α_{loss} is the intensity attenuation coefficient in (1/m). When acoustic waves propagate within a cavity consisting of two mirrors perpendicular to the waves' propagation direction, they are reflected by the cavity mirrors and return to their initial position. Thus, acoustic waves are superimposed with waves from subsequent round-trip reflections, and the total wave can be written as:

$$u_{tot}(x,t) = \sum_n u_0(x,t)|r_1 r_2|^n \exp\left(-in(\varphi_{RT} - i\alpha_{loss} l_c)\right)$$

where n is the number of round trips, r_1 and r_1 are the reflection of cavity mirrors 1 and 2, respectively, φ_{RT} is the accumulated phase per cavity round trip, and l_c is the distance between the two mirrors. Let the complex factor h be defined as:

$$h = |r| \exp\left(-i\varphi_{RT}\right)$$

where $|r| = |r_1 r_1| \exp(-\alpha_{loss} l_c)$, $|r|^2$ being the round-trip intensity attenuation factor. The total displacement wave can then be written as:

$$u_{tot}(x,t) = \sum_n h^n u_0(x,t) = u_0(x,t)/(1-h)$$

The intensity of a displacement wave is proportional to the square of the displacement (dropping (x,t) from notation):

$$\frac{I}{I_0} = \frac{|u_{tot}|^2}{|u_0|^2} = \frac{1}{|1 - |r| \exp(-i\varphi_{RT})|^2}$$

$$I = \frac{I_0}{|1 - |r| \exp(-i\varphi_{RT})|^2}$$

Note that maximum intensity occurs when $\varphi_{RT} = q2\pi$, where q is an integer:

$$I_{max} = \frac{I_0}{(1-|r|)^2}$$

Thus, cavity peaks occur under the condition that $\varphi_{RT} = q2\pi$, known as the resonance phase condition. The intensity can then be written as:

$$I = \frac{I_{max}}{1 + (2\mathcal{F}/\pi)^2 \sin^2(\varphi_{RT}/2)}$$

where $\mathcal{F}$ is the finesse and is given by:

$$\mathcal{F} = \frac{\pi\sqrt{|r|}}{1-|r|}$$

I is then a periodic function of φ_{RT} with a periodicity of 2π. Consider values of φ_{RT} near the $\varphi_{RT} = 0$ peak where $sin(\varphi_{RT}/2) \approx \varphi_{RT}/2$ (because $|\varphi_{RT}| \ll 1$), such that we can write the intensity as:

$$I = \frac{I_{max}}{1 + (\mathcal{F}/\pi)^2 \varphi_{RT}^2}$$

Consider a Lorentzian line shape which is given as:

$$\mathcal{L} = \frac{A}{1 + (2(x - x_0)/w)^2}$$

where A is the amplitude, w is the linewidth (*i.e.*, the full width at half maximum), and x_0 is the position of the maximum. It can be seen that the linewidth of cavity peaks is:

$$\Delta\varphi_{RT} = \frac{2\pi}{\mathcal{F}}$$

where $\varphi_{RT} = \frac{4\pi f l_c}{v_{SAW}} + \varphi_1 + \varphi_2$ and φ_1 and φ_2 are the reflection phases of cavity mirrors 1 and 2, respectively. $\varphi_1 + \varphi_2$ can be modelled as an effective length, l_0, added to the free surface cavity length:

$$\varphi_{RT} = \frac{4\pi f(l_c + l_0)}{v} = \frac{4\pi f l_t}{v}$$

where l_t is the total effective free surface cavity length. Thus, the linewidth of cavity peaks in the frequency domain, Δv_c, is:

$$\Delta v_c = \frac{v_{SAW}}{2\mathcal{F} l_t}$$

Note, the round-trip attenuation factor $|r|^2$ can be expressed as:

$$|r|^2 = R_1 R_2 \exp(-2\alpha_{loss} l_t)$$

R_1 and R_2 being the reflectance of cavity mirrors 1 and 2, respectively. Note that for distributed mirrors such as Bragg reflectors, $\exp(-2\alpha_{loss} l_t)$ effectively models acoustic wave propagation attenuation in the cavity as well as propagation attenuation that occurs as the waves penetrate the reflectors. $|r|^2$ can be equivalently written as:

$$|r|^2 = \exp(-2\alpha_{tot} l_t)$$

where $\alpha_{tot} = \alpha_{loss} + \frac{1}{2l_c} \ln\left(\frac{1}{R_1 R_2}\right)$. Therefore, the finesse $\mathcal{F}$ can be expressed in terms of α_{tot} as:

$$\mathcal{F} = \frac{\pi \exp(-\alpha_{tot} l_t/2)}{1 - \exp(-\alpha_{tot} l_t)}$$

If $\alpha_{tot} l_c << 1$, then $\exp(-\alpha_{tot} l_c) \approx 1 - \alpha_{tot} l_c$. $\mathcal{F}$ can then be written as:

$$\mathcal{F} \approx \frac{\pi}{\alpha_{tot} l_t}$$

The linewidth of cavity peaks can be written as:

$$\Delta v_c = \frac{v_{SAW} \alpha_{tot}}{2\pi}$$

Therefore, the linewidth of cavity peaks can be expressed in terms of loss mechanisms as:

$$\Delta v_c = -\frac{v_{SAW}}{4\pi l_t} \ln(R_1 R_2) + \frac{v_{SAW} \alpha_{loss}}{2\pi}$$

Acknowledgment

The authors acknowledge Luis Angel Mayoral and Maryamossadat Amiri Naeini for their help in constructing the measurement setup and for their guidance in operating numerous tools required for this work.

Declaration of Conflict of Interest

The authors declare that they have no known competing financial interests or personal relationships that could have appeared to influence the work reported in this paper.

Data Availability Statement

The data that support the findings of this study are available from the corresponding author upon reasonable request.

References

[1] P. Delsing, A. Cleland, M. Schuetz, et al., "The 2019 surface acoustic waves roadmap," *Journal of Physics D: Applied Physics 52,* p. 40, (2019).

[2] D. P. Morgan, Surface acoustic wave filters: with applications to electronic communications and signal processing, Amsterdam: Academic Press, 2007.

[3] J. Shi, D. Ahmed, X. Mao, S. Lin, A. Lawita and T. Huang, "Acoustic tweezers: patterning cells and microparticles using standing surface acoustic waves (SSAW)," *Lab on a Chip 9,* pp. 2890-2895, (2009).

[4] H. Wohltjen, "Mechanism of operation and design considerations for surface acoustic wave device vapour sensors," *Sensors and Actuators 5,* pp. 307-325, (1984).

[5] Y. Chu, P. Kharel, W. Renninger et al., "Quantum acoustics with superconducting qubits," *Science 358,* pp. 199-202, (2017).

[6] K. Satzinger, Y. Zhong, H. Chang, et al., "Quantum control of surface acoustic-wave phonons," *Nature 563,* pp. 661-665, (2018).

[7] B. Moores, L. Sletten, J. Viennot, K. Lehnert, "Cavity quantum acoustic device in the multimode strong coupling regime," *Physical Review Letters 120,* (2018).

[8] M. Schuetz, J. Knorzer, G. Giedke et al., "Acoustic traps and lattices for electrons in semiconductors," *Physical Review X 7,* (2017).

[9] H. Sato, T. Meguro, K. Yamanouchi, K. Shibayama, "Optimum cut for rotated Y-cut LiNbO3 crystals used as the substrate of elastic surface wave filters," *The Journal of the Acoustical Society of Japan 30,* pp. 549-556, (1974).

[10] A. Stefanescu, A. Müller, I. Giangu, A. Dinescu, G. Konstantinidis, "Influence of Au-based metallization on the phase velocity of GaN on Si surface acoustic wave resonators," *IEEE Electronic Device Letters 37,* pp. 321-324, (2016).

[11] C. Campbell, Surface Acoustic Wave Devices and their Signal Processing Applications, Academic Press, Inc., 1989.

[12] J. Temmyo, I. Kotaka, T. Inamura, S. Yoshikawa, "Precise measurement of SAW propagation velocity on LiNbO3," *IEEE Transactions on Sonics and Ultrasonics 27,* pp. 218-219, (1980).

[13] M. Hirabayashi, "A technique for measuring phase velocities of surface acoustic waves using comb filters," *Japanese Journal of Applied Physics 20,* pp. 53-56, (1981).

[14] M. Hirabayashi, "Precise measurement of phase velocity of surface acoustic waves using parallel comb filters," *Electronics letters 25,* pp. 1380-1381, (1989).

[15] G. Cambon, M. Rouzeyre, G. Simon, "Optical probing of surface Rayleigh waves," *Applied Phyiscs Letters 18,* pp. 295-298, (1971).

[16] K. Suzuki, M. Nishikawa, "“Sing-around” method for acoustic surface-wave velocity measurements using an optical probe," *Japanese Journal of Applied Physics 13,* pp. 1216-1218, (1974).

[17] A. Slobodnik, "Microwave frequency acoustic surface wave propagation losses in LiNbO3," *Applied Physics Letters 14,* pp. 94-96, (1969).

[18] I. Bajak, A. McNab, J. Richter, C. Wilkinson, "Attenuation of acoustic waves in lithium niobate," *The Journal of the Acoustical Society of America, ,* pp. 689-695, (1981).

[19] M. Ryzy, T. Grabec, J. Osterreicher, M. Hettich, I. Veres, "Measurement of coherent surface acoustic wave attenuation in polycrystalline aluminum," *AIP Advances 8,* (2018).

[20] P. Wright, "Modeling and experimental measurements of the reflection properties of SAW metallic gratings," *iEE 1984 Ultrasonics Symposium,* pp. 54-63, (1984).

[21] Waldemar Soluch, "Application of Synchronous Two-Port Resonators for Measurement of SAW Parameters in Piezoelectric Crystals," *IEEE Transactions on Ultrasonics, Ferroelectrics and Frequency Control, 45,* pp. 1113-1116, (1998).

[22] Y. Xu, W. Fu, C. Zou, et al., "High quality factor surface Fabry-Perot cavity of acoustic waves," *Applied Physics Letters 112,* (2018).

[23] D. Bell, "Surface-acoustic-wave resonators," *Proceedings of the IEEE 64,* pp. 711-721, (1976).

[24] L. Kelly, H. Northfield, S. Rashid, X. Bao, P. Berini, "Fabrication of high frequency SAW devices using tri-layer lift-off photolithography," *Microelectronic Engineering, 253,* (2022).

[25] E. Lean, C. Powell, "Optical Probing of Surface Acoustic Waves," *Proceedings of the IEEE, 58,* pp. 1939-1947, (1970).

[26] B.E.A Saleh, M. C. Teich, Fundamentals of Photonics 3rd Edition, John Wiley & Sons, Inc., 2019.

Chapter 4 – High resolution surface acoustic wave (SAW) strain sensor based on acoustic Fabry-Pérot resonance

4.1. Summary

In this chapter we demonstrate a high-resolution SAW strain sensor based on measuring Fabry-Pérot resonance peaks from a 2-port SAW resonator. First, a theoretical analysis is proposed to estimate the frequency sensitivity to strain for cavity resonance peaks and to predict strain distributions in both the cavity and IDT regions of a 2-port SAW resonator bonded to a tapered cantilever beam. Then, in order to determine the minimum resolution of the proposed device, its frequency stability and sensitivity are measured. The frequency stability of cavity resonance peaks for 2-port SAW resonators of different cavity length are measured to determine the cavity length which exhibits optimal stability. It is found that the stability of cavity resonances improves with cavity length up to 10 mm. A cross-correlation analysis technique is then introduced to improve the detection of the frequency shift of SAW resonances and enable multimode frequency shift detection. Then, the measured frequency sensitivity to strain of the cavity resonances of a resonator 10 mm in length was measured and found to be -103.2 ± 0.2 Hz/με, its stability over a 60 s interval was found to be 12.1 Hz. By considering a minimum signal to noise ratio (SNR) of 3 dB, the device exhibits a minimum strain resolution of 234 nε. Additional details including the equations used for FEM analysis and the FEM optimization of the cantilever beam geometries are included as supplementary materials. Finally, the frequency stability of cavity resonances of 10 mm long resonators was compared where it was found the lowest operating frequency had the best stability and is therefore optimal for high-resolution strain measurements.

4.2. Work contribution

In this work, a high-resolution SAW strain sensor based on measuring Fabry-Pérot resonance peaks from a 2-port SAW resonator was demonstrated. To achieve high resolution, the ratio of the device's sensitivity to its stability must be high, thus in designing this device several factors which affect the strain sensitivity and stability of SAW devices were investigated. Firstly, a numerical analysis was performed to predict the strain distributions in a SAW device bonded to a cantilever beam. From this analysis, it was determined that the IDT region experiences less strain than the cavity region, due to the former being closer to the device edges and having metallic strips which effectively increase the elastic stiffness when compared to the later, which had not been previously studied in the literature. Additionally, the dependence of frequency shift stability on the device's cavity length was investigated for the first time, finding that a 10 mm cavity exhibited optimal stability. It is found that stability tends to improve with cavity length, which we attribute to *i)* the reduced impact of thermal noise arising from electronic circuitry in the SAW cavity when compared to the IDT regions and *ii)* the requirement of a smaller frequency sweep range to track the cavity peaks (as their Q-factor improves with cavity length), reducing the frequency measurement uncertainty of the VNA. Furthermore, a cross-correlation technique was introduced to SAW devices to improve frequency shift detection and enable multimode sensing. These results provide important insights into the mechanisms which determine the sensitivity and stability of SAW strain sensors and are used to demonstrate a high-resolution strain sensor. The resolution of our sensor (234 nε) is on par with the state-of-the-art technology, which was demonstrated using a temperature-compensated SAW oscillator on 128° Y-X lithium niobate (174 nε [44]).

4.3. Article

The following article is presented as published in Sensors and Actuators A: Physical, 338 (May 2022).

High-resolution surface acoustic wave (SAW) strain sensor based on acoustic Fabry-Pérot resonance

Liam Kelly,[a) 1,2] Chen Chen,[1,2] Xiaoyi Bao,[1,2] Pierre Berini[1,2,3]

[1]Department of Physics, University of Ottawa, Ottawa ON, K1N 6N5, Canada
[2]Centre for Research in Photonics, University of Ottawa, Ottawa ON, K1N 6N5, Canada
[3]School of Electrical Engineering and Computer Science, University of Ottawa, Ottawa ON, K1N 6N5, Canada

Abstract

A surface acoustic wave (SAW) strain sensor based on measuring acoustic Fabry-Pérot resonance peaks from a 2-port SAW resonator is demonstrated. A theoretical analysis is proposed to estimate the frequency sensitivity to strain of IDT and cavity resonances and to predict strain distributions in both the cavity and IDT regions of a 2-port SAW resonator bonded to a tapered cantilever beam. The frequency stability of cavity resonance peaks for fabricated 2-port SAW resonators of different cavity length are measured and analyzed to determine the cavity length which exhibits maximum frequency stability. A cross-correlation analysis technique is then introduced to improve the detection of the frequency shift of SAW resonances and enable multimode frequency shift detection. The measured frequency sensitivity to strain of the cavity resonances of a resonator 10 mm in length (operating frequency = 97.7 MHz) was found to be -103.2 ± 0.2 Hz/με while demonstrating excellent linearity (R^2 = 0.9999). By considering a minimum signal to noise ratio (SNR) of 3 dB, the device exhibits a minimum strain resolution of only 234 nε.

Keywords: SAW, Strain sensor, Stability, High-resolution

1. Introduction

SAW devices as strain sensors have received considerable interest due to their low power consumption, wafer-scale fabrication, sensitivity, robustness, passive implementation, and ability to be remotely interrogated, making them ideal sensors for rugged conditions as required in the aerospace, automotive, and civil engineering fields. Compared to alternatives such as piezoresistive [1], [2] or optical fiber strain sensors [3], [4], SAW sensors have superior dynamic range, low system complexity, and are inexpensive.

Surface acoustic wave devices used as strain sensors are based on several design configurations. The first and simplest form of a SAW strain sensor is the 1-port SAW resonator, where the resonance frequency of the interdigital transducer (IDT) is used as the measurand [5], [6], [7]. When strained, the SAW velocity and pitch of the IDT are affected, leading to shifts in the IDT's resonant frequency. 1-port SAW resonators often feature arrays of reflecting metal strips on either side of the device to enhance the Q-factor of the IDT resonance. Additionally, SAW strain sensors based on 2-port SAW resonators have been demonstrated [8], which consist of two IDTs separated by a free surface length and enable transmission measurements from one IDT to the other. When a standard IDT design is used with many finger pairs, IDTs act not only as transducers but also as SAW Bragg reflectors. Acoustic energy is then trapped between the IDTs which form a cavity, with resonant modes that appear when the round-trip phase is an integer multiple of 2π, analogous to an optical Fabry-Pérot interferometer. The addition of a 2nd IDT gives rise to distinct Fabry-Pérot cavity modes in the S_{11} (reflection) frequency response when compared to a single IDT. These cavity modes are sometimes eliminated in 2-port SAW resonators by implementing a split finger IDT design [9].

Other common designs include the SAW oscillator, which uses two IDTs in a "sing-around" configuration to generate high quality factor resonant modes [10], [11], [12]. SAWs produced by a transmitting IDT are converted to an electrical signal at a receiving IDT, then amplified and routed back to the transmitting IDT, causing the system to oscillate when the total phase per system round trip is an integer multiple of 2π. When the substrate is strained, both the distance between the IDTs and the SAW velocity in the substrate are affected, producing a shift in the oscillation frequencies. Finally, SAW strain sensors have been demonstrated using the reflective delay line, where the change in phase of a SAW signal produced by an IDT, travelling to and from a reflection array under strain, is measured [13], [14]. Reflective delay lines are in principle similar to 2-port SAW resonators, with the exception that for the reflective delay line only reflection measurements can be made and multiple reflections between the IDT and reflection array are not considered.

a) Corresponding author.

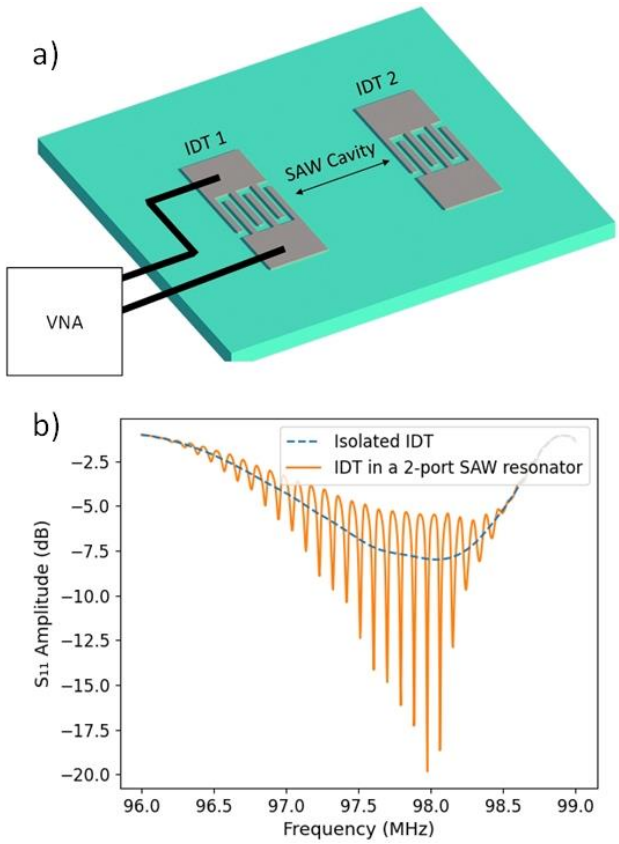

Figure 1: a) Sketch of two IDTs in a 2-port SAW resonator configuration forming a cavity acting as a Fabry-Pérot resonator for SAWs. One IDT is connected to a vector network analyzer (VNA) to excite and detect SAW signals. b) Comparison of the measured S_{11} (reflection) frequency response of an isolated IDT and of a 2-port SAW resonator of 20 mm cavity length between IDTs.

The strain resolution (minimum detectible strain) of any strain sensor is determined by two performance metrics: strain sensitivity and stability of the baseline signal (unstrained). The stain sensitivity can be defined as the partial derivative of the measurand, *e.g.*, the frequency of a particular resonance, with respect to strain. Improvements in strain sensitivity of SAW devices have been primarily achieved by either increasing the operating frequency of the device [15] or choosing a substrate material that exhibits high strain sensitivity [7]. The stability can be defined as the standard deviation of the baseline measurand, *e.g.*, the standard deviation of the frequency of a particular resonance under no (or nominal) strain. SAW devices typically suffer from instability, mainly due to the high temperature coefficient of frequencies (TCF) often associated with SAW substrates [12]. 128° Y-X $LiNbO_3$ is one of the most popular SAW substrates due to its low SAW attenuation and high piezoelectric coupling, but it has a large linear TCF of ~ 75 ppm/°C [16], leading to large SAW frequency fluctuations when temperature is not well controlled. Approaches used to reduce temperature dependence include selecting a piezoelectric substrate with a flat temperature dependence near the operating temperatures [11], subtracting the response of a secondary unstrained reference device [12], or fabricating SAW devices on thin film piezoelectric substrates that can excite the transverse shear mode in addition to SAW modes, allowing for temperature compensation through knowledge of the strain and TCF of both acoustic modes [8], [17]. While these methods are effective at compensating for slowly changing environmental temperatures, thermal noise arising from the electronic circuitry used to interrogate the sensors also contributes and should be considered in the system design.

A high-resolution strain sensor based on acoustic Fabry-Pérot resonance peaks from 2-port SAW resonators is demonstrated. Theoretical modelling is used to investigate and compare strain distributions in both the cavity and IDT regions of a device that is bonded to a tapered cantilever beam used as a strain test structure. Several devices of different cavity length are then fabricated, and the effect of the resonator's cavity length on the frequency stability of SAW resonances is investigated for the first time, allowing for the determination of the optimal cavity length for high-resolution strain measurement. A 2-port SAW resonator with a 10 mm cavity length is then bonded to the surface of a tapered cantilever beam for strain measurements. A cross-correlation analysis technique is introduced to improve the detection of the frequency shift of the cavity resonance and enable multimode frequency shift detection. Finally, the strain sensitivities of both the IDT and cavity resonances for the examined device are measured and compared.

2. Theory and modelling

2.1 Strain sensitivity of interdigital transducer (IDT) and Fabry-Pérot cavity resonances

2-port SAW resonators, which consist of two IDTs separated by a free surface length, as sketched in Figure 1a, are used for strain sensing in this work. The addition of the 2nd IDT gives rise to Fabry-Pérot cavity modes, whose frequency can be used as a strain measurand. Since only one IDT is probed while the 2nd IDT acts only as a Bragg reflector, the employed devices act as 1-port resonators in this work. However, since the devices are identical in design to what is typically used for 2-port SAW resonators, they are referred to as such throughout. Theoretical expressions for the strain sensitivities of both the resonance of an isolated IDT and cavity resonance of the 2-port SAW resonator are derived and compared.

i) IDT resonance sensitivity

IDTs are thin metallic structures which consist of two electrodes with interdigitated fingers that are placed on a piezoelectric substrate to excite and detect SAW modes. The distance between fingers of the same electrode is known as the periodicity of the IDT and is usually set to the wavelength of the SAW to be transduced (λ_{IDT}). When an electrical signal is applied across the electrodes at the frequency of the SAW mode of wavelength λ_{IDT} ($f_{IDT} = v_{SAW}/\lambda_{IDT}$, where v_{SAW} is the SAW velocity), SAW generation is maximal. Thus, resonance occurs about f_{IDT}, known as the IDT resonance. The frequency shift of the IDT resonance with strain can be used as the measurand. Consider an IDT whose period is parallel to the x-direction, with a uniform strain distribution throughout the device substrate that is also directed parallel to the x-direction. The fractional shift in the resonance frequency ($\Delta f_{IDT}/f_{IDT_0}$) can be expressed as:

$$\frac{\Delta f_{IDT}}{f_{IDT_0}} \cong \frac{\Delta v_{SAW}}{v_{SAW_0}} - \frac{\Delta \lambda_{IDT}}{\lambda_{IDT_0}} = \frac{\Delta v_{SAW}}{v_{SAW_0}} - \varepsilon_{xx} \qquad (1)$$

where the subscripts 0 and ε refer to the unstrained and strained states, respectively. Thus, the fractional change in the fundamental operating frequency of the SAW device depends only on the fractional change in velocity and the strain parallel to SAW propagation.

ii) Fabry-Pérot resonance sensitivity

SAW reflecting elements, such as arrays of reflecting strips, gratings, or IDTs with many fingers can be used to create an acoustic cavity. Like an optical Fabry-Pérot interferometer, resonant cavity modes can be observed when the phase per cavity round trip is equal to an integer multiple of 2π, as shown in Figure 1b. The frequency of the cavity modes (f_c) can be expressed as:

$$f_c = \frac{n v_{SAW}}{2l} \qquad (2)$$

where l is the length of the cavity and n is an integer. When a SAW cavity is strained, the length of the cavity and the SAW velocity are affected, thus the fractional change in frequency is

$$\frac{\Delta f}{f_0} = \frac{\Delta v_{SAW}}{v_{SAW\,0}} - \frac{\Delta l_{eff}}{l_{eff\,0}} = \frac{\Delta v_{SAW}}{v_{SAW\,0}} - \varepsilon_{xx} \qquad (3)$$

We then find that the fractional frequency shift for cavity modes is identical to the fractional frequency shift of a single resonant IDT (Eq. (1)), and that it has no dependence on the length of the cavity. However, it should be noted that some error may be introduced by absorbing the reflection phase in the cavity length as the IDTs are not localized reflectors and the reflection is the sum of reflection from successive IDT fingers. It should also be noted that it has been assumed in the analysis that strain is uniformly distributed throughout the substrate and is the same over the IDT and cavity regions.

2.2 FEM modelling of Strain Distributions in SAW Device and Cantilever Beam

Details of the FEM modelling scheme adopted, the governing physics and optimization of the cantilever beam geometry can be found in the supplementary materials.

The straining structure used in the experiments is a tapered cantilever beam, selected for its ability to easily produce a uniform x-directed strain distribution along its top surface. Using a FEM model, the dimensions of the cantilever beam were optimized to minimize the strain difference between the top surfaces of both the cantilever beam and the SAW device, while maintaining a high strainability (see supplementary materials for details). The dimensions of the optimized cantilever beam are: a free length (L) of 50 cm, a fixed end width (w_i) of 70 mm, a free end width (w_f) of 5 mm, and a thickness (h) of 6 mm. The material properties of the cantilever beam used in the simulations were set to those of grade 316 stainless steel using the built-in COMSOL library [18].

An FEM model was then used to determine the strain distributions in a SAW device that was assumed perfectly bonded to the strained cantilever beam. The geometry of the SAW device modelled (width of 5 mm, length of 20 mm and thickness of 500 μm) was specified to match the geometry of the fabricated 2-port SAW resonators of 10 mm cavity length. 120 μm thick Al strips were placed on the SAW device surface with a 50% duty cycle and a period of 200 μm to model the effects of the IDTs on the surface strain. The material properties of the cantilever beam and the SAW device were set to those of grade 316 stainless steel and 128° Y-X $LiNbO_3$, respectively. A stationary solver was used with the solid mechanics interface to determine the strain distribution throughout the SAW device and cantilever beam, assuming perfect adhesion between the two. The calculated strain distributions are given in Figure 2a. The strain in both the cavity and IDT regions of the SAW device, due to a mass applied to the cantilever beam's free end, were calculated, and are plotted in Figure 2b. The average induced strain per applied kg over the cavity and IDT regions were determined from best-fit linear models as 61.88 με/kg and 53.25 με/kg, respectively. The cavity region experiences 16% more strain than the IDT region due to two main effects: *i.* Strain is better coupled from the cantilever surface to the SAW surface in regions that are further from the SAW device edges, as shown in the inset of Figure 2a. *ii.* The Al IDT structures effectively increase the elastic modulus of the substrate surface in the IDT regions, making these areas more difficult to strain than the free surface.

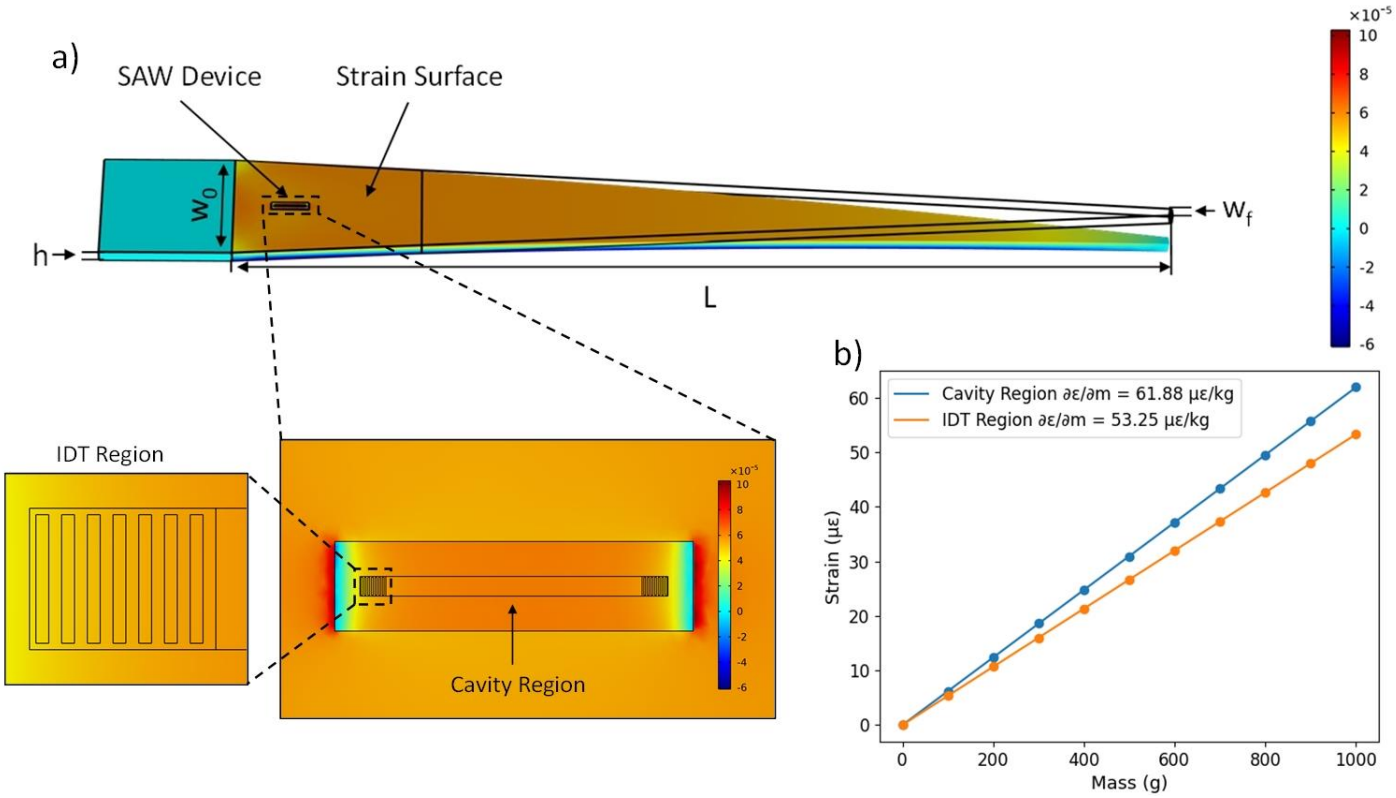

Figure 2: a) Computed deformed surface map of the x-directed strain (ε_{xx}) for a cantilever beam with a SAW device assumed bonded to its surface in response to a 1 kg load applied at the free end. Insets show enlarged surface maps of the x-directed strain (ε_{xx}) over the SAW device and over an IDT region. b) Calculated average x-directed strain (ε_{xx}) in the cavity and IDT regions of the SAW device in response to various masses applied to the cantilever beam's free end. Both data sets demonstrate excellent linearity with R^2 values of 1.0000 for both linear fits.

3. Experiment

3.1 Experimental setup

2-port SAW resonators consisting of two identical IDTs separated by a cavity length were fabricated on 500 μm thick 4" dia. 128° Y-X $LiNbO_3$ wafers. The devices were fabricated using a tri-layer lift-off photolithography technique intended for piezoelectric and pyroelectric substrates as described elsewhere [19]. The design geometries which were used for all fabricated IDTs are given in Table 1. These IDTs were used to create 2-port SAW resonators of 1, 2, 5, 10, and 20 mm cavity length. A second 700 nm thick layer of Al was also patterned on all devices for use as electrical contact pads. A microscope image of a completed device is shown in Figure 3a.

The tapered cantilever beam was fabricated from a ¼" (6.35 mm) sheet of stainless steel, following the optimal dimensions determined by modelling in Subsection 2.2 (the fixed width of the beam is 70 mm, its free width is 5 mm, and its free length is 50 cm). The stainless steel used was grade 316 or grade 304 (the mechanical properties of both grades are effectively identical) [20]. Using these dimensions, the applied mass to cantilever beam surface strain ratio was determined via FEM modelling and found to be 51.93 με/kg. The cantilever beam was mounted on a floating optics table as shown in Figure 3b.

The frequency response of the fabricated SAW devices was measured using an HP 8510 vector network analyzer (VNA). Ground-signal probes (Picoprobe, ECP18) were mounted onto optical positioners and connected to the VNA by SMA cables. The signal and ground tips of the probes were firmly contacted to the pads of the IDTs. By using two identical SAW devices and connecting one IDT from each to VNA ports 1 and 2, the electrical reflection S-parameters (S_{11} and S_{22}) were measured for both devices concurrently (almost simultaneously). Concurrent measurement allows for one device to act as an unstrained reference and the other as the strain sensor, enabling compensation of environmental temperature fluctuations via comparative measurements. The IDT and cavity resonances of each device were observed as dips in their respective reflection spectra.

Table 1: Design geometry of the fabricated IDTs used in the 2-port SAW resonators.

IDT Pitch (μm)	Metallization Ratio (%)	# of Finger Pairs	Aperture Width (μm)	Film Thickness (nm)
40	50	70	1000	20 (Cr) + 100 (Al)

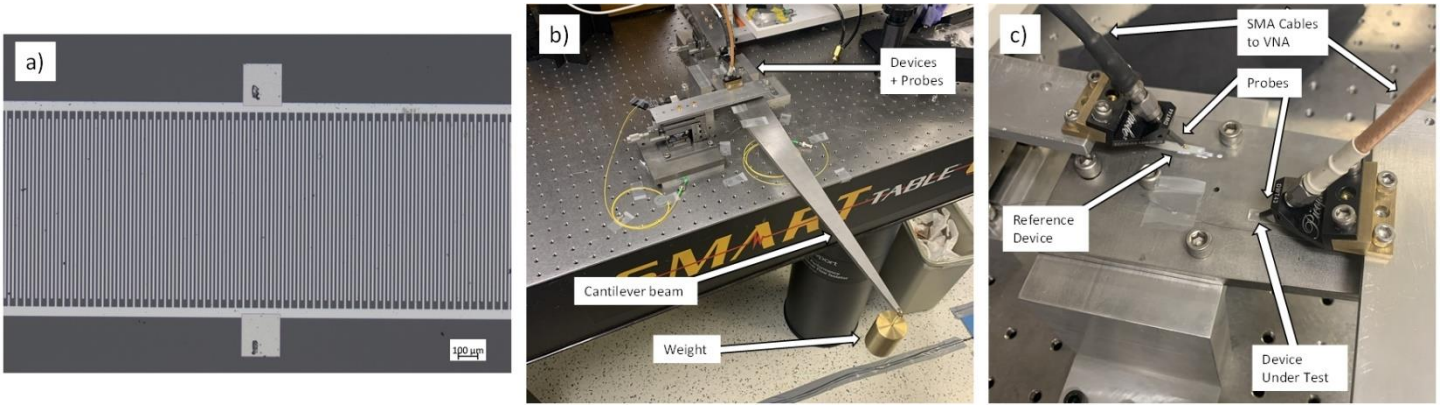

Figure 3: a) Optical microscope image of a fabricated IDT with thick metal contact pads (probing marks are apparent). b) Cantilever beam setup with a mass loaded at the cantilever beam free end to induce strain. c) Probes contacted the reference device (left) and the device under test (right).

3.2 Calibration of mass to strain

An optical fiber Bragg grating (FBG) was used to determine the relationship between a mass applied to the free end of the cantilever beam and the strain produced on the cantilever beam surface. An erbium-doped fiber amplifier (Amonics, C-band) was used as a broadband ASE source. The light reflected from the FBG was isolated using a circulator and captured using an optical spectrum analyzer (Yokogawa AQ6375). The optical FBG was initially calibrated to determine its wavelength shift sensitivity to longitudinal strain as 1.2591 pm/με, in good agreement with the theoretical value of 1.21 pm/με [21]. The optical FBG was then bonded to the cantilever surface, parallel to the length of the cantilever beam, using all-purpose Krazy glue. By applying mass to the free end of the cantilever beam, a longitudinal strain is applied to the FBG sensor introducing a wavelength shift of the reflection band, as shown in Figure 4a, due to changes in refractive index and lengthening of the FBG. As shown in Figure 4b, the wavelength shift varies linearly with applied mass, such that the slope of the best fit linear model is obtained as 67.35 pm/kg. Using the (aforementioned) wavelength shift sensitivity to strain of the FBG, the relation between applied mass and strain on the cantilever beam surface is obtained as 53.45 με/kg, which is in good agreement with the value calculated via COMSOL of 51.93 με/kg (Subsection 3.1).

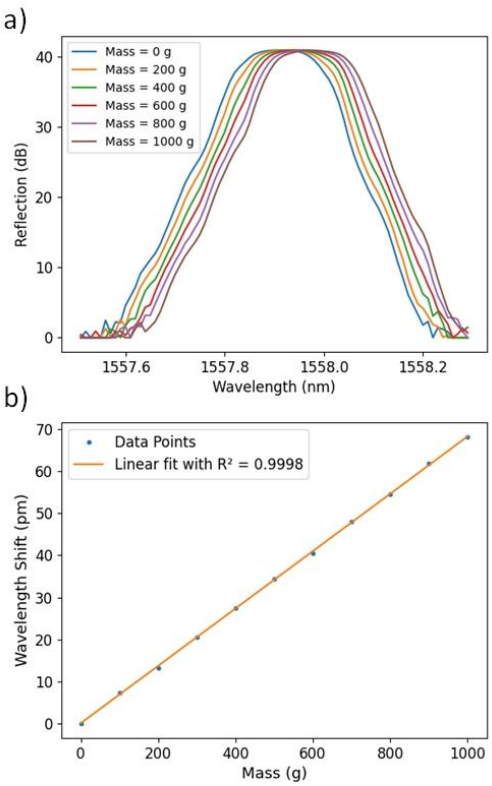

Figure 4: a) Traces of the FBG reflection band when various masses are applied to the free end of the cantilever beam. b) The wavelength shift of the FBG reflection band as a function of mass. A linear fit is applied to the data, having a slope of 0.06735 pm/g and an R^2 value of 0.9997.

3.3 Stability of IDT and cavity peaks (60 min)

The stability of an IDT resonance peak, and of several resonance peaks of 2-port SAW resonators of different cavity length, were then measured over the course of 60 minutes. The S-parameter reflection spectra (S_{11} and S_{22}) of 2 identical devices were measured every 1.4 s and the frequency shift of both devices was recorded. In this configuration, one device acts as the device under test and the other acts as the reference. The temperature compensated frequency shift is obtained by taking the difference between the frequency shift of the two devices, as the resonance frequencies of both devices are equally impacted by environmental temperature fluctuations. Remaining fluctuations in the baseline temperature-compensated frequency shift reflect the noise in the device. The temperature compensated frequency shift and its gradient, the frequency shift rate (calculated using the second order centered difference approximation), of all resonances are shown in Figure 5a, illustrating the improved stability of the cavity resonances over the IDT resonance. The measured frequency shift stability and frequency shift rate stability, taken as the standard deviation of the frequency shift and frequency shift rate over time, respectively, with no strain present, are shown in Figure 5b. Increasing the cavity length tends to improve the stabilities of both the frequency and the frequency shift rate, with optimal frequency shift stability occurring for the 10 mm long cavity, making it the most suitable for high resolution strain measurements. The time responses of Figure 5a represent baseline signals against which changes due to applied strain would be compared, and resolution improves as the standard deviation of the baseline decreases.

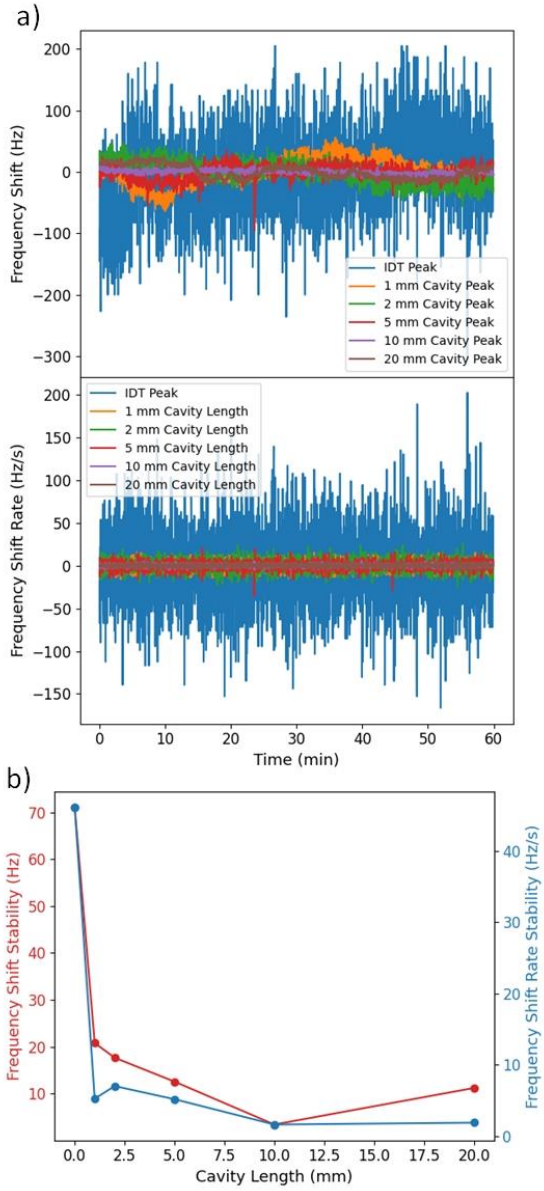

Figure 5: a) Frequency shift of resonant peaks vs. time (top panel) and frequency shift rate vs. time (bottom panel) for an isolated IDT and 2-port SAW resonators of cavity length 1, 2, 5, 10, and 20 mm. b) Frequency shift stability and frequency shift rate stability of resonance peaks of 2-port SAW resonators of different cavity length. The stabilities of the IDT resonance peak are plotted as a cavity length of 0 mm. The stabilities are taken as the standard deviation over time of the traces in Part (a).

3.4 Strain measurements of IDT and 10 mm cavity peaks

Strain measurements were then performed using two 2-port SAW resonators with 10 mm long cavities. One device, the device under test, was fixed to the cantilever beam surface about 2 cm away from the fixed end of the beam using all purpose Krazy glue, while the other device, the reference device, was loosely attached to the top of the fixed area of the cantilever beam using high compliance silicone adhesive as shown in Figure 3c. In this configuration both devices experience nearly identical temperatures, while only the device under test experiences strain, allowing for temperature compensation. As strain is applied to the device under test by applying mass to the free end of the cantilever beam, the frequency response of the S-parameter reflection spectrum of the device under test shifts. The peak shift can be measured by fitting a

mathematical function to the peak, such as a Lorentzian function, but this method is problematic as cavity peaks are impacted by the shape of the underlying IDT resonance and consequently often do not fit well to a particular mathematical function (see Figure 6a)).

The frequency shift of the reflection spectrum is therefore best determined by applying a cross-correlation technique, which determines the "likeness" between the two spectra as a function of the displacement (lag) of one spectrum relative to the other. Consider a S_{11} measurement of a device over a frequency range $[f_0, f_f]$ with a frequency step f_{step}, measured over the time range $[0, t_f]$. For every value of t, the full cross-correlation, $corr$, can be calculated between $S_{11}(t, f)$ and $S_{11}(0, f)$ as:

$$corr(t, lag) = \sum_{f=f_0}^{f_f} {S_{11}}^*(t, f) S_{11}(0, f + lag \times f_{step}) \qquad (4)$$

The full cross-correlations between S_{11} spectra, before and after application of various amounts of strain to the cantilever beam surface, are shown in Figure 6b. The frequency shift of the spectrum at time t is determined by taking the difference in lag between the maximum value of $corr(t, lag)$ and the maximum value of $corr(0, lag)$, then multiplying by f_{step}. This method does not require peaks to adhere to the shape of any mathematical function, and as shown in Table 2, boasts better linearity, stability, and signal to noise ratio (SNR) compared to frequency shift measurements made using a Lorentzian fit. Furthermore, when using a fitting method, multimode devices can present an issue as the fitted function can mode hop from one peak to another. Thus, to avoid mode hopping, limiting the measurement frequency range to a bandwidth narrower than the mode spacing is required so that only one resonant peak is tracked. Since the cross-correlation method detects of the frequency shift of the entire measured spectrum, the existence of multiple modes does not present an issue and no frequency limitations are required.

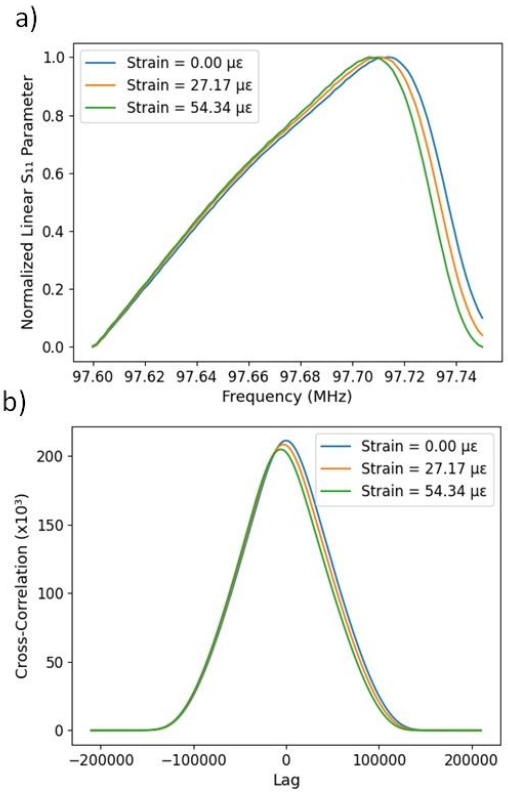

Figure 6: a) Normalized linear S_{11} spectra of cavity peaks of a 10 mm 2-Port SAW resonator with various amounts of strain induced on the cantilever beam's surface. b) The full cross-correlation between strained and unstrained traces for various amounts of strain induced on the cantilever beam's surface.

Table 2: Stability, sensitivity, and SNR of the frequency shifts measured by a Lorentzian fit and cross-correlation.

Frequency Shift Measurement Method	Linearity (R^2)	Stability (ppm)	Sensitivity (ppm/με)	SNR per με (1/με)
Lorentzian Fit	0.9996	0.250	1.319	5.283
Cross-Correlation	0.9999	0.124	1.055	8.517

The frequency sensitivity to strain of a cavity resonance from a 2-port SAW resonator with a 10 mm cavity length, and of a single IDT resonance, were then measured by measuring the shift of resonance peaks using the cross-correlation method as increasing mass was applied to the free end of the cantilever. Measurements of both resonance peaks were made on the same device. The IDT resonance was isolated by applying SAW attenuating silicone adhesive to the middle of the SAW cavity, allowing for direct comparison of their sensitivities. The frequency shifts produced by applying various amounts of strain to the cantilever beam surface are shown in Figure 7a. A linear fit was used to obtain the sensitivity of both resonances (slopes), as shown in Figure 7c, found to be -65.1 ± 3.0 Hz/με and -103.2 ± 0.2 Hz/με for the single IDT and Fabry-Pérot cavity, respectively. The single IDT peak demonstrates reasonable linearity with an R^2 value of 0.9813, while the cavity peak demonstrates excellent linearity with an R^2 value of 0.9999. The measured sensitivities and stabilities (standard deviation, no strain) of both resonances are shown in Table 3. By considering a minimum signal to noise ratio (SNR) of 2 (3 dB), the resolution of the cavity resonance peak of a 10 mm 2-port SAW resonator is found to be 234 nε.

Table 3: Sensitivity, stability, and strain resolution of the IDT resonance peak and the cavity resonance peak of a 2-port SAW resonator with a 10 mm cavity length, measured using the cross-correlation method.

Resonance Type	Sensitivity (Hz/με)	Average stability over 60 s (Hz)	SNR per με (1/με)	Strain resolution (με)
IDT	65.1 ± 3.0	383.5	0.170	11.7
10 mm cavity	103.1 ± 0.2	12.1	8.52	0.234

Additionally, the frequency shift of the 10 mm cavity resonance peak in response to small strains is shown in Figure 7b, where the frequency shift in response to 540 nε is clearly measurable.

The frequency shift of the cavity resonance peak due to the periodic application of a 500 g load is shown in Figure 8. The average frequency shifts of the unstrained and strained states are -1.6 ± 1.2 Hz and -2831.5 ± 1.7 Hz, respectively, where the small error in each state indicates excellent repeatability. Additionally, the frequency stability of the device is not affected significantly by repeated strains, being measured as 14.2 Hz after strain was applied.

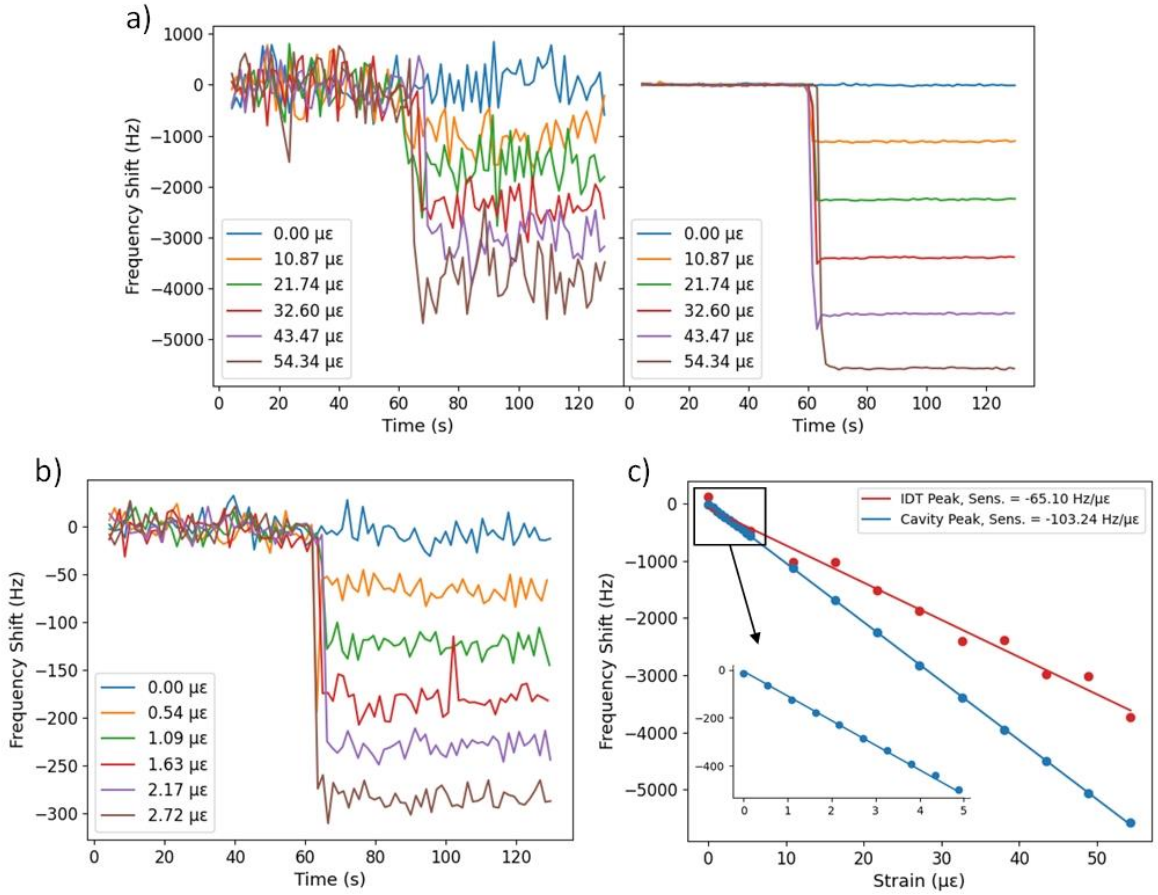

Figure 7: a) Frequency shift vs. time of the IDT resonance peak (left) and of the cavity resonance peak (right) of a 2-port SAW resonator with a 10 mm long cavity; b) frequency shift vs. time of the cavity resonance peak of a 2-port SAW resonator with a 10 mm long cavity (small strains). For both (a) and (b), the frequency shifts were determined using cross-correlation analysis of the measured spectra, and various masses were applied to the cantilever's free end at t = 60 s to produce strain on the device as noted in the legends. c) Frequency shift of both resonance peaks vs. applied strain on the cantilever beam surface (data from Part (a)). Inset shows the frequency shift in response to small strains for the cavity peak (data from Part (b)). A linear fit is applied to the data for the IDT and cavity peaks, with R^2 values of 0.9813 and 0.9999, respectively.

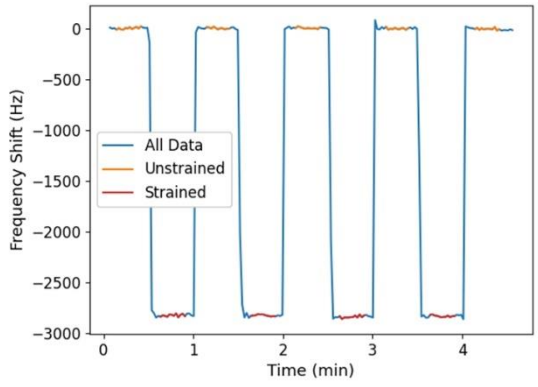

Figure 8: Repeatability of the frequency shift of the cavity resonance peak of a 2-port SAW resonator with a 10 mm long cavity in response to the periodic application of a 500 g load at the free end of the cantilever beam, measured using cross-correlation. Data considered for the unstrained and strained states are shown in orange and red, respectively.

3.5 Discussion

There is a marked improvement in the stability of the SAW Fabry-Pérot cavity resonance peak compared to the resonance peak of a single IDT. Noise in a frequency shift measurement is commonly attributed to thermal noise originating in the electrical circuitry [12], which produces thermal strain and affects the elastic coefficients of $LiNbO_3$ through their temperature dependence. Thermal noise therefore induces frequency noise due to random changes in the length of the devices and in SAW velocity. However, since thermal noise is localized to the IDTs, so are its deleterious effects. The IDT resonance, which only considers SAW generation and propagation within the IDT region, is strongly affected by thermal noise. Conversely, Fabry-Pérot resonance peaks in SAW cavities are formed by SAWs that travel along the entire cavity, so they are much less affected by thermal noise localized to the IDT regions. Furthermore, it is known that the VNA noise is proportional to the frequency sweep range [22]. As increasing the cavity length reduces the linewidth of cavity resonances, a smaller frequency sweep range can be used to track the resonance, which also reduces frequency noise. However, random fluctuations in temperature and strain along the cavity also introduce noise, such that the stability worsens beyond an optimal cavity length, as observed when the length was increased from 10 to 20 mm (Figure 5b).

The measured sensitivity of the cavity peak is greater that the sensitivity of the IDT peak by about 60% (Figure 7c), even though a cavity resonance should not

be significantly more sensitive to strain than an IDT resonance, as deduced theoretically in Subsection 2.1 (Eqs. (1) and (3)). However, it is expected that the cavity region experiences more strain due to its distance from the device edges and due to the lack of metallic IDT structures that locally increase the effective elastic modulus of the substrate surface, as discussed in Subsection 2.2 (Figure 2). The experimental improvement in sensitivity of the cavity peak (60%) is much larger than the expected improvement of 16% computed in Subsection 2.2 (Figure 2b). This is attributed to the non-uniformity of the adhesion between the SAW device and the cantilever beam, which could lead to some areas of the device experiencing more strain than others.

4. Conclusion

A SAW strain sensor based on acoustic Fabry-Pérot resonances from a 2-port SAW resonator was demonstrated. A theoretical analysis was performed to estimate the sensitivity of cavity resonances to strain and to predict strain distributions within the IDT and cavity regions of a device. The measured frequency stability of cavity peaks for different cavity lengths was compared to the frequency stability of a single IDT resonance peak. Stability was found to generally improve with cavity length, and was optimal for a cavity length of 10 mm. By bonding a 2-port SAW resonator of 10 mm cavity length to a straining cantilever beam, S_{11} spectra were measured as a function of applied strain, and frequency shifts determined accurately using a cross-correlation analysis. The frequency shift of the 2-port SAW resonator's cavity peak demonstrated excellent linearly with strain, its linear fit having an R^2 value of 0.9999. The strain sensitivity of the cavity peak was found to be -103.2 ± 0.2 Hz/με, about 60% better than a single IDT resonator. By considering a minimum signal to noise ratio (SNR) of 3 dB, the resolution of a 10 mm 2-port SAW resonator cavity peak was found to be only 234 nε.

Credit Author Statement

LK performed all measurements and analysis, carried out the FEM simulation, and wrote the manuscript. CC constructed the optical FBG setup and assisted in optical measurements. XB and PB directed the projected. All authors contributed to the interpretation of the results and to editing the manuscript.

Declaration of Conflict of Interest

The authors declare that they have no known competing financial interests or personal relationships that could have appeared to influence the work reported in this paper.

Acknowledgements

This work was supported in part by the Natural Sciences and Engineering Research Council of Canada (NSERC) under Grant STPGP 506628 and Grant RGPIN-2015-06071.

References

[1] A. Garcia-Alonso, J. Garcia, E. Castafio, I. Obleta, F. J. Gracla, "Strain sensitivity and temperature influence on sputtered thin films for piezoresistive sensors," *Sensors and Actuators A,37,* pp. 784-789, (1993).

[2] B. Han, J. Ou, "Embedded piezoresistive cement-based stress/strain sensor," *Sensors and Actuators A, 138,* pp. 294-298, (2007).

[3] A. Kersey et al., "Fiber grating sensors," *Journal of Lightwave Technology, 15,* pp. 1442-1463, (1997).

[4] A. Othonos, A. Alavie, S. MeIIe, S. Karr, R. Measures, "Fiber Bragg grating laser sensor," *Optical Engineering, 32,* pp. 2841-2846, (1993).

[5] B. Donohoe, D. Geraghty, G. O'Donnell, "Wireless calibration of a surface acoustic wave resonator as a strain sensor," *IEEE Sensors Journal, 11,* pp. 1026-1032, (2011).

[6] R. Stoney, D. Geraghty, G. O'Donnell, "Characterization of differentially measured strain using passive wireless surface acoustic wave (SAW) strain sensors," *IEEE Sensors Journal, 14,* pp. 722-728, (2014).

[7] Q. Li, J. Liu, B. Yang, L. Lu, Z. Yi, et al., "Highly sensitive surface acoustic wave flexible strain sensor," *IEEE Electron Device Letters, 40,* pp. 961-964, (2019).

[8] H. Xu, S. Dong, W. Xuan, U. Farooq, S. Huang, et al., "Flexible surface acoustic wave strain sensor based on single crystalline LiNbO3 thin film," *Applied Physics Letters, 112,* p. 5, (2018).

[9] H. Oh et al., "Development of a high-sensitivity strain measurement system based on a SH SAW sensor," *J. Micromech. Microeng., 22* , p. 10, (2012).

[10] U. Zwicker, "Strain sensor with commercial SAWR," *Sensors and Actuators, 17,* pp. 235-239, (1989).

[11] J. F. Dias, "Physical Sensors using SAW devices," *Hewlett-Packard Journal, 32,* pp. 18-20, 1981.

[12] C. Fua, K. Lee, K. Lee, S. Yanga, W. Wangba, "A stable and highly sensitive strain sensor based on a surface acoustic wave oscillator," *Sensors and Actuators A, 218,* pp. 80-87, (2014).

[13] V. Varadan et al., "Wireless passive IDT strain microsensor," *Smart Mater. Struct., 6,* pp. 745-751, (1997).

[14] T. Nomura, T. Kosaka, A. Saitoh, S. Furukawa, "Passive strain sensor using SH-SAW reflective delay line," *Ferroelectrics, 333,* pp. 121-129, (2006).

[15] B. Hu, "Fabrications of L-Band LiNbO3-Based SAW Resonators for Aerospace Applications," *Micromachines, 349,* p. 12, (2019).

[16] W. Soluch, M. Lysakowska, "Surface Acoustic Waves on X-Cut LiNbO3," *IEEE Transactions on Ultrasonics, 52,* pp. 145-147, (2005).

[17] H. Xu et al., "Flexible dual-mode surface acoustic wave strain sensor based on crystalline LiNbO3 thin film," *J. Micromech. Microeng., 29,* p. 10, (2019).

[18] COMSOL Multiphysics, Material Library User's Guide, 2018.

[19] L. Kelly, H. Northfield, S. Rashid, X. Bao, P. Berini, "Fabrication of high frequency SAW devices using tri-layer lift-off photolithography, in press," *Microelectr. Eng., 253,* p. 111671, (2022).

[20] AZO Materials, 2021. [Online]. Available: https://www.azom.com/.

[21] Z. Zhou, "Actualities and Development on Dynamic Monitoring and Diagnosis with Distributed Fiber Bragg Grating in Mechanical Systems," *Journal of Mechanical Engineering, 49,* pp. 55-69, (2013).

[22] Hewlett-Packard, "HP 8510C Network Analyzer Specifications," Hewlett-Packard Company, 1999.

4.4. Supplementary materials

Supplementary Material

DETAILS OF PHYSICS USED FOR FEM MODELLING

The Solid Mechanics interface was used to model stresses and strains. Since only small strains are considered (< 100 με), geometric linearity can be assumed. The solid mechanical equation of motion is given by:

$$\nabla_i \cdot T_{ij} = \rho \frac{\partial^2 u_j}{\partial t^2}$$

where T_{ij} is the surface force acting on each finite element of the mesh (*i.e.*, the stress), ρ is the mass density, u_j is the displacement of each finite element from its equilibrium position. Note subscripts i and j denote the cartesian directions. Stresses are related to strains, S_{kl}, by the elastic stiffness, ${c^E}_{ijkl}$:

$$T_{ij} = {c^E}_{ijkl} S_{kl}$$

A stationary solver is used to calculate the deformed state of the cantilever beam and SAW device in response to a static applied load. Since the solution is steady state, all time variant terms are equal to 0.

OPTIMIZATION OF CANTILEVER BEAM

In constructing an experimental strain setup, the design of the strain surface which the SAW device is bonded to is critical. For our experiment, a tapered cantilever beam was selected as the strain surface for two reasons: *i)* the tapered cantilever beam can be easily strained by placing small masses at the free end of the beam, and *ii)* highly uniform strain distributions are generated on its surface in response to loads. To optimize the geometries of the cantilever beam, a stationary solver was employed with the solid mechanics interface to calculate the strain distributions in the cantilever beam and a bonded SAW device in response to applied loads. Two parameters were defined to quantify the quality of the strain distributions. The first parameter, the strain difference (ε_{diff}), quantifies the % difference between the strain on the SAW device surface (ε_{SAW}) and the strain on the surrounding cantilever beam surface (ε_{can}):

$$\varepsilon_{diff} = \frac{|\varepsilon_{SAW} - \varepsilon_{can}|}{\frac{1}{2}(\varepsilon_{SAW} + \varepsilon_{can})}$$

The second parameter, the average strain on the SAW device surface ($avg(\varepsilon_{SAW})$) indicates how easily the surface is strained when the free end of the cantilever is loaded.

The cantilever beam was specified with the material properties of grade 316 stainless steel with a free length (L) of 50 cm and a free end width (w_i) of 5 mm. The fixed end width (w_0) and the thickness of the beam (h) were parametrically swept from 70 mm to 130 mm and 2 mm to 10 mm, respectively. The SAW device was specified with the material properties of 128° Y-X lithium niobate and dimensions of 20 mm x 3 mm x 0.5 mm to mimic the dimensions of a fabricated Fabry-Pérot resonator with a 10 mm delay line length. The SAW device was assumed to be perfectly fixed to the cantilever beam's surface and was positioned 2 cm away from the fixed end of the cantilever beam. For each value of w_0 and h, ε_{diff} and $avg(\varepsilon_{SAW})$ were calculated in response to a 1 N load applied in the negative y-direction at the cantilever's free end, as seen in Figure 1a/b).

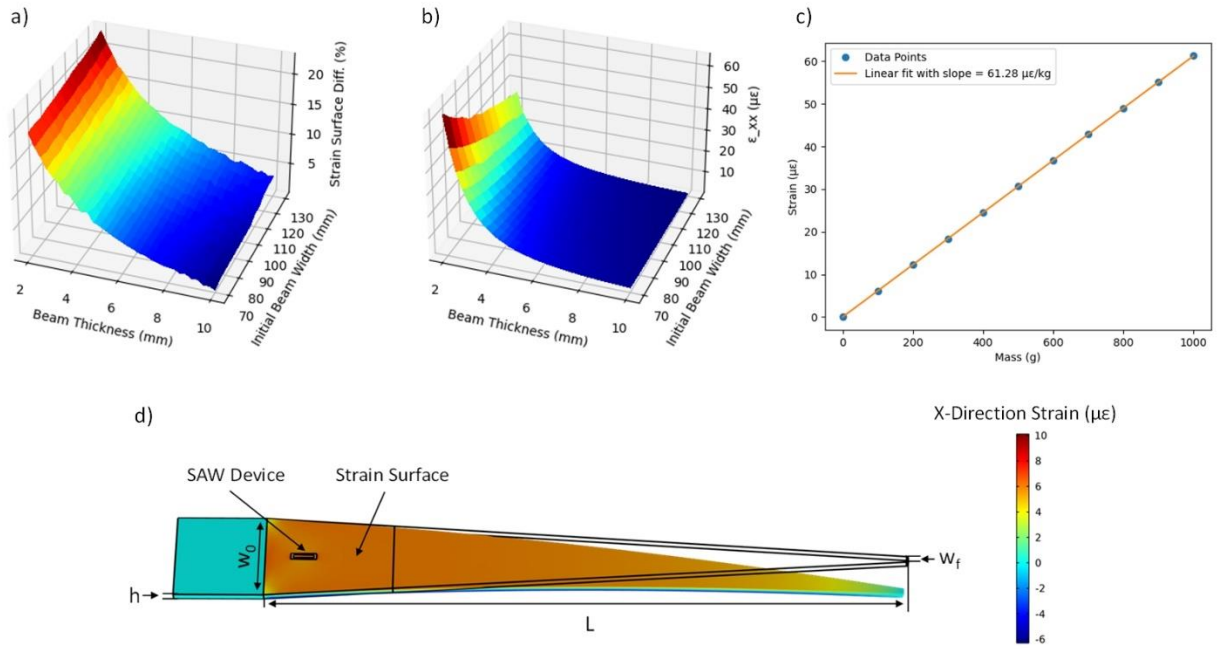

Figure 1: Optimization of cantilever beam through COMSOL simulation. a) The strain difference between the SAW and cantilever beam surfaces as a function of the initial width and thickness of the cantilever beam. b) The average x-direction strain on the SAW surface as a function of the initial width and thickness of the cantilever beam. c) The average x-direction strain over the SAW device surface as a function of the applied mass at the cantilever beam's free end (h = 6 mm, w_0 = 70 mm). d) Deformed surface map of the x-direction strain on the cantilever beam (h = 6 mm, w_0 = 70 mm).

By creating a cut-off value for $\boldsymbol{\varepsilon_{diff}}$ of 10%, above which cantilever geometries are deemed unacceptable, the remaining geometries can be compared by their ability to produce strain at the SAW device surface. The geometry which had a value of $\boldsymbol{\varepsilon_{diff}}$ below 10% and the highest strain at the SAW device surface had an initial width of 70 mm and a thickness of 6 mm. It can be seen in Figure 1c) that the strain produced on the SAW device surface has a linear relationship with the mass applied to the cantilever beam's free end. The calculated relation of strain produced at the SAW device surface to applied mass of the cantilever beam was 61.28 με/kg. In Figure 1d) the strain produced on the cantilever beam is essentially constant along most of the beam's length.

4.5 Comparison with existing strain sensors

SAW devices have been used for strain sensing for over 40 years. However, in recent years, they have gained renewed interest due to their ability for passive wireless interrogation and ability to withstand rugged conditions as required in the aerospace, automotive, and civil engineering fields. One application of SAW strain sensors is for providing real time strain/stress and vibration measurements in turbine engine structures. The high temperatures of turbine engine environments prevent the use of traditional strain gauges. Compared to alternatives such as piezoresistive [33], [34] or optical fiber strain sensors [35], [36], SAW sensors are not only much better at withstanding rugged conditions, but also exhibit superior dynamic range, low system complexity, and are inexpensive.

Our SAW strain sensor can be compared with SAW strain sensors from the literature. In [44], both the frequency shift stability and frequency shift sensitivity to strain of a SAW oscillator on 128 Y-X^{o} lithium niobate were investigated, with a strain sensitivity of 126 Hz/με @ 151 MHz and a frequency stability of 11 Hz. Considering a minimum SNR of 3dB, this corresponds to a state-of-the-art strain resolution of 174 nε. We demonstrated a SAW strain sensor based on Fabry-Perot resonances from a 2-port SAW resonator in Chapter 4.3., having a strain sensitivity of 103 Hz/με @ 97.7 MHz, frequency stability of 12 Hz, and a strain resolution of 234 nε. Thus, our device exhibits similar performance to the state-of-the-art. It should be noted that the SAW oscillator, like the Fabry-Perot resonances from a 2-port SAW resonator, also considers phase information of SAWs propagating between two IDTs, and therefore should also benefit from many of the same benefits as the Fabry-Perot resonances from a 2-port SAW resonator as discussed in Chapter 4.3.

4.5. Stability of Fabry-Pérot resonance peaks as a function of the operating frequency of the device

It is well known that as the operating frequency of SAW strain sensors increase, their sensitivity increases as well [14]. This can be shown by considering the equation for the fractional frequency shift of Fabry-Pérot resonance peaks of a 2-port SAW resonator in response to strain:

$$\frac{\Delta f_c}{f_{c_0}} = \frac{\Delta v_{SAW}}{v_{SAW_0}} - \varepsilon_{xx}$$

Note that the equation is the same for IDT resonance and follows the same analysis. However, if we consider the frequency shift itself:

$$\Delta f_{IDT} = f_{IDT_0}\left(\frac{\Delta v_{SAW}}{v_{SAW_0}} - \varepsilon_{xx}\right)$$

We find that Δf_{IDT} is proportional to the operating frequency. Since sensitivity, S, is defined as the partial derivative of the measurand (f_{IDT}) with respect to strain, the sensitivity can be approximated as:

$$S = \Delta f_{IDT}/\Delta\varepsilon$$

Therefore, the frequency sensitivity of resonance peaks is proportional to the operating frequency. Highly sensitive SAW strain sensors have been proposed by increasing the operating of the employed SAW device to frequencies in the GHz range.

However, when using a SAW strain sensor to detect small amounts of strain, the stability of the device, σf_{IDT}, (*i.e.*, the standard deviation of the fluctuations in the baseline signal in the absence of strain) becomes equally important as its sensitivity. The minimum resolvable strain can be defined as the minimum strain that produces a frequency shift which is at twice as large as the fluctuations in the baseline:

$$\varepsilon_{min} = \frac{2S}{\sigma f_{IDT}}$$

Thus, for a device to have a better minimum resolvable strain, improvements in the sensitivity must be larger than the reduction in stability.

If we consider measures of frequency shift in terms of ppm ($\Delta f_{IDT}/f_{IDT_0} \times 10^6$), we find that the sensitivity is constant as a function of the operating frequency. We can now compare the stabilities for devices of different operating frequencies and see if the fluctuations of the baseline in terms of ppm reduce or increase. Frequency fluctuations of cavity resonances from 10 mm-long 2-port SAW resonators with values of λ_{IDT} of 40, 16, 8, and 4 μm and cavity peaks at frequencies of 97.7, 243.8, 494.3, 995.0 MHz, respectively, were measured over the course of 60 minutes as seen in Figure 7 a). The measured stability of the frequency shift and its gradient, the frequency shift rate, can be seen in Figure 7 b).

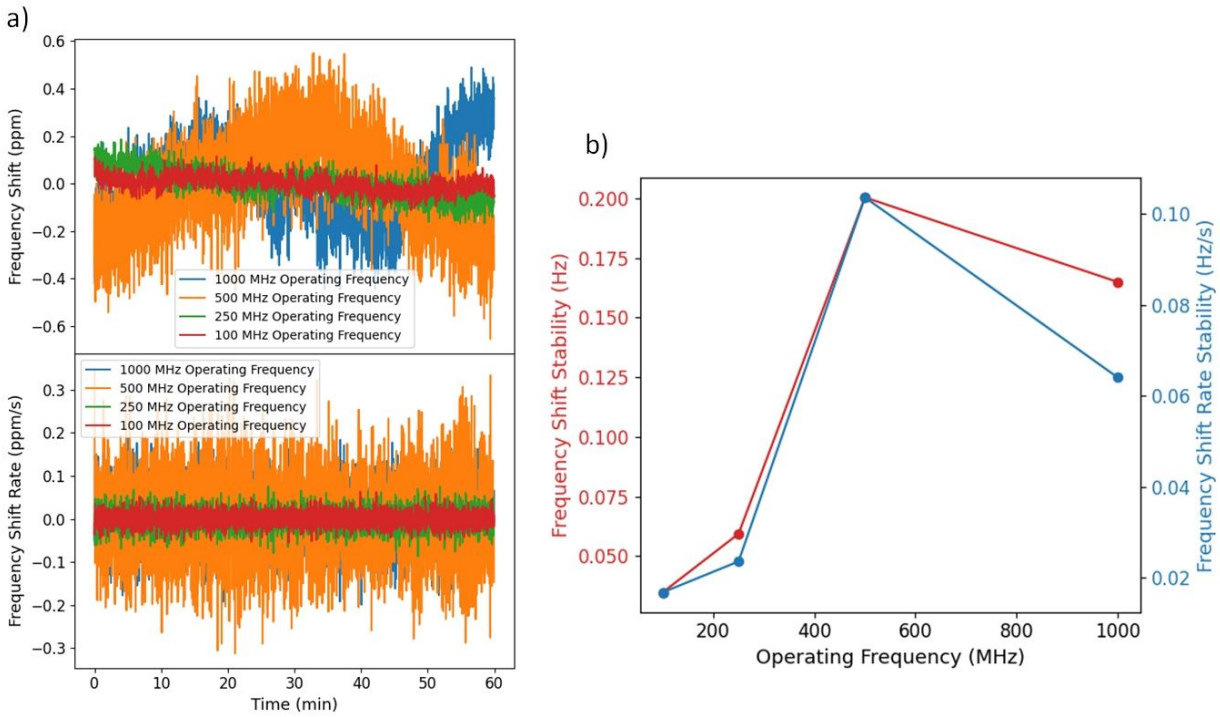

Figure 7: a) Frequency shift of cavity resonant peaks vs. time (top panel) and frequency shift rate vs. time (bottom panel) for cavity resonance peaks from 10 mm-long 2-port SAW resonators with operating frequencies of at 97.7, 243.8, 494.3, 995.0 MHz operating frequencies. b) Frequency shift stability and frequency shift rate stability of resonance peaks from 2-port SAW resonators with different operating frequencies. The stabilities are taken as the standard deviation over time of the traces in Part (a).

As seen in Figure 7 a) and b), the ppm frequency stability of a 10 mm long 2-port SAW resonator tends to reduce as the operating frequency increases, implying the strain resolution will be optimal for the

40 μm λ_{IDT} device. Considering that one of the main contributions to the frequency fluctuations in the baseline signal is thermal noise which has a linear temperature coefficient of frequency in 128° Y-X lithium niobate, its not surprising that the stability in ppm does not improve with increasing operating frequency. Additionally, frequency noise from the VNA is also expected to increase with operating frequency [47]. Therefore, for our fabricated devices, the 10 mm long 2-port SAW resonator with $\lambda_{IDT} = 40$ μm will have the minimum resolvable strain and is best suited for small strain measurements.

Chapter 5 – Conclusion

5.1 Summary and contributions

The presented thesis outlined a study of the fabrication of high frequency SAW devices using tri-layer photolithography (Chapter 2), a method of determining SAW parameters from acoustic Fabry-Pérot spectra (Chapter 3), and an investigation into the use of Fabry-Pérot resonance modes from a 2-port SAW resonator to produce a high-resolution strain sensor (Chapter 4). SAW sensors are known to be more sensitive at higher frequencies. However, resolution limits of traditional photolithographic techniques prevent the realization of high frequency SAW devices. A previously reported tri-layer photolithography process intended for use on SiO_2 or Si substrates was modified for compatibility with piezoelectric/pyroelectric materials enabling the fabrication of SAW devices (Chapter 2). The tri-layer consists of layers of LOR, BARC, and PR, where the addition of the BARC layer prevents back reflection of exposure light, improves the structural integrity of the lithographic stack, and decouples the PR and LOR development, improving resolution over traditional lift-off photolithography techniques. The process was employed to fabricate SAW devices with a 4 μm IDT pitch and feature sizes as small as 1 μm on 128◦ Y-X cut lithium niobate with high yield (Chapter 2.3, Fig. 3). Fabricated IDTs were electrically characterized, and the frequency of the excited SAW mode was determined as 994.5 MHz. Numerical modelling was carried out to determine the theoretical operating frequency of the SAW device as 995.5 MHz (Chapter 2.3, Fig. 8). The measured and computed frequencies are in excellent agreement, with only a 0.10% difference. These results, in addition to physical measurements obtained on fabricated devices, validate the tri-layer photolithography process as capable of reliably fabricating high-quality GHz SAW devices using only standard UV contact photolithography equipment. The fabrication of high-frequency SAW devices was thus enabled by this process, allowing for their investigation as a SAW strain sensor in Chapter 4.

A method of determining SAW parameters such as velocity, attenuation, and reflection through acoustic Fabry-Pérot spectra was proposed and demonstrated in Chapter 3. Theory adopted from the optical

Fabry-Pérot resonator was expressed for acoustic waves, and equations for the free spectral range and linewidth of cavity peaks were determined. 2-port SAW resonators with IDT pitches of 16 and 8 μm, and varying cavity lengths, were fabricated on 128° Y-X lithium niobate and used to generate SAWs which reflect between two IDTs acting as Bragg reflectors and forming an acoustic cavity. The frequency spacing of cavity peaks in the S_{11} spectra is used to calculate the free surface SAW velocity, the correction to the free surface cavity length, and the reflection phase of the IDTs (Chapter 3.3 Figure 4). The linewidth of the spectral peaks is then used to calculate the intensity attenuation coefficient and the reflection amplitude of the IDTs (Chapter 3.3 Figure 5). The method proposed is easy to implement and intuitive, providing an accessible method for determining key cavity characteristics. A full derivation of the phase condition for acoustic cavity resonances and the linewidth of cavity peaks was also included in the appendix of Chapter 3.3.

A SAW strain sensor based on acoustic Fabry-Pérot resonances from a 2-port SAW resonator was presented in Chapter 4. A 2-port SAW resonator with a larger number of IDT finger pairs which reflect and confine SAWs between the IDTs, forming an acoustic Fabry-Pérot cavity, is used for strain sensing. A theoretical analysis of the frequency sensitivity of the cavity resonances was presented, and a numerical analysis was performed to predict strain distributions in the IDT and cavity regions of the device. The measured 60-minute stability of cavity peaks for different cavity lengths was measured to determine the cavity length which exhibits optimal stability (Chapter 4.3 Figure 5). It is found that the stability of cavity resonances improves with cavity length up to 10 mm. Then, by bonding a 2-port SAW resonator of 10 mm cavity length to a straining cantilever beam, spectra were measured as a function of applied strain, and frequency shifts determined using cross-correlation analysis (Chapter 4.3 Figure 6). The frequency shift of the 2-port SAW resonator's cavity peak demonstrated excellent linearly with strain, its linear fit having an R^2 value of 0.9999 (Chapter 4.3 Figure 7). The strain sensitivity of the cavity peak was found to be -103.2 ± 0.2 Hz/με with a stability of 12.1 Hz. By considering a minimum signal to noise ratio (SNR) of 3 dB, the resolution of a 10 mm 2-port SAW resonator cavity peak was found to be 234 nε. Additional details

including the equations used for FEM analysis and the FEM optimization of the cantilever beam geometries were included as supplementary materials. An investigation on the frequency stability of 10 mm-long 2-port SAW resonators of different operating frequencies was performed and it was found that the 40 μm λ_{IDT} device had the best stability and would have the highest resolution as a SAW strain sensor (Chapter 4.5 Figure 1).

5.2 Suggestions for future work

The tri-layer photolithography method presented in Chapter 2 enables the fabrication of high frequency SAW devices using UV photolithography. In this process we constrained thermal ramps to be below 2 ^{o}C/min to prevent damaging piezoelectric/pyroelectric substrates. While this thermal ramp rate was effective for producing high quality results, thermal ramps would take as long as 3 hours each and thus processing times were consequently long. It may be possible to increase thermal ramp rates without significantly impacting the quality of results. A study on the thermal ramp rate below which lithium niobate remains stable in a lithography process would be highly useful in selecting a thermal ramp rate and minimizing time spent thermally cycling samples in the process.

SAW resonators consisting of two IDTs with many fingers separated by a free cavity length were presented. Owing to the large number of IDT fingers, reflection of the IDTs was high, and a strong cavity effect was produced between the IDTs, leading to the appearance of cavity peaks in the measured S_{11} spectra. These cavity peaks were exploited to measure SAW parameters in Chapter 3 and to be used as the basis of a SAW strain sensor in Chapter 4. However, there are other options aside from IDT fingers to produce coherent SAW reflection and form a SAW cavity. Electrically disconnected metal strips can be deposited on the substrate surface with a periodicity of $\lambda_{IDT}/2$, forming a Bragg reflecting array. Thus, it would be possible to confine SAWs in the cavity between the IDTs using a Bragg reflecting array of metal strips on the outer sides of the IDTs. This would have two clear advantages over using the large number of IDT fingers: i) IDTs are bidirectional devices, meaning they generate SAWs in both the +ve and -ve

directions perpendicular to the IDT fingers on the substrate surface. By implementing a Bragg reflecting array with many reflecting elements on either side of the SAW resonator, most of the SAW energy propagating away from the cavity will be reflected back towards the cavity, improving the efficiency of the device. ii) When the number of IDT fingers increase, the Q-factor of the IDT resonance increases as well. This means that only a narrow band of SAW frequencies can be excited by the IDT, imposing a limitation on the observable frequency response of the device. By reducing the number of IDT fingers, a larger range of SAW frequencies can be generated, while high reflection/confinement in the cavity can still be obtained using the aforementioned reflecting arrays. Using the SAW parameters measured in Chapter 3, a 2-port SAW resonator could be accurately designed to have optimal performance for its intended application.

In Chapter 4 (and throughout the thesis), 128^{o} Y-X lithium niobate was used as the substrate material for SAW devices. This substrate material was chosen due to its high piezoelectric coupling and low SAW attenuation. However, the temperature sensitivity of 128^{o} Y-X lithium niobate is a significant drawback when designing a SAW strain sensor. Thus, other substrates materials such as quartz and lithium tantalate should be considered more seriously for future work. Additionally, an FEM analysis method for calculating the frequency shift sensitivity to strain could be developed. This would allow for a comparison of the frequency shift sensitivity to strain for SAW devices with different substrate materials and determination of the optimal substrate material for strain sensing.

Appendix

i. Voigt notation

Owing to the fact that stress and strain matrices are symmetric, an abbreviated subscript notation called Voigt notation can be used to reduce the complexity of tensors in the governing equations. The components of the stress matrix are given as:

$$T_{ij} = \begin{bmatrix} T_{11} & T_{12} & T_{13} \\ T_{21} & T_{22} & T_{23} \\ T_{31} & T_{32} & T_{33} \end{bmatrix} = \begin{bmatrix} T_1 & T_6 & T_5 \\ T_6 & T_2 & T_4 \\ T_5 & T_4 & T_3 \end{bmatrix}$$

Thus, the stress can be reduced from a 2-dimensional 3x3 matrix to a 1-dimensional six-element vector:

$$T_i = \begin{bmatrix} T_1 \\ T_2 \\ T_3 \\ T_4 \\ T_5 \\ T_6 \end{bmatrix}$$

The strain matrix can be abbreviated similarly as S_j with $(j = 1 \rightarrow 6)$. The elastic stiffness tensor $({c^E}_{ij})$ can then be reduced from a 4th order $3 \times 3 \times 3 \times 3$ tensor into a 2nd order 6×6 tensor, significantly reducing its size and complexity. The piezoelectric coupling tensor (e_{ij}) is reduced from a 3rd order $3 \times 3 \times 3$ tensor to a 2nd order 3×6 tensor. Owing to the reduced complexity, the elastic stiffness and piezoelectric coupling tensors are almost always presented in Voigt notation.

ii. Crystal orientations

Nomenclature

When dealing with anisotropic crystals, a nomenclature for crystal orientation must be established as its material properties are direction dependent. The nomenclature that is used popularly works by first defining two directions: the direction parallel to the surface normal and the direction parallel to the

propagation axis, both defined with respect to crystalline axes. The two directions then proceed the name of the crystal material. For example: 128° Y-X lithium niobate has a surface normal parallel to the crystalline y-axis rotated 128° about the crystalline x-axis, and a propagation direction parallel to the crystalline y-axis.

Crystal Rotations

Since crystal properties are direction dependent, they are provided in tensor form. Thus, when it is desired to perform analysis on a specific crystal orientation, the crystal properties should be rotated so that the analysis orientation is aligned with the desired crystal orientation. To calculate the displacement field and electric field associated with mechanical waves in a piezoelectric substrate, we require four material properties: Density (ρ_0), permittivity (ε_{ij}), elastic stiffness ($c^E{}_{ijkl}$) and piezoelectric coupling (e_{ijk}). Since density is direction invariant, it is constant among all reference frames and requires no rotation. However, permittivity, elastic stiffness, and piezoelectric coupling are tensor values and thus require rotation when performing an analysis on a rotated crystal plane.

Relative permittivity is a 2nd order tensor and can be rotated using standard rotation matrices.

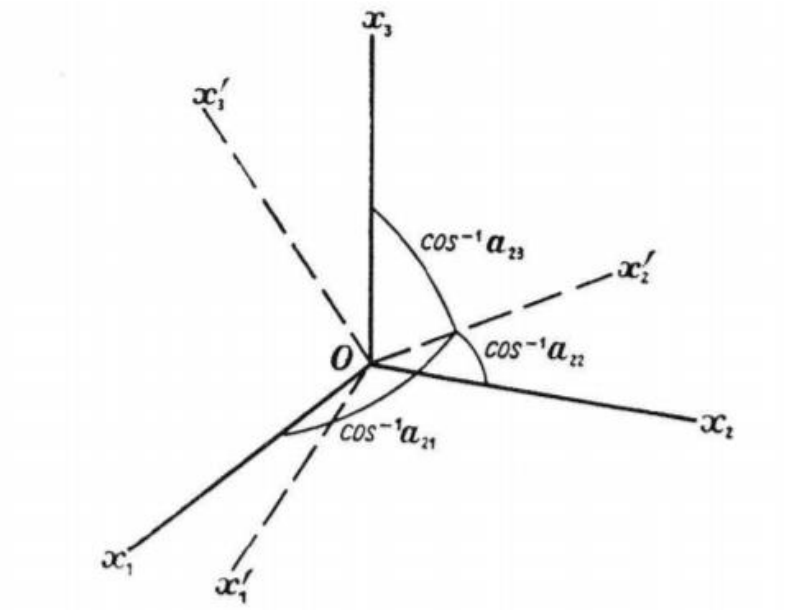

Figure 8: Rotation of coordinates from an initial set of axes $\{x_1, x_2, x_3\}$ and a final set of axes $\{x_1', x_2', x_3'\}$ [48]

To rotate from the initial set of axes $\{x_1, x_2, x_3\}$ to the final set of axes $\{x_1', x_2', x_3'\}$, we can create a table of direction cosines to relate the two axes [48]:

$$\begin{array}{cccc} & x_1 & x_2 & x_3 \\ x_1' & \cos(\theta_{11}) & \cos(\theta_{12}) & \cos(\theta_{13}) \\ x_2' & \cos(\theta_{21}) & \cos(\theta_{22}) & \cos(\theta_{23}) \\ x_3' & \cos(\theta_{23}) & \cos(\theta_{32}) & \cos(\theta_{33}) \end{array} = \begin{bmatrix} a_{11} & a_{12} & a_{13} \\ a_{21} & a_{22} & a_{23} \\ a_{31} & a_{32} & a_{33} \end{bmatrix} = a_{ij}$$

where θ_{ij} is the angle between the i^{th} axis ($i = 1,2,3$) in the final frame and the j^{th} axis ($j = 1,2,3$) in the initial frame. A vector expressed in terms of components parallel to the axes of the initial frame (p_j) can be equivalently expressed in terms of the components parallel to the axes of the final frame (p_i') through multiplication with a_{ij}:

$$p_i' = a_{ij} p_j$$

Material properties which are given in Voigt notation such as the piezoelectric coupling (e_{ijk}) and elastic stiffness (${c^E}_{ijkl}$), require special rotation matrices: the Bond stress and strain matrices [49].

The Bond stress matrix (M_{ij}) satisfies the following equation:

$$T_i' = M_{ij} T_j$$

Where T_j $(j = 1 \rightarrow 6)$ are the Voigt notation components of the stress tensor in the original coordinate system and T_i' $(i = 1 \rightarrow 6)$ are the Voigt notation components of the stress tensor in the rotated coordinate system. The bond stress matrix M_{ij} can be written as:

$$M_{ij} = \begin{bmatrix} a_{xx}^2 & a_{xy}^2 & a_{xz}^2 & 2a_{xy}a_{xz} & 2a_{xz}a_{xx} & 2a_{xx}a_{xy} \\ a_{yx}^2 & a_{yy}^2 & a_{yz}^2 & 2a_{yy}a_{yz} & 2a_{yz}a_{yx} & 2a_{yx}a_{yy} \\ a_{zx}^2 & a_{zy}^2 & a_{zz}^2 & 2a_{zy}a_{zz} & 2a_{zz}a_{zx} & 2a_{zx}a_{zy} \\ a_{yx}a_{zx} & a_{yy}a_{zy} & a_{yz}a_{zz} & a_{yy}a_{zz} + a_{yz}a_{zy} & a_{yx}a_{zz} + a_{yz}a_{zx} & a_{yy}a_{zz} + a_{yx}a_{zy} \\ a_{zx}a_{xx} & a_{zy}a_{xy} & a_{zz}a_{xz} & a_{xy}a_{zz} + a_{xz}a_{zy} & a_{xz}a_{zx} + a_{xx}a_{zz} & a_{xx}a_{zy} + a_{xy}a_{zx} \\ a_{xx}a_{yx} & a_{xy}a_{yy} & a_{xz}a_{yz} & a_{xy}a_{yz} + a_{xz}a_{yy} & a_{xz}a_{yx} + a_{xx}a_{yz} & a_{xx}a_{yy} + a_{xy}a_{yx} \end{bmatrix}$$

Similarly, the Bond strain matrix (N_{ij}) satisfies the following equation:

$$S_i' = N_{ij} S_j$$

Where S_j $(j = 1 \rightarrow 6)$ are the Voigt notation components of the strain tensor in the original coordinate system and S_i' $(i = 1 \rightarrow 6)$ are the Voigt notation components of the strain tensor in the rotated coordinate system. The bond stress matrix can be written explicitly as:

$$N_{ij} = \begin{bmatrix} a_{xx}^2 & a_{xy}^2 & a_{xz}^2 & a_{xy}a_{xz} & a_{xz}a_{xx} & a_{xx}a_{xy} \\ a_{yx}^2 & a_{yy}^2 & a_{yz}^2 & a_{yy}a_{yz} & a_{yz}a_{yx} & a_{yx}a_{yy} \\ a_{zx}^2 & a_{zy}^2 & a_{zz}^2 & a_{zy}a_{zz} & a_{zz}a_{zx} & a_{zx}a_{zy} \\ 2a_{yx}a_{zx} & 2a_{yy}a_{zy} & 2a_{yz}a_{zz} & a_{yy}a_{zz} + a_{yz}a_{zy} & a_{yx}a_{zz} + a_{yz}a_{zx} & a_{yy}a_{zz} + a_{yx}a_{zy} \\ 2a_{zx}a_{xx} & 2a_{zy}a_{xy} & 2a_{zz}a_{xz} & a_{xy}a_{zz} + a_{xz}a_{zy} & a_{xz}a_{zx} + a_{xx}a_{zz} & a_{xx}a_{zy} + a_{xy}a_{zx} \\ 2a_{xx}a_{yx} & 2a_{xy}a_{yy} & 2a_{xz}a_{yz} & a_{xy}a_{yz} + a_{xz}a_{yy} & a_{xz}a_{yx} + a_{xx}a_{yz} & a_{xx}a_{yy} + a_{xy}a_{yx} \end{bmatrix}$$

The rotation matrices require to rotate each material property can be determined through the governing equations. Let's consider the piezoelectric constitutive equation for electric displacement field D_i:

$$D_i = \varepsilon_{ij} E_j + e_{im} S_m$$

Since D_i is a first order tensor it can be rotated through multiplication of a_{ij}:

$$D_i{}' = a_{ij}D_j$$

$$D_i{}' = a_{ij}\varepsilon_{jk}E_k + a_{ik}e_{km}S_m$$

and $E_k = {a_{lk}}^{-1}E_l{}'$ and $S_m = {N_{nm}}^{-1}S_n{}'$

$$D_i{}' = a_{ij}\varepsilon_{jk}{a_{lk}}^{-1}E_l{}' + a_{ik}e_{km}{N_{nm}}^{-1}S_n{}'$$

$\therefore\ \varepsilon_{il}{}' = a_{ij}\varepsilon_{jk}{a_{lk}}^{-1}$and $e_{in}{}' = a_{ik}e_{km}{N_{nm}}^{-1}$

where $(i, j, k, l = 1,2,3\ and\ m, n = 1 \rightarrow 6)$The rotation of the compliance matrix can be found by examining Hooke's law:

$$T_i = {c^E}_{ij}S_j$$

where the stress matrix can be rotated using the Bond stress matrix, M_{ki}:

$$T_k{}' = M_{ki}T_i$$

$$T_k{}' = M_{ki}{c^E}_{ij}S_j$$

And the strain matrix can be rotated using the Bond strain matrix, N_{lj}:

$$S_j = {N_{lj}}^{-1}S_l{}'$$

Thus, the stress becomes:

$$T_k{}' = M_{ki}{c^E}_{ij}{N_{lj}}^{-1}S_l{}'$$

$$\therefore {c^E}_{kl}{}' = M_{ki}{c^E}_{ij}{N_{lj}}^{-1}$$

References

[1] L. Rayleigh, "On waves propagated along the plane surface of an elastic solid," *Proceedings of the London Mathematical Society, 11,* pp. 4-11, (1885).

[2] R. White, F. Voltmer, "Direct piezoelectric coupling to surface elastic waves," *Appl. Phys. Lett., 7,* pp. 314-316, (1965).

[3] C. Campbell, Surface Acoustic Wave Devices and their Signal Processing Applications, Academic Press, Inc., 1989.

[4] J. Shi, D. Ahmed, X. Mao, S. Lin, A. Lawita and T. Huang, "Acoustic tweezers: patterning cells and microparticles using standing surface acoustic waves (SSAW)," *Lab on a Chip 9,* pp. 2890-2895, (2009).

[5] D. S. Ballantine, Acoustic wave sensors theory, design, and physico-chemical applications, San Diego: Academic Press, 1997.

[6] Y. Chu, P. Kharel, W. Renninger et al., "Quantum acoustics with superconducting qubits," *Science 358,* pp. 199-202, (2017).

[7] K. Satzinger, Y. Zhong, H. Chang, et al., "Quantum control of surface acoustic-wave phonons," *Nature 563,* pp. 661-665, (2018).

[8] B. Moores, L. Sletten, J. Viennot, K. Lehnert, "Cavity quantum acoustic device in the multimode strong coupling regime," *Physical Review Letters 120,* (2018).

[9] M. Schuetz, J. Knorzer, G. Giedke et al., "Acoustic traps and lattices for electrons in semiconductors," *Physical Review X 7,* (2017).

[10] P. Delsing, A. Cleland, M. Schuetz, et al., "The 2019 surface acoustic waves roadmap," *Journal of Physics D: Applied Physics 52,* p. 40, (2019).

[11] J. Vaughan, The Fabry-Perot Interferometer: History, Theroy, Practice and Application, Taylor and Francis Gorup, LLC, 1989.

[12] Y. Xu, W. Fu, C. Zou, et al., "High quality factor surface Fabry-Perot cavity of acoustic waves," *Applied Physics Letters 112,* (2018).

[13] J. Choma and W. Chen, Feedback networks: theory and circuit applications, World Scientific Publishing, 2008.

[14] B. Hu, "Fabrications of L-Band LiNbO3-Based SAW Resonators for Aerospace Applications," *Micromachines, 349,* p. 12, (2019).

[15] M. Hatzakis, B.J. Canavello, J.M. Shaw, "Single-step optical lift-off process," *IBM journal of research and development 24,* pp. 452-460, (1980).

[16] H. Smith, F. Bachner, N. Efremow, "A high-yield photolithographic technique for surface wave devices," *J. Electrochem. Soc. 118,* pp. 821-825, (1971).

[17] H. I. Smith, "Fabrication techniques for surface-acoustic-wave and thin-film optical devices," *Proceedings of the IEEE 62,* pp. 1361-1387, (1974).

[18] J. Mei, N. Zhang, J. Friend, "Fabrication of surface acoustic wave devices on lithium niobate," *J. Vis. Exp. 160,* (2020).

[19] N. Yoshioka, A. Sakai, H. Morimoto, K. Hosono, Y. Watakabe, S. Wadaka, "Fabrication of surface acoustic wave devices By using x-ray lithography," *Journal of Vacuum Science and Technology B 7,* pp. 1688-1691, (1989).

[20] W.H. Brünger, L.-M. Buchmann, M. Kreutzer, M. Torkler, G. Zwicker, B. Fleischmann, "Fabrication of 3.5 GHz surface acoustic wave filters by ion projection lithography," *Microelectronic Engineering 17,* pp. 245-248, (1992).

[21] M. Itoh, H. Gokan, S. Esho, K. Asakawa, "Fabrication process for surface acoustic wave filters having 0.5 μm finger period electrodes," *Journal of Vacuum Science and Technology 20,* pp. 21-25, (1982).

[22] H. Sato, T. Meguro, K. Yamanouchi, K. Shibayama, "Optimum cut for rotated Y-cut LiNbO3 crystals used as the substrate of elastic surface wave filters," *The Journal of the Acoustical Society of Japan 30,* pp. 549-556, (1974).

[23] A. Stefanescu, A. Müller, I. Giangu, A. Dinescu, G. Konstantinidis, "Influence of Au-based metallization on the phase velocity of GaN on Si surface acoustic wave resonators," *IEEE Electronic Device Letters 37,* pp. 321-324, (2016).

[24] J. Temmyo, I. Kotaka, T. Inamura, S. Yoshikawa, "Precise measurement of SAW propagation velocity on LiNbO3," *IEEE Transactions on Sonics and Ultrasonics 27,* pp. 218-219, (1980).

[25] M. Hirabayashi, "A technique for measuring phase velocities of surface acoustic waves using comb filters," *Japanese Journal of Applied Physics 20,* pp. 53-56, (1981).

[26] M. Hirabayashi, "Precise measurement of phase velocity of surface acoustic waves using parallel comb filters," *Electronics letters 25,* pp. 1380-1381, (1989).

[27] G. Cambon, M. Rouzeyre, G. Simon, "Optical probing of surface Rayleigh waves," *Applied Phyiscs Letters 18,* pp. 295-298, (1971).

[28] K. Suzuki, M. Nishikawa, "“Sing-around” method for acoustic surface-wave velocity measurements using an optical probe," *Japanese Journal of Applied Physics 13,* pp. 1216-1218, (1974).

[29] A. Slobodnik, "Microwave frequency acoustic surface wave propagation losses in LiNbO3," *Applied Physics Letters 14,* pp. 94-96, (1969).

[30] M. Ryzy, T. Grabec, J. Osterreicher, M. Hettich, I. Veres, "Measurement of coherent surface acoustic wave attenuation in polycrystalline aluminum," *AIP Advances 8,* (2018).

[31] P. Wright, "Modeling and experimental measurements of the reflection properties of SAW metallic gratings," *iEE 1984 Ultrasonics Symposium,* pp. 54-63, (1984).

[32] Waldemar Soluch, "Application of Synchronous Two-Port Resonators for Measurement of SAW Parameters in Piezoelectric Crystals," *IEEE Transactions on Ultrasonics, Ferroelectrics and Frequency Control, 45,* pp. 1113-1116, (1998).

[33] A. Garcia-Alonso, J. Garcia, E. Castafio, I. Obleta, F. J. Gracla, "Strain sensitivity and temperature influence on sputtered thin films for piezoresistive sensors," *Sensors and Actuators A,37,* pp. 784-789, (1993).

[34] B. Han, J. Ou, "Embedded piezoresistive cement-based stress/strain sensor," *Sensors and Actuators A, 138,* pp. 294-298, (2007).

[35] A. Kersey et al., "Fiber grating sensors," *Journal of Lightwave Technology, 15,* pp. 1442-1463, (1997).

[36] A. Othonos, A. Alavie, S. MeIIe, S. Karr, R. Measures, "Fiber Bragg grating laser sensor," *Optical Engineering, 32,* pp. 2841-2846, (1993).

[37] B. Donohoe, D. Geraghty, G. O'Donnell, "Wireless calibration of a surface acoustic wave resonator as a strain sensor," *IEEE Sensors Journal, 11,* pp. 1026-1032, (2011).

[38] R. Stoney, D. Geraghty, G. O'Donnell, "Characterization of differentially measured strain using passive wireless surface acoustic wave (SAW) strain sensors," *IEEE Sensors Journal, 14,* pp. 722-728, (2014).

[39] Q. Li, J. Liu, B. Yang, L. Lu, Z. Yi, et al., "Highly sensitive surface acoustic wave flexible strain sensor," *IEEE Electron Device Letters, 40,* pp. 961-964, (2019).

[40] H. Xu, S. Dong, W. Xuan, U. Farooq, S. Huang, et al., "Flexible surface acoustic wave strain sensor based on single crystalline LiNbO3 thin film," *Applied Physics Letters, 112,* p. 5, (2018).

[41] H. Oh et al., "Development of a high-sensitivity strain measurement system based on a SH SAW sensor," *J. Micromech. Microeng., 22* , p. 10, (2012).

[42] U. Zwicker, "Strain sensor with commercial SAWR," *Sensors and Actuators, 17,* pp. 235-239, (1989).

[43] J. F. Dias, "Physical Sensors using SAW devices," *Hewlett-Packard Journal, 32,* pp. 18-20, 1981.

[44] C. Fua, K. Lee, K. Lee, S. Yanga, W. Wangba, "A stable and highly sensitive strain sensor based on a surface acoustic wave oscillator," *Sensors and Actuators A, 218,* pp. 80-87, (2014).

[45] V. Varadan et al., "Wireless passive IDT strain microsensor," *Smart Mater. Struct., 6,* pp. 745-751, (1997).

[46] T. Nomura, T. Kosaka, A. Saitoh, S. Furukawa, "Passive strain sensor using SH-SAW reflective delay line," *Ferroelectrics, 333,* pp. 121-129, (2006).

[47] F. Mubarak et al., "Noise Behavior and Implementation of Interferometer-Based Broadband VNA," *IEEE Transactions on Microwave Theory and Techniques, 67,* pp. 1-12, (2018).

[48] J. F. Nye, Physical Properties of Crystals, Oxford: Oxford Uniersity Press, 1985.

[49] B. Auld, Acoustic Fields and Waves in Solids, New York: J. Wiley and Sons, Ltd, 1973.